Volume 1, Issue 1 | 2025
ISSN: 3102-0798 (Print/Online)

Nanomaterials and Polymers Innovations

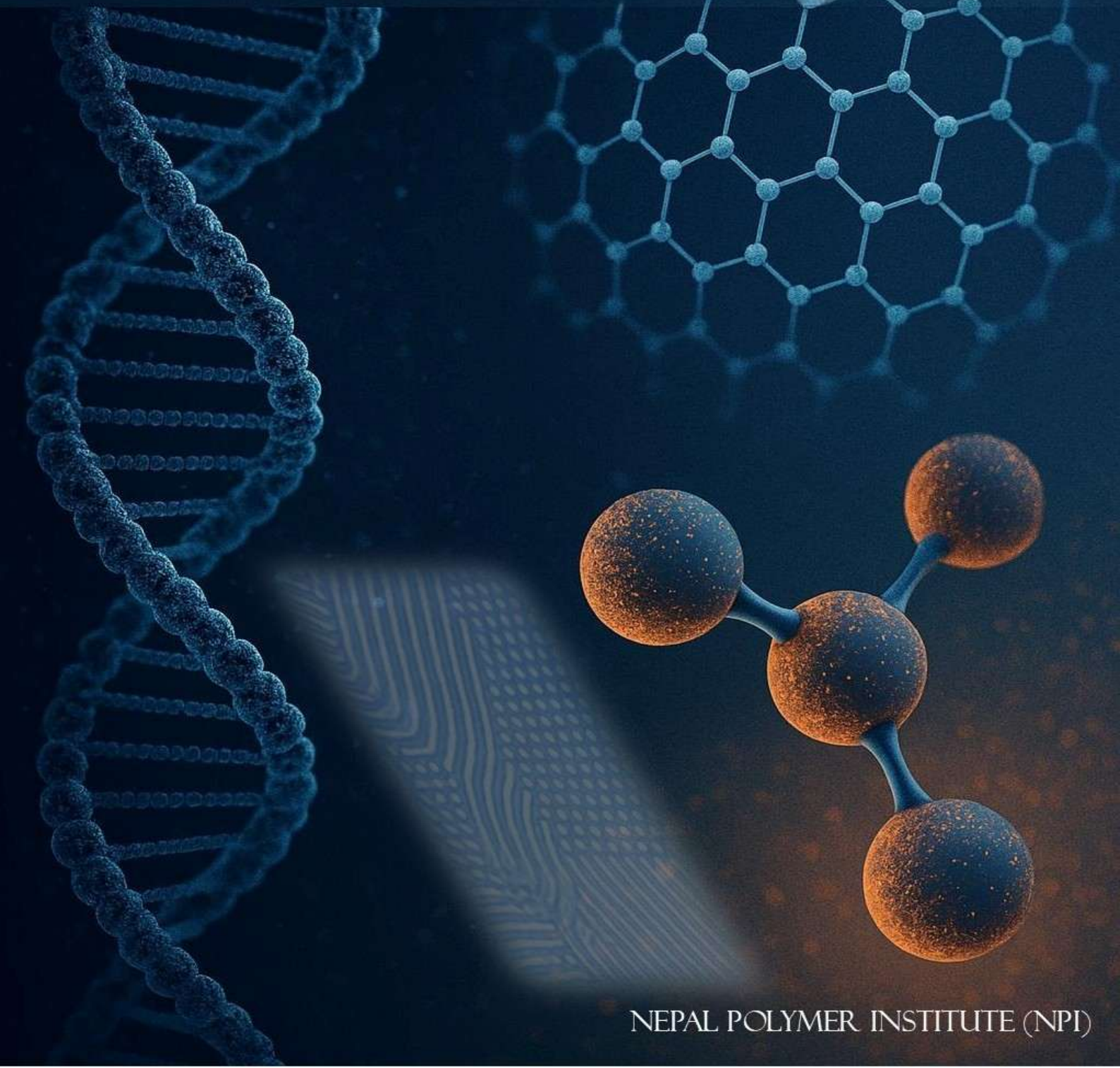

NEPAL POLYMER INSTITUTE (NPI)

Cover page: The cover page, reflecting the underlying themes of design, synthesis, physics, and engineering, particularly in terms of dimensionality, organizational hierarchy, and connections to biological systems, captures the essence of innovations in nanomaterials and polymers. The parallelogram-shaped micrographs positioned on the lower left of the cover, depicting hexagonally arranged cylindrical structures, illustrate the nanostructural hierarchy of a block copolymer system. They are based on a transmission electron micrograph captured by Ms. Sylvia Goerliz in the laboratory of Prof. Goerg Hannes Michler in Halle, Germany. The conceptualization and design of the cover were carried out by Mr. Manish Man Shrestha, with the assistance of AI tools.

Disclaimer: The authors of the articles are solely responsible for all legal and ethical issues related to the content, both in words and notion, of the materials published in this Journal.

Editor In-Chief
Rameshwar Adhikari
Tribhuvan University, Research Centre for Applied Science and Technology (RECAST), Kirtipur, Kathmandu 44618, Nepal

Special Issue Editors
Rameshwar Adhikari, Sven Henning, and Ralf Lach

Editorial Assistance
Nelson Rai and Manish Man Shrestha provided support in the overall manuscript design, typesetting, and printing. Ms. Prasamsha Panta and Ms. Elina Maharjan assisted in establishing the journal's online platform.

© Nepal Polymer Institute (NPI), P. O. Box 24411, Kathmandu, Nepal

INTERNATIONAL EDITORIAL AND ADVISORY BOARD

Dr. Raju Adhikari, RMIT University, Australia

Prof. Volker Abetz, University of Hamburg, Germany

Prof. Dr. Devesh Kumar Avasthi, University of Petroleum and Energy Studies, Dehradun, India

Prof. Berhard Blümich, University of Aachen, Germany

Prof. Ratiram G. Chaudhary, Seth Kesarimal Porwal College, Kamptee, Nagpur, India

Dr. Sven Henning, Fraunhofer Inst. Microstructure of Materials and Systems, Halle, Germany

Prof. Wasudeo Gurnule, Kamla Nehru Mahavidyalaya, Sakkardara, Nagpur, India

Dr. Roger Hiorns, Université de Pau et des Pays de l'Adour (UPPA), France

Prof. Sreekantha Jonnalagadda, University of KwaZulu-Natal, Durban, South Africa

Prof. Vimal Katiyar, Indian Institute of Technology (IIT) Guwahati, Assam, India

Dr. Ralf Lach, Polymer Service GmbH Merseburg (PSM), Merseburg, Germany

Prof. Dr. Beate Langer, University of Applied Sciences, Merseburg, Germany

Prof. Dr. Elizabete F. Lucas, Federal University of Rio de Janeiro (UFRJ), Rio de Janeiro, Brazil

Prof. Ricardo Manríquez González, Universidad Nacional Autónoma de México, México

Prof. Takahiro Maruyama, Meijo University, Nagoya, Japan

Prof. Dr. Sanjay Mathur, University of Cologne, Cologne, Germany

Dr. Yogendra Kumar Mishra, University of Southern Denmark, Sønderborg, Denmark

Prof. Dr. Mehrdad Negahban, University of Nebraska-Lincoln, USA

Dr. Shigeru Okamoto, Nagoya Institute of Technology, Nagoya, Japan

Prof. Tarasankar Pal, Indian Institute of Technology (IIT) Kharagpur, India

Prof. Suprakash Sinha Roy, Council for Scientific and Industrial Research, Pretoria, South Africa

Prof. Dr. Jean-Marc Saiter, Université de Rouen Normandie, Rouen, France

Prof. Sinichi Sakurai, Kyoto Institute of Technology, Kyoto, Japan

Prof. Dr. Holger Schönherr, University of Siegen, Siegen, Germany

Prof. Ajaya Kumar Singh, Government VYT PG Autonomous College, Durg, CG, India

Prof. N. B. Singh, Sharda University, Greater Noida, India

Prof. Dr. Sabu Thomas, Mahatma Gandhi University, Kottayam, Kerala, India

Prof. Dr. Patrick Theato, Karlsruhe Institute of Technology, Karlsruhe, Germany

Dr Santosh K. Tiwari, NMAM Institute of Technology, India

Prof. Wei Wang, Chang'an University, Xi'an, China

CONTENTS

EDITORIAL

NαPI: A Journey to Innovation and Solidarity in New Materials Research

The inaugural issue of *Nanomaterials and Polymers Innovations (NαPI)*, the official *Diamond Open-Access* Journal of Nepal Polymer Institute (NPI), the National Adhering Organization to the International Union of Pure and Applied Chemistry (IUPAC), holds special significance as its publication marks the 80th auspicious birthday of **Professor Dr. Goerg Hannes Michler**, a pioneering scientist whose outstanding contributions have profoundly shaped the fields of polymer science and nanostructured materials.

Professor Michler's scientific legacy spans several decades and encompasses seminal work in polymers, nanostructured polymers, semicrystalline polymers, and structure–property correlations. He is particularly renowned for his groundbreaking contributions in elucidating the relationships between morphological features of homogeneous and heterogeneous solid polymers, gels, and blends and composites, and their micromechanical deformation mechanisms. His work has fundamentally advanced our understanding of how nanoscale and microscale structures govern the macroscopic mechanical performance of polymeric materials.

A hallmark of Professor Michler's research is his unique and innovative use of electron microscopy, especially advanced and *in situ* techniques, to determine micromechanical properties of materials subjected to deformation. His contributions in constructing and designing materials based on micromechanical insights derived from electron microscopy have set benchmarks in the field and continue to influence contemporary materials research worldwide.

Beyond his scientific achievements, Professor Michler's passion for microscopy and education is truly remarkable. He has been actively collaborating with his contemporaries, students, and young researchers to build strong foundations in microscopy, extending even to school students and enthusiastic beginners. Through these efforts, he has inspired generations of scientists and fostered a deep appreciation for materials characterization and microscopy across diverse communities.

This special issue of *Nanomaterials and Polymers Innovations (NαPI)*, the journal's inaugural issue, is guest edited by Professor Michler's former students and is dedicated to honoring his exceptional scientific contributions, mentorship, and enduring influence. We gratefully acknowledge the support of the *POLY-CHAR International Polymer Characterization Forum* for the journal and warmly thank Professor Michler for his inspiring address at the **10th Microsymposium on Applied Sciences (Nano/Bio) - 2025**, held to celebrate his birthday and to mark the public release of this inaugural journal issue. On this occasion, we extend our heartfelt wishes to Professor Goerg H. Michler for good health and a continued active and inspiring life ahead.

May 19, 2025

Nanomaterials and Polymers Innovations Vol. 1, No. 1 (2025); 02-04
ISSN: 3102-0798 (Online). Available online at www.nepalpolymer.org
DOI:https://doi.org/.....xyz.....xyz (to be updated)

Letter to the editor

MBENEs: A New Class of 2D Materials Beyond MXenes

Santosh K. Tiwari*
Centre for New Materials and Surface Engineering, NMAM Institute of Technology, Nitte, 574110, India
ORCID: 0000-0003-1602-9345

Abstract: Developing advanced materials is key to progress in energy, electronics, and environmental technologies. MBENEs, a new class of 2D transition metal borides (Mn+1Bn), offer exceptional electrical conductivity, thermal stability, and chemical resilience. Derived from MAB phases via selective etching, MBENEs differ from MXenes in their strong M–B bonds, making synthesis more challenging but promising for harsh-environment applications. Unlike graphene and MXenes, MBENEs combine metal-like conductivity with catalytic activity and structural robustness. Though current research on MBENEs is largely theoretical, early studies highlight their potential in catalysis, energy storage, and high-temperature electronics. Indeed, key challenges remain in scalable synthesis and surface property control to realize their technological promises.

शोधसार: उन्नत सामग्रीहरूको विकास ऊर्जा, इलेक्ट्रोनिक्स, र वातावरणीय प्रविधिमा प्रगतिको प्रमुख कुञ्जी हो। MBENEs (Mn+1Bn) नामक नयाँ वर्गका दुई-आयामी ट्रान्जिशन मेटल बोराइडहरूले असाधारण विद्यतिय सुचालकता, तापीय स्थायित्व, र रासायनिक प्रतिरोध प्रदान गर्छन्। MAB फेजहरूबाट छानिएको एचिङ प्रविधिमार्फत प्राप्त गरिने यी MBENEs, MXenes भन्दा फरक छन् किनभने तिनीहरूमा M–B बन्धनहरू बलिया हुन्छन्, जसले गर्दा तिनिहरुलाई संश्लेषण कठिन हुन्छ तर कठोर वातावरणमा प्रयोगका लागि सम्भावनायुक्त बनाउँछ। ग्राफिन र MXenes भन्दा फरक रूपमा, MBENEs ले धातु-जस्तै सुचालकता, उत्प्रेरक सक्रियता, र संरचनात्मक दृढता संयोजन गर्छन्। यद्यपि हालसम्मको अनुसन्धान प्रायः सैद्धान्तिक छन्, प्रारम्भिक अध्ययनहरूले उत्प्रेरक, ऊर्जा सञ्चयन, र उच्च तापमा काम गर्ने इलेक्ट्रोनिक उपकरणहरूमा तिनीहरूको सम्भावना देखाएका छन्। यस्ता प्रविधिगत सम्भावनाहरू साकार पार्न अझै पनि ठूला चुनौतीहरू, जस्तै ठूलो मात्रामा संश्लेषण र सतह गुणहरूको नियन्त्रण, कायम छन्।

INTRODUCTION

The development of new materials is essential for cutting-edge technology, enabling breakthroughs in energy, aerospace, electronics, tissue engineering, and environmental sustainability [1,2]. Novel materials with tailored properties boost innovation in devices and systems by overcoming the limitations of existing materials [1,2]. In this context, MBENEs (Cr_2B_2, Fe_2B_2, Mo_2B_2, W_2B_2, etc. based on first-principles calculations) a new 2D transition metal borides class, offer exceptional electrical conductivity, thermal stability, and chemical resilience [3,4]. These properties position MBENEs as promising candidates for next-generation applications in catalysis, energy storage, and harsh environment electronics, addressing critical challenges where other 2D materials like graphene or MXenes may fall short [3,5,6]. The emergence of MBENEs exemplifies the transformative potential of engineered 2D materials. In this regard, over the past three decades, research has surged into discovering and synthesizing numerous 2D systems with tailored properties for applications spanning sensing, robotics, electronics, energy storage, catalysis, and many more. Among these, graphene, transition metal dichalcogenides MXenes, and h-BN nanosheets got great consideration, and now the emerging class of MBENEs (a 2D transition metal borides, having general formula $M_{n+1}B_n$ where M = early transition metal, and B = boron) represent critical milestones. Thus, MBENEs are composed of metal boride nanosheets and are directly exfoliated from MAB phases (**Figure 1**). MAB phases are structurally analogous to the more

Corresponding author, E-mail: ismgraphene@gmail.com
© Nepal Polymer Institute, Kathmandu, Nepal
Received: April 23, 2025; Revised: May 11, 2025, Accepted: May 11 2025; Published: May 19, 2025

established MAX phases from which MXenes are derived. In a typical MAB phase, a transition metal (M) is bonded to a boron sublayer (B), and the structure is interleaved with an (A) group element, commonly from groups 13 to 16. Through selective etching usually targeting the A-site element researchers aim to exfoliate the M–B layers, thereby yielding MBENE sheets. However, unlike MAX-derived MXenes, where the M–C or M–N bonds are relatively ionic and easier to disrupt, the M–B bonds in MAB phases exhibit stronger covalency and greater structural rigidity. This difference makes the synthesis of MBENEs greatly challenging, requiring innovative etching strategies and thermodynamically guided processes, including molten salt and electrochemical methods [4,6–8].

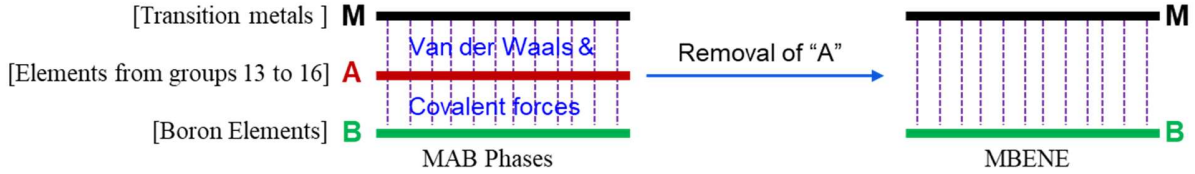

Figure 1. Schematic diagram showing the composition of MAB phases, MBENE, and the general strategy for conversion of MAB phases to MBENE

Each class of 2D materials offers distinct chemistry, structure, and functionality and possesses its advantages and shortcomings. In this line, MBENEs, introduce a different paradigm; combining the advantageous features of transition metals and boron in ultrathin, crystalline architectures. These materials, though still in their infancy, hold the promise of addressing some of the limitations faced by graphene, MXenes and h-BN nanosheets. Nevertheless, the attraction of MBENEs lies in their combination of robust thermal stability, high electrical conductivity, and chemical durability behaviors that make them mainly outstanding for harsh environments and high-performance applications. Compared to MXenes, which are often terminated with–F, –OH, or –O groups that enhance hydrophilicity and reactivity but also introduce structural instability in certain conditions, MBENEs provide a more chemically resilient alternative. The presence of boron, known for forming strong covalent bonds and contributing to high hardness and oxidation resistance, imparts greater thermal and chemical endurance to MBENEs. Therefore, MBENEs become promising candidates for next-generation electrocatalysts, high-temperature electronics, and protective coatings. In comparing MBENEs to MXenes, several important distinctions appear. MXenes first synthesized in 2011 have undergone extensive development, with over 30 distinct compositions reported and widespread application in supercapacitors, battery electrodes, electromagnetic shielding, and sensors [7,9]. The surface chemistry of MXenes, enabled by abundant terminal groups, is both a strength and a weakness. Although MXenes allow for functionalization and dispersion in aqueous media, these also contribute to oxidation degradation and electrochemical side reactions. In contrast, MBENEs are expected to be less reactive, thereby offering better longevity in operational devices. However, the trade-off is limited surface tunability, at least based on present research. In the same line, compared to graphene, MBENEs present an even more differentiated profile. Graphene, with its pristine sp^2-bonded carbon lattice, remains unmatched in terms of carrier mobility, mechanical flexibility, and chemical purity. Yet graphene's chemical inertness, although beneficial in some contexts, limits its ability to host active sites for catalysis or ion intercalation without defect engineering or heteroatom doping [5,10]. MBENEs, due to their transition metal centers and boron-based structure, naturally offer metal-like conductivity and catalytically active sites, especially when surface terminations or structural defects are introduced [2–4]. This makes them promising alternatives in energy storage and conversion technologies where graphene falls short. Nevertheless, the current state of MBENE research is largely exploratory. Moreover, the experimental reports are sparse, with only a handful of successful syntheses (e.g., Ti_2B and Mo_2B) documented whereas 100 s of methods have been developed for graphene production. In the case, of MBENEs most

studies remain computational and theoretical, using density functional theory to predict properties such as electronic structure, magnetic ordering, and thermodynamic stability [11]. These theoretical insights suggest that MBENEs can exhibit a rich diversity of behaviors, from metallic to semiconducting phases, and from nonmagnetic to ferromagnetic configurations, depending on the choice of transition metal and boron framework. The potential for tunable band structures via strain/doping further improves the importance of MBENEs. Importantly, to transition MBENEs from concept to technology, several challenges must be addressed. First, scalable and controllable synthesis methods are required to produce phase-pure, few-layer MBENE sheets with the defined morphology. Second, a deeper understanding of their structural, surface, and morphological properties, especially regarding possible terminations and their impact on properties, is very indispensable. Third and most crucial, application-specific optimization such as improving ion diffusion kinetics for battery electrodes, or maximizing surface area and active sites for catalysis must be undertaken.

In summary, MBENEs represent a compelling addition to the 2D material family, combining aspects of MXenes and graphene but carving out a unique identity defined by boron-rich chemistry and transition-metal functionality. Although, the theoretical promise of MBENEs is high, and their experimental progress, currently it is in a nascent stage, and gaining momentum widely in the materials science fraternity. Based on scientific progress, it is assumed that as synthetic techniques improve and mechanistic understanding deepens, MBENEs could become central to future materials platforms in energy, electronics, and beyond. Their arrival signals a continued diversification of the 2D materials landscape, offering new possibilities for designing functional matter at the atomic scale.

Acknowledgment: SKT sincerely appreciates the support of the SPARC project (P3808) under the Indo-UK scheme. Additionally, SKT extends heartfelt gratitude to Nitte University for providing the research grant (Grant No. NUFR-23–070), which has significantly facilitated our research endeavors.

REFERENCES

1. Glavin NR, Rao R, Varshney V, Bianco E, Apte A, Roy A, et al. Emerging Applications of Elemental 2D Materials. Advanced Materials. 2020;32(7):1904302.
2. Cai X, Luo Y, Liu B, Cheng HM. Preparation of 2D material dispersions and their applications. Chem Soc Rev. 2018 Aug 1;47(16):6224–66.
3. Jakubczak M, Szuplewska A, Rozmysłowska-Wojciechowska A, Rosenkranz A, Jastrzębska AM. Novel 2D MBenes—Synthesis, Structure, and Biotechnological Potential. Advanced Functional Materials. 2021;31(38):2103048.
4. Zhang B, Zhou J, Sun Z. MBenes: progress, challenges and future. J Mater Chem A. 2022 Aug 4;10(30):15865–80.
5. Tiwari SK, Sahoo S, Wang N, Huczko A. Graphene research and their outputs: Status and prospect. Journal of Science: Advanced Materials and Devices. 2020 Mar 1;5(1):10–29.
6. Hayat A, Bashir T, Ahmed AM, Ajmal Z, Alghamdi MM, El-Zahhar AA, et al. Novel 2D MBenes-synthesis, structure, properties with excellent performance in energy conversion and storage: A review. Materials Science and Engineering: R: Reports. 2024 Jun 1;159:100796.
7. Lim KRG, Shekhirev M, Wyatt BC, Anasori B, Gogotsi Y, Seh ZW. Fundamentals of MXene synthesis. Nat Synth. 2022 Aug;1(8):601–14.
8. Nair VG, Birowska M, Bury D, Jakubczak M, Rosenkranz A, Jastrzębska AM. 2D MBenes: A Novel Member in the Flatland. Adv Mater. 2022 Jun;34(23):e2108840.
9. Naguib M, Barsoum MW, Gogotsi Y. Ten Years of Progress in the Synthesis and Development of MXenes. Advanced Materials. 2021;33(39):2103393.
10. Tiwari SK, Kumar ,Vijay, Huczko, Andrzej, Oraon, R., Adhikari, A. De, and Nayak GC. Magical Allotropes of Carbon: Prospects and Applications. Critical Reviews in Solid State and Materials Sciences. 2016 Jul 3;41(4):257–317.
11. Ozdemir I, Kadioglu Y, Üzengi Aktürk O, Yuksel Y, Akıncı Ü, Aktürk E. A new single-layer structure of MBene family: Ti2B. J Phys: Condens Matter. 2019 Sep;31(50):505401.

Nanomaterials and Polymers Innovations Vol. 1, No.1 (2025); 05-18
ISSN: 3102-0798 (Online). Available online at www.nepalpolymer.org
DOI:https://doi.org/.....xyz... xyz (to be updated)

Original research paper

Nuclear Magnetic Resonance of Deformed Polymers

Bernhard Blümich*
**Institut für Technische und Makromolekulare Chemie, RWTH Aachen University, Germany*

Abstract: Most polymer products are designed to bear mechanical loads. These affect the conformation and mobility of their constituent macromolecules. Nuclear magnetic resonance (NMR) is sensitive to molecular conformation and mobility and has been employed to study the signature of macroscopic deformation of polymer materials on a scale ranging from molecular to macroscopic dimensions. This report reviews key studies of polymer deformations by NMR spectroscopy, relaxometry, and imaging.

Keywords: NMR, relaxometry, imaging

शोधसार: धेरैजसो पोलिमर उत्पादनहरू यांत्रिक भार सहन सक्ने गरी डिजाइन गरिएका हुन्छन्। यस्ता भारहरूले तिनीहरूको संरचनात्मक म्याक्रोमोलेक्युलहरूको आकृति र गतिशीलतामा असर पार्दछ। न्युक्लियर म्याग्नेटिक रेजोनेन्स (NMR) प्रविधि आणविक आकृति र गतिशीलताको लागि संवेदनशील हुन्छ, र यसलाई पोलिमर सामग्रीको आणविकदेखि म्याक्रोस्कोपिक स्तरसम्मको बस्तुको संरचनामा हुने रुपान्तरणको अध्ययन गर्न प्रयोग गरिएको छ। यो प्रतिवेदनले NMR स्पेक्ट्रोस्कोपी, रिल्याक्सोमेट्री, र इमेजिङ प्रयोग गरी पोलिमरको संरचनामा हुने रुपान्तरण तथा संरचनात्मक विकृति सम्बन्धी गरिएका प्रमुख अनुसन्धानहरूलाई समेट्छ।

INTRODUCTION

Polymer materials are formulated from macromolecules, processing and antiaging additives, plasticizers, and fillers [1-4]. Their main constituent are the macromolecules. These are large molecules, most often chains of small molecular repeat units, typically with branches, and some with cross-links to other chains. Elastomers are the most important representative of cross-linked macromolecules in the molten or rubbery state. Technical macromolecules are not uniform like small molecules but exhibit distributions in molecular weight and configuration in terms of branches and sequences of repeat units if there is more than one repeat unit or if the same repeat units are connected in different ways.

Polymer materials are often classified according to the conformation of the macromolecules in the solid state. In the melt, the macromolecular chains form random, interpenetrating coils with free volume between chains, which enables translational motions of entire chains and local motions of chain segments. The melt freezes upon cooling below the glass transition temperature. In the frozen melt, the translational motion of entire chains is largely disabled while local motions persist. Such amorphous polymers typically are transparent and are called glassy polymers. Strictly speaking, they are not in thermodynamic equilibrium, and given enough time, chain segments can still slip past each other, particularly under pressure or strain, unless the chains are crosslinked. The nature of cross-links can be either chemical, i. e., the cross-links are formed by chemical bonds, or physical, i.e., the macromolecules are physically entangled through loops and knots or linked through crystalline domains formed by two or more polymer chains.

Partially crystalline polymers are called semicrystalline, and their crystalline domains may form ordered structures, for example, lamellae. The term crystalline polymer is used synonymously with semicrystalline polymer, as single crystals of large macromolecules are difficult to grow. The mobility of the polymer chain segments in the amorphous regions is higher, along with more free volume, while it is lower in the crystalline regions and mostly located at crystal defects. At the interface from ordered

Corresponding author, E-mail: bluemich@itmc.rwth-aachen.de
© Nepal Polymer Institute, Kathmandu, Nepal
Received: May 3,, 2025; Revised: May 17, 2025, Accepted: May 17, 2025; Published: May 19, 2025

crystalline domains to disordered amorphous domains, the segmental chain mobility transitions from low to high. Molecular order also arises in polymer melts under shear and in liquid-crystalline polymers. It is directly probed by diffraction patterns from x-ray scattering and by wide-line solid-state NMR (nuclear magnetic resonance) spectroscopy. It is indirectly probed via molecular mobility, for example, by NMR relaxometry.

NMR probes the magnetic moments of nuclear spins in molecules exposed to magnetic polarization fields. It has three major modalities, spectroscopy, imaging, and relaxometry [5]. NMR spectroscopy of molecules in solution is one of the most important methods of chemical analysis for identification of molecular structures [6]. With molecules in the solid state, NMR spectroscopy for chemical analysis is hampered by various anisotropic interactions between the nuclear spins. But the rapid thermal molecular motion prevalent in solution can be artificially replaced in solids by rapid rotation of the entire solid sample at a particular angle relative to the direction of the applied magnetic field. This technique is known as magic angle spinning (MAS) NMR and leads to solid-state spectra with lines nearly as narrow as in liquid-state NMR spectra. On the other hand, the anisotropic spin interactions can be exploited to probe molecular order and mobility [7]. To this end, many studies of solid polymers have been conducted by recording wide-line deuteron (^{2}H) NMR spectra from selectively deuterated chemical positions of interest. These spectra are much broader than the lines in MAS spectra, because each molecular orientation in the magnetic field gives rise to a different NMR frequency.

Solid-state NMR spectra are recorded with expensive NMR instruments fitted with high-field

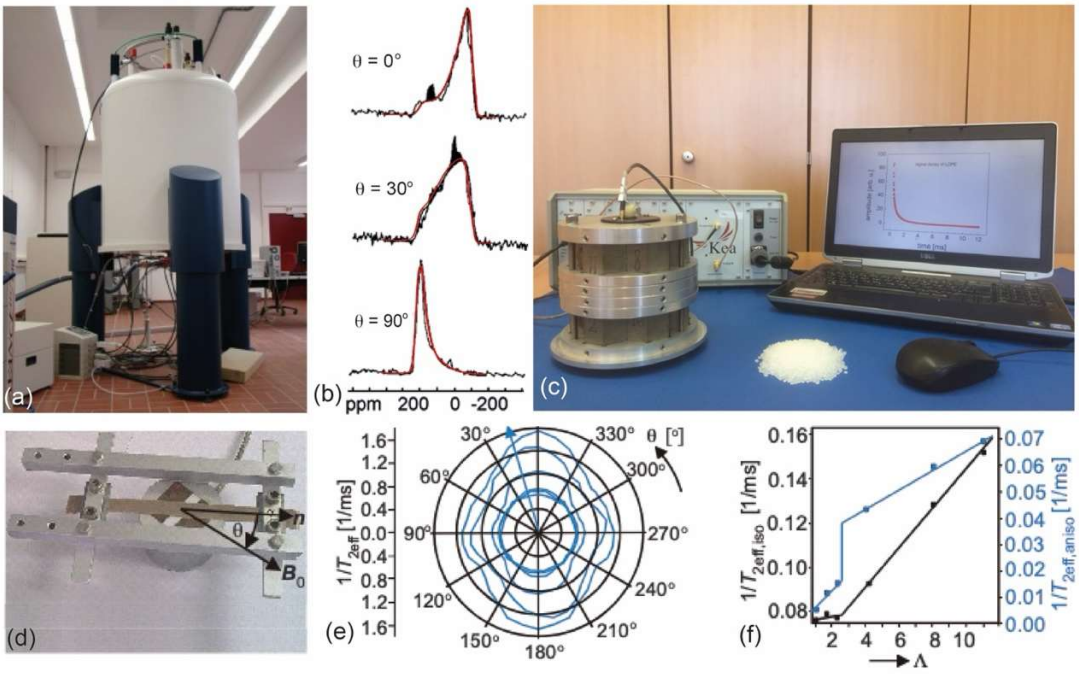

Figure 1. (a) Magnet of an 800 MHz spectrometer for chemical analysis by NMR spectroscopy [5]. (b) Orientation-dependent ^{13}C wide line NMR spectra of a ^{13}C-labeled liquid-crystalline sidechain polymer with different orientation angles θ between the alignment direction and the magnetic field [8]. (c) Low-field NMR set-up for measurement of NMR relaxation signals [5]. The sample is positioned inside the permanent magnet (left). A transverse NMR relaxation curve (red) is shown on the computer screen. (d) Strained rubber band positioned on a stray-field magnet (NMR-MOUSE [9]) for angle-dependent relaxation measurements [5]. (e) Strain and angle-dependent relaxation rates measured for unfilled natural rubber [10]. With increasing strain, the relaxation anisotropy increases. (f) Isotropic and anisotropic relaxation rates extracted from (e) as a function of elongation Λ [5].

superconducting magnets (Fig. 1a) [5]. Liquid-state NMR spectra, on the other hand, can nowadays also be measured routinely with small bench

top instruments, which are considerably less expensive and simpler to operate [11]. Compact as well as portable or mobile
NMR instruments also exist for measuring NMR relaxation signals (Fig. 1c) [12,13]. NMR relaxation does not provide
molecular information about the chemical nature of a substance, but instead it provides mesoscopic information about the physical properties of a material. It refers to the NMR relaxation times T_1 and T_2 characterizing build-up and decay of nuclear magnetization [14], which relate to the mobility of molecules and, in turn, to the viscoelastic properties of matter [15]. NMR relaxometers are less demanding on magnet performance than NMR spectrometers; they are more robust and can be operated in harsher environments. While most benchtop NMR instruments require a sample to be fitted inside a center hole of a permanent magnet (Fig. 1c), portable instruments acquire essentially the same information locally from a selected region inside intact objects by facing them from one side (Fig. 1d) [16]. When shifting the sensor relative to the object, images can be acquired pixel by pixel.

NMR imaging (MRI – magnetic resonance imaging) is a modality of NMR where spatial resolution is introduced by means of magnetic gradient fields [17-19]. NMR images report molecular properties visually on a macroscopic scale. The main use of MRI is in clinical diagnostics, but it is also employed to a considerable extent in materials science, chemical engineering, and related fields [13,20-23], including rheological studies of complex fluids [24].

All three NMR modalities, spectroscopy, relaxometry, and imaging have been explored to investigate the effects of mechanical force on polymer materials. In the following, major contributions of the NMR literature in this field are reviewed for different types of macromolecular materials.

RUBBERY MATERIALS

Basic NMR

Rubber is a melt of entangled macromolecules. Crosslinking inhibits translational motion of the macromolecules, so that they can no longer diffuse and slip past each other. Active fillers like carbon black strongly interact with the macromolecules and affect their segmental motion near the filler-particle surface and significantly alter the mechanical properties of the material. Between crosslinks the motion of the macromolecular chains is fast reminiscent of the motion in a low-molecular melt, but anisotropic so that orientation-dependent spin interactions like the dipole-dipole coupling among protons and the quadrupolar coupling of deuteron spin labels are no longer averaged out. Rubbery materials have been studied extensively by NMR to understand their structural and dynamic properties and the effects of strain, exploring the orientation-dependent residual dipolar and quadrupolar couplings.

In the relaxed state without deformation, the ^{1}H NMR resonance of elastomers is broadened compared to that of liquids due to the molecular motion being constrained by crosslinks and entanglements between polymer chains. As a result, the information attached to the chemical shift is blurred and mostly lost so that most investigations concern the ^{1}H NMR signal decay in the time domain or the transverse magnetization decay, while spectral analyses rely on other nuclei such as ^{13}C with a far wider chemical shift range and on ^{2}H after site-specific isotope enrichment.

^{1}H relaxometry

Models of the ^{1}H NMR signal decay of cross-linked rubber account for different motional regimes in the rubber network [25-27]. Depending on the model, different simplifying assumptions are made in calculating the ^{1}H signal decay [28]. The frozen-bond model assumes that all crosslink positions in a network are immobile and that the end-to-end vectors of the inter-crosslink chains have a Gaussian distribution [29–31]. The second-moment model assumes a Gaussian distribution of dipolar interactions and an exponential correlation function of the segmental motion [32]. Both models can explain the non-exponential nature of the NMR impulse response, specifically the free induction magnetization decay (FID) of the amplitude in the Hahn-echo NMR experiment [28]. Yet for practical purposes a simple approximation of the signal decay in terms of a sum of three relaxation decays often suffices, in which the individual terms account for the more fixed inter-crosslink chains, for dangling chains and for the sol part.

Fitting theoretical relaxation decays to experimental data gives access to the cross-link density [33,34]. Its variation across an elastomer product can be assessed by NMR imaging [35,36] or depth-resolved stray-field NMR relaxometry [9,37,38]. Approaches to cross-link density and other material parameters more sophisticated than simple relaxation analyses explore multi-quantum phenomena resulting from the residual dipole-

dipole interactions among the protons in randomly oriented inter-crosslink chains [39-42].

Upon straining, the motional anisotropy of the intercross-link chains is enhanced, and the signal decay changes from more liquid-like to more solid-like [25-27]. This means that the chemical shift anisotropy, the dipole-dipole interaction among nuclear spins, and the quadrupole couplings of ^{2}H isotope labels are enhanced because the molecular motion is averaged to a lesser degree. In the deformed regions, the macromolecular chains align so that the overall NMR signal depends on the orientation of the alignment direction with respect to the applied magnetic field [31,43]. Not only can an orientation-dependent splitting of the resonance line be observed, but also the NMR relaxation times become anisotropic. While the dependence of the NMR signal on strain and time in terms of relaxation times and component amplitudes can be followed with moderate effort employing a conventional NMR setup, where the sample is positioned in the center inside an NMR magnet [44], to study the orientation dependence of the NMR signal requires the angle between the strain direction and the magnetic field to be varied. This can be achieved either with the sample and the stretching device inside the confinement of the NMR magnet or with a simple stray-field setup using a sensor like the NMR-MOUSE (MObile Universal Surface Explorer), where the strained sample rests on the magnet, and the NMR signal is acquired from a region inside the sample but outside the magnet (Fig. 1d) [9,10]. When approximating the signal decay of the strained elastomer by a single exponential function, the orientation dependence of the transverse relaxation rate in natural rubber (Fig. 1e) can be modelled by the sum of an orientation-independent relaxation rate and a relaxation rate which depends on the square of the second Legendre polynomial. With increasing strain, both relaxation rates increase albeit at different rates (Fig. 1f). At an elongation of about $\Lambda = 2.3$, strain-induced crystallization sets in. At this elongation the anisotropic relaxation rate exhibits a first order phase transition as a function of Λ while the isotropic relaxation rate changes in a way reminiscent of the glass transition or a second order phase transition [45]. Strain-induced crystallization has been investigated by NMR relaxometry and multi-quantum NMR for natural rubber and polyurethane elastomers [46,47].

Along with chain alignment, mechanical deformation alters segmental mobility, affecting proton transverse relaxation [48-50] and relaxation dispersion [50] as well as multipolar spin states [51] and multi-quantum build-up curves [39-42]. Fillers enhance mechanical reinforcement but introduce heterogeneous strain fields. They affect local strain distributions and overstrain phenomena [52,53]. Reinforced elastomers exhibit non-affine deformation, where local strain does not follow macroscopic deformation. In solid propellants, ^{1}H NMR relaxometry identifies deformation-induced microstructural changes [54]. In thermoplastic elastomers, deformation influences the microphase-separated structure of the copolymers, affecting chain dynamics and relaxation times [48].

^{13}C NMR spectroscopy

Effects of strain are also observable in NMR spectra of ^{13}C in natural abundance and of ^{2}H isotope labels enriched at selected chemical sites. ^{13}C NMR spectra of strained rubber exhibit broadened lines which depend on the sample orientation in the magnetic field [55,56]. While the ^{1}H-^{13}C dipole-dipole interaction is suppressed during measurement, the ^{13}C-^{13}C dipole-dipole coupling is negligible due to the low natural abundance of the nuclei, but the large ^{13}C chemical shift range enables the chemical shift anisotropy to be resolved, leading to small variations in resonance frequencies for different chain-segment orientations. In natural rubber, the efficiency of transferring ^{1}H magnetization to ^{13}C by cross-polarization was affected by strain-induced chain orientation, revealing a time-dependent mechanism of chain-segment dynamics on dynamic strain [57], and strain-induced crystallization was studied by high-resolution solid-state ^{13}C NMR spectroscopy of natural rubber samples stretched *in situ* [58].

^{2}H NMR spectroscopy

The most detailed insights by NMR into the molecular dynamics and structural characteristics of strained or deformed elastomers are obtained by analyzing the resonance of chemical sites specifically enriched with deuteron isotope labels. ^{2}H is a quadrupolar spin 1 nucleus which exhibits orientation-dependent line shapes on the order of 2 kHz wide in elastomers and up to 250 kHz wide in rigid polymers, dominating the dipole-dipole coupling and the chemical shift anisotropy [59,60]. From fits of modelled to measured line shapes, the orientational distribution function, geometry, and timescale of molecular motion can

be extracted. Two-dimensional NMR experiments are particularly powerful in this regard [60].

Early on, this chemically demanding approach was employed to study the effects of deformation on chains in rubber-elastic networks. Strain, but also compression, leads to strain-dependent splitting of the ^{2}H NMR resonance due to average uniaxial chain orientation under strain [61-64]. Experiments on homogeneously deuterated networks and on partially deuterated networks with short deuterated segments at network junctions revealed a nonaffine deformation mechanism where short elastically effective chains are stretched to a greater extent than long chains along with an excess orientation near network junctions [2,65]. By analyzing the ^{2}H NMR line shape, the contributions from the network constraints and the chain interactions to the average orientation of the chain segments can be separated, and the average molecular weight between topological constraints be calculated [66,67]. Moreover, ^{2}H NMR spectroscopy reveals that the molecular dynamics along the cross-link chain are heterogeneous and more restricted in the junction zones [68,69]. Consequently, effects of chain orientation from strain are stronger in the center of cross-link chains than near the cross-link points [70]. Similar heterogeneity of molecular dynamics is produced by active fillers, where local chain mobility is slowed down in an adsorption layer [72]. A relatively small fraction of chains strongly absorbed to active fillers impacts the stress-strain properties of filled elastomers significantly [72].

The chemical labelling effort is avoided, if deuterated network-like chains are incorporated into the elastomer sample by swelling prior to measurement [73-75]. In this way, stress-induced crystallization and melting have been studied in natural rubber with and without carbon black filler [76,77]. The segmental order observed upon dilution, however, depends on the solvent. The chain order is less affected by chain oligomers as solvents than with conventional low molecular weight solvents [78]. Yet the anisotropy of the cross-linked network suffices even in stretched poly(dimethyl siloxane) gels to slightly align biomolecules so that their residual dipolar couplings can assist the effort to unravel their molecular structures [79-81].

Magnetic resonance imaging

NMR imaging (MRI – Magnetic Resonance Imaging) is a nondestructive method particularly suited to obtain 3D and 2D tomographic images of soft matter [17,18]. It has become an indispensable diagnostic tool in medicine, complementing X-ray tomography by its abundance of contrast parameters for soft matter diagnosis. The synthetic equivalence to biological soft matter is rubber and elastomers, so that early on, MRI has been explored to study rubbery materials, with particular attention to variations in crosslink density, filler distribution, solvent ingress, and aging [20,35,36]. While on a sufficiently coarse scale rubbery materials are considered homogeneous, the NMR signal from sufficiently small volume elements reveals variations in cross-link density and filler content, an observation to be expected when considering the statistical nature of their distributions. Already, the voxel volume of MRI and even stray-field NMR is small enough to be sensitive to such inhomogeneities [82]. Additional inhomogeneities arise from insufficient mixing during product manufacturing [83], so that MRI, along with stay-field NMR relaxometry, are valuable assets in rubber process control and manufacturing [84]. Large products do not fit into the MRI magnet, and those containing steel, like most tires, are unfit because of their interaction with the magnet. While the use of rubber MRI is mainly of interest in research, stray-field NMR relaxometry is well integrated in parts of the tire industry [9,37,38].

An early MRI study revealed that the spatial distributions of the ^{1}H spin density is lowered and the molecular motion of water molecules in a gel is slowed down by compression compared with those in the surrounding uncompressed region [85]. A filled polysiloxane rubber band with a cut was imaged under elongation [83]. The filler distribution was found to be inhomogeneous, and images of the transverse relaxation time were calibrated to report stress and strain maps. Local strain has also been mapped by means of deuterated spy oligomers incorporated into the object and making use of their strain-dependent double-quantum signal or the ^{2}H line splitting, as has been demonstrated with deuterated poly(butadiene) oligomers incorporated into a natural rubber band with cuts [86,87]. The same information can be obtained without sample preparation by mapping different multi-quantum NMR parameters associated with the strain-dependent residual ^{1}H-^{1}H dipolar coupling [88,89]. In a comparative study, MRI and stray-field relaxometry with the NMR-MOUSE were found to reveal differences in molecular mobility in silicone elastomers arising from differences in cross-link density, material heterogeneity, aging, and strain [90]. Moreover, the impact of radiation

on the shear modulus of silica-filled PDMS elastomers was quantified by ^{1}H relaxation measurements and stray-field imaging [91].

Depending on the loss modulus, the mechanical energy imparted to the rubber material by dynamic mechanical load raises the temperature. The thermal energy is dissipated through the surface of the object, leading to a temperature distribution inside. The distributions of molecular mobility associated with different carbon-black filler contents of dynamically sheared rubber cylinders were reported by parameter images of the transverse relaxation time and recalibrated to temperature distributions [92].

In a unilateral stray-field NMR setup, oscillation-synchronized NMR excitation served to extract the deformation waveforms in different viscoelastic polyurethane samples, which were then processed to calculate the loss-angle and magnitude of the dynamic modulus for each sample [93]. Mechanical motion, like oscillatory or viscous fluid shear, can well be studied by MRI and unilateral stray-field NMR. The underlying NMR methodology and instrumentation have recently been reviewed in the literature with particular attention to portable stray-field NMR, which provides open access to the sample for mechanical deformation accessories [94].

By means of magnetic field gradients oscillating with the same frequency as the mechanical deformation, the propagation of mechanical waves can be imaged, and their interference patterns can be analyzed, giving access to maps of the storage and loss moduli across an object [18]. This approach is termed NMR elastography. It can be employed for elastomers [95–98] but more importantly, it is of considerable interest for diagnosing cancer in living tissue [99–103].

RIGID POLYMERS

^{1}H relaxometry

Rigid polymers are predominantly in the amorphous, glassy state below the glass transition temperature or the semicrystalline state between the glass transition temperature and the melting temperature. The amorphous regions usually are characterized by higher segmental mobility and larger free volume than the defect-bearing crystalline regions. They are commonly understood to respond to increasing mechanical deformation before the crystalline domains are affected, leading to strain hardening, brittle or ductile behavior depending on the deformation rate and temperature, and crazing until failure [104,105]. ^{1}H NMR relaxation studies are also well suited to investigate the impact of deformation and aging in solid polymers, because these phenomena primarily affect the segmental mobility on a time scale to which NMR relaxation is sensitive.

Mobile, single-sided NMR relaxometry is a unique tool for investigating the effects of polymer aging, deformation and annealing, which has been demonstrated on a variety of technologically relevant materials like LDPE (low density poly(ethylene)) steel-pipe shells, HDPE (high density poly(ethylene)) pipes, polypropylene, and Nylon 6 [106–111]. The NMR signal decay of a semicrystalline polymer can be decomposed into three different components, which are attributed in decreasing order of the relaxation times to the amorphous, interfacial, and crystalline domains constituting the material morphology. In uniaxially stretched poly(propylene), both the relaxation times of the amorphous and the interfacial regions decreased with increasing elongation while the amorphous content increased, and the interfacial and crystalline contents decreased [109]. Similarly, a recent, combined study of the amorphous-chain reorientation under uniaxial elongation of low-density polyethylene relying on wide-angle X-ray scattering data and orientation-dependent solid-state NMR signal decays revealed the formation of additional rigid amorphous regions above a threshold elongation [112]. On the other hand, in a weakly curved, carbon-black-filled PE pipe section, both the relaxation times of the amorphous and the interfacial regions increased upon straining the pipe [106,108|.

NMR spectroscopy of ^{2}H and ^{13}C isotope labels

Enhanced chain mobility was also observed by deuteron NMR in the amorphous regions of deuterated Nylon 6 under active uniaxial deformation near the glass transition temperature, which relaxed upon stress release [110], whereas the mobility of D_2O incorporated into Nylon-6 became progressively confined with increasing alignment of polymer chains and strain-associated changes in polymer morphology [111].

Strain-enhanced molecular mobility is also expected from molecular dynamics simulations for glassy polymers [113,114]. This has been observed by ^{2}H NMR for bulk polycarbonate and poly(*p*-phenyleneterephthalamide) fibers [115–118]. Wideline ^{2}H 2D exchange NMR spectroscopy of phenyl-ring deuterated polycarbonate revealed that the reorientation angle distribution of the phenyl-ring flip widened

upon stretching the sample inside the NMR magnet with a dedicated titanium rig [117]. Subsequently, enhanced phenyl ring dynamics were observed by the same method in poly(*p*-phenyleneterephthalamide) fiber bundles uniaxially loaded to 55% of their breaking strength [116]. Moreover, double quantum correlated 2D NMR spectroscopy on doubly ^{13}C labeled polycarbonate confirmed that the geometry of the entanglement network is the most important structural parameter for the plastic behavior of glassy polymers [117]. The conformational distribution was found to be unaffected by the deformation, whereas small changes in the local packing of molecular segments could be detected in terms of the phenylene ring planes tending to orient parallel to one another upon deformation [118]. The same experimental technique revealed that the degree of molecular alignment in dragline silk fibers increases with the fiber draw rate, and that it changes more, when the drawing tension on the fiber is relaxed from higher draw rates [119]. Wideline ^{13}C NMR spectra were also measured to follow the light-induced change in orientational order of an oriented liquid-crystalline side-chain polymer film (Fig. 1b) [8].

NMR imaging

NMR imaging of rigid polymers is challenged by short transverse relaxation times, which require special solid-state imaging techniques, unless images of the soft fractions suffice. Else, high excitation power, small samples, and line-narrowing techniques like MAS (magic angle spinning) or isotope enrichment of the sample need to be applied [18,120–122]. Information on molecular order and dynamics can be extracted from spatially resolved wide-line spectra of samples labelled by ^{2}H at selected chemical sites when the spatial information is encoded in the narrow double quantum resonance, an approach which has been demonstrated on a phantom constructed from drawn poly(ethylene) [123,125]. On the other hand, the ^{13}C resonance is sufficiently narrow to enable space encoding, albeit at the expense of long measurement times due to the low natural abundance of the nucleus. This has been demonstrated with a spectroscopic ^{13}C image of a tensile bar from syndiotactic poly(propylene), which revealed the skin-core layer structure of the object that resulted from the orientation and associated inhomogeneous cooling of the material during injection molding [124,125].

Special multi-pulse NMR line-narrowing sequences can sufficiently extend the duration of the ^{1}H NMR signal for space encoding and give access to relaxation rates sensitive to defect structures in rigid polymers. In this way, polycarbonate samples drawn to different elongation ratios up to $\lambda = 2.7$ have been imaged with the multi-pulse relaxation time as a contrast parameter [126]. In the necking region, the relaxation rate was increased due to immobilization of the small amplitude phenylene motion corresponding to a temperature shift of 10 K. Moreover, two crossing shear bands were clearly visible in an NMR image, whereas they were far less resolved in a polarization microscopy image.

In a detailed study, ^{1}H NMR imaging served among others to yield the chain director distribution in macroscopic sections derived from a frozen contraction flow of a main-chain liquid crystalline polymer [127]. The crack-growth resistance of ABS, a blend of poly(styrene-*co*-acrylonitrile) with poly(butadiene) and PBT/PTMO, a block copolymer of poly(butylene terephthalate)/poly(tetramethylene oxide) was studied by ^{1}H MRI of the crack tip with a dedicated stretching device that allowed to keep notched materials under load inside the magnet during imaging [128]. Numerous damage bands appeared in the images of strained ABS, which converged toward the crack tip and remained upon unloading. The image contrast was due to reduced material density. With the same setup, notched specimens of two different types of extruded polyamide 6 and maleic anhydride grafted ethylene-propylene blends were examined under critical load, where one blend contained pure rubber particles dispersed in the PA6 matrix, and the other contained PA6 occlusions within the rubber particles [126]. MRI experiments revealed a gradual increase of rubber cavitation toward the crack tip, whereby the tougher blend with the occlusions had a significantly more extended plastic zone ahead of the crack tip.

SUMMARY

Mechanical deformation of polymer materials changes the mobility and alignment of their constituting macromolecules. These properties can be probed by NMR in terms of NMR relaxation times and resonance frequencies. Relaxation times are primarily determined by molecular motion, whereas resonance frequencies are determined by the impact of average molecular order on anisotropic spin interactions between ^{1}H nuclei, ^{13}C chemical shifts, and ^{2}H isotope labels. The NMR modalities of spectroscopy and relaxometry have been employed individually and

combined with spatial resolution in NMR images to unravel many details of the molecular response to strain and pressure on a space scale ranging from the chain segment to a macroscopic sample section. While the execution of most NMR techniques demands the skills of experts, NMR relaxometry inside and outside the magnet is simple to use and has found its way to elastomer manufacturing sites, providing valuable information on cross-link density, quality of mixing, and aging. Investigations of the polymer response to static and dynamic strain, on the other hand, have greatly contributed to the principle understanding of the impact of deformation on molecular dynamics, order, and polymer morphology on the way to real-time monitoring of polymer processing steps and the conception of ecologically sound, smart, and responsive polymer materials.

References

1. G.H. Michler, Atlas of Polymer Structures: Morphology, Deformation and Fracture Structures, Carl Hanser Verlag, München, 2016
2. S. Kotzenburg, M. Maskos, O. Nuyken, Polymere: Synthese, Eigenschaften und Anwendungen, Springer, Berlin, 2014
3. H.G. Elias, Macromolecules, volumes 1-4, Wiley-VCH, Weinheim, 2009
4. D.W. van Krevelen, Properties of Polymers, 3rd ed., Elsevier, Amsterdam, 1990
5. B. Blümich, Essential NMR, 2nd ed., Springer, Berlin, 2019
6. K. Hatada, T. Kitayama, NMR Spectroscopy of Polymers, Springer, Berlin, 1994
7. K. Schmidt-Rohr, H.W. Spiess, Multi-dimensional solid-state NMR and polymers, Academic Press, London, 1994
8. U. Wiesner, K. Schmidt-Rohr, C. Boeffel, U. Pawelzik, H.W. Spiess, Solid-state ^{13}C-NMR on oriented films of liquid crystalline polymers, Adv. Mat. 2 (1990) 484-487
9. F. Casanova, J. Perlo, B. Blümich, eds., Single-Sided NMR, Springer, Berlin, 2011
10. K. Hailu, R. Fechete, D.E. Demco, B. Blümich, Segmental anisotropy on strained elastomers detected with a portable scanner, Solid State Nucl. Magn. Reson. 22 (2002) 237–243
11. B. Blümich, Introduction to compact NMR: A review of methods, Trends Anal. Chem. 83 (2016) 2-11
12. B. Blümich, S. Haber-Pohlmeier, W. Zia, Compact NMR, de Gruyter, Berlin, 2014
13. M.L. Johns, E.O. Fridjonsson, S.J. Vogt, A. Haber, eds., Mobile NMR and MRI, R. Chem. Soc, Cambridge, 2016
14. R. Kimmich, Nuclear Magnetic Relaxation and Molecular Dynamics, R. Chem. Soc., Cambridge, 2024
15. R. Kimmich, Principles of Soft-Matter Dynamics: Basic Theories, Non-invasive Methods, Mesoscopic Aspects, Springer, Berlin, 2012
16. F. Casanova, J. Perlo, B. Blümich, Single-Sided NMR, Springer, Berlin, 2011
17. P.T. Callghan, Principles of Nuclear Magnetic Resonance Microscopy, Clarendon Press, Oxford, 1991
18. B. Blümich, NMR Imaging of Materials, Clarendon Press, Oxford, 2000
19. R. Kimmich, NMR Tomography, Diffusometry, Relaxometry, Springer, Berlin, 2011
20. B. Blümich, W. Kuhn, eds., Magnetic Resonance Microscopy – Methods and Applications in Materials Science, VCH, Weinheim, 1992
21. P. Blümler, B. Blümich, R. Botto, E. Fukushima, eds., Spatially Resolved Magnetic Resonance – Methods, Materials, Medicine, Biology, Rheology, Geology, Ecology, Hardware, Wiley-VCH, Weinheim, 1998
22. S.L. Codd, J.D. Seymour, eds., Magnetic Resonance Microscopy – Spatially Resolved NMR Techniques and Applications, Wiley-VCH, Weinheim, 2009
23. S. Haber-Pohlmeier, B. Blümich, L. Ciubanu, eds., Magnetic Resonance Microscopy – Instrumentation and Applications in Engineering, Life Science, and Energy Research, Wiley-VCH, Weinheim, 2022
24. P.T. Callaghan, Translational Dynamics and Magnetic Resonance, Oxford University Press, Oxford, 2011
25. M.G. Brereton, NMR study of the molecular anisotropy induced in a strained rubber network, Macromolecules 26 (1993) 1152–1157
26. M.G. Brereton, NMR transverse relaxation function calculated for constrained polymer chains: application to entanglements and networks, Macromolecules 23 (1990) 1119–1131

27. M. Warner, P.T. Callaghan, E.T. Samulski, Nuclear magnetic resonance line shape from strained Gaussian networks, Macromolecules 30 (1997) 4733–4736
28. M. Knörgen, H. Menge, G. Hempel, H. Schneider, M.E. Ries, Polymer Communication 43 (2002) 4091–4096
29. G. Simon, H. Schneider, M_C-determination in elastomers by ^{1}H-NMR relaxation and ^{2}H-NMR spectroscopy, Makromol. Chem. Macromol. Symp. 52 (1991) 233–246
30. U. Heuert, M. Knörgen, H. Menge, G. Scheler, H. Schneider, New aspects of transversal ^{1}H-NMR relaxation in natural rubber vulcanizates, Polym. Bull. 37 (1996) 489–496
31. P.T. Callaghan, E.T. Samulski, Molecular ordering and the direct measurement of weak proton-proton dipolar interactions in a rubber network, Macromolecules 30 (1997) 113–122
32. P. Sotta, C. Fülber, D.E. Demco, B. Blümich, H.W. Spiess, Effect of Residual Dipolar Interactions on the NMR Relaxation in Cross-Linked Elastomers, Macromolecules 29 (1996) 6222–6230
33. J. Kolz, J. Martins, K. Kremer, T. Mang, B. Blümich, Investigation of the elastomer-foam production with Single-Sided NMR, KGK 60 (2007) 179–183
34. F. Zhao, Z. Ping, S. Zhao, Y. Jian, W. Kuhn, Characterization of Elastomer Networks by NMR Parameters Part I. Sulfur cured NR networks, KGK 60 (2007) 554–558
35. W. Kuhn, P. Barth, S. Hafner, G. Simon, H. Schneider, Material Properties Imaging of Cross-Linked Polymers by NMR, Macromolecules 27 (1994) 5773–5779
36. P. Blümler, B. Blümich, NMR Imaging of Elastomers: A Review, Rubber Chemistry and Technology 70 (1997) 468–518
37. G. Zimmer, A. Guthausen, B. Blümich, Characterization of cross-link density in technical elastomers by the NMR-MOUSE, Solid State Nucl. Magn. Reson. 12 (1998) 183–190
38. B. Blümich, D. Jaschtschuk, C. Rehorn, Advances and Adventures with Mobile NMR, in: S. Sabina Haber-Pohlmeier, B. Blümich, L. Ciobanu, Magnetic Resonance Microscopy, pp. Wiley, VCH, Weinheim, pp. 155–172
39. K. Saalwächter, Microstructure and molecular dynamics of elastomers as studied by advanced low-resolution nuclear magnetic resonance methods, Rubber Chem. Tech. 85 (2012) 350–386
40. K. Saalwächter, Proton multiple-quantum NMR for the study of chain dynamics and structural constraints in polymeric soft materials, Prog. Nucl. Magn. Reson. Spectr. 51 (2007) 1–35
41. M. Ott, R. Pérez-Aparicio, H. Schneider, P. Sotta, K. Saalwächter, Microscopic Study of Chain Deformation and Orientation in Uniaxially Strained Polymer Networks: NMR Results versus Different Network Models, Macromolecules 47 (2014) 7597–7671
42. A. Naumova, D.C. Agudelo, M.A. Villar, D.A. Vega, J.L. Valentin, K. Saalwächter, Microscopic State of Polymer Network Chains upon Swelling and Deformation, Macromolecules 52 (2019) 5042−5053
43. M.G. Brereton, NMR Study of Molecular Anisotropy in a Strained Rubber Network, Macromolecules 26 (1993) 1152–1157
44. Z. Xia, Y. Wang, K. Gong, W. Chen, An in situ stretching instrument combined with low field nuclear magnetic resonance (NMR): Rheo-Spin NMR, Rev. Sci. Instrum. 93 (2022) 033905
45. B. Blümich, Essential NMR, 2nd edition, Springer Nature, Cham, 2029, p. 135
46. J. Che, S. Toki, J.L. Valentin, J. Brasero, A. Nimpaiboon, L. Rong, B.S. Hsiao, Chain Dynamics and Strain-Induced Crystallization of Pre- and Postvulcanized Natural Rubber Latex Using Proton Multiple Quantum NMR and Uniaxial Deformation by in Situ Synchrotron X‑ray Diffraction, Macromolecules 45 (2012) 6491−6503
47. F. Wang, S. Chen, Q. Wu, R. Zhang, P. Sun, Strain-induced structural and dynamic changes in segmented polyurethane elastomers, Polymer 163 (2019) 154–1614
48. K. Fukumori, T. Kurauchi, O. Kamigaito, Pulsed NMR Study of Elastomeric Block Copolymer under Deformation, J. Appl. Polym. Sci. 38 (1989) 1313–133
49. V.M. Litvinov, Strain-Induced Phenomena in Amorphous and Semicrystalline Elastomers. Solid State ^{1}H NMR T_2 Relaxation under Uniaxial Compression, Macromolecules 34 (2001) 8468–8474
50. S. Kariyo, S. Stapf, Influence of Cross-Link Density and Deformation on the NMR Relaxation Dispersion of Natural Rubber, Macromolecules 35 (2002) 9253–9255

51. R. Fechete, D.E. Demco, B. Blümich, Segmental Anisotropy in Strained Elastomers by ^{1}H NMR of Multipolar Spin States, Macromolecules 35 (2002) 6083–6085
52. S. Dupres, D.R. Long, P.-A. Albouy, P. Sotta, Local Deformation in Carbon Black-Filled Polyisoprene Rubbers Studied by NMR and X-ray Diffraction, Macromolecules 42 (2009) 2634–2644
53. R. Pérez-Aparicio, M. Schiewek, J.L. Valentín, H. Schneider, D.R. Long, M. Saphiannikova, P. Sotta, K. Saalwächter, M. Ott, Local Chain Deformation and Overstrain in Reinforced Elastomers: An NMR Study, Macromolecules 46 (2013) 5549–5560
54. A. Azoug, A. Constantinescu, R. Nevière, G. Jacob, Microstructure and deformation mechanisms of a solid propellant using ^{1}H NMR spectroscopy, Fuel 148 (2015) 39–47
55. H. Kimura, H. Dohi, M. Kotani, T. Matsunaga, K. Yamauchi, H. Kaji, H. Kurosu, T. Asakura, Molecular dynamics and orientation of stretched rubber by solid-state ^{13}C NMR, Polymer J. 42 (2010) 25–30
56. M. Kitamura, Y. Hata, H. Yasuoka, T. Kurotsu, A. Asano, Strain-induced ^{13}C chemical shift change of natural rubber, Polymer J. 44 (2012) 778–785
57. T. Kameda, T. Asakura, Structure and dynamics in the amorphous region of natural rubber observed under uniaxial deformation monitored with solid-state ^{13}C NMR, Polymer 44 (2003) 7539–7544
58. W. Lin, M. Bian, G. Yang, Q. Chen, Strain-induced crystallization of natural rubber as studied by high-resolution solid-state ^{13}C NMR spectroscopy, Polymer 45 (2004) 4939–4943
59. H.W. Spiess, Rotation of molecules and nuclear spin relaxation, in: P. Diehl, E. Fluck, R. Kosfeld, eds., NMR: Basic Principles and Progress 15, Springer, Heidelberg, 1978, pp. 55–214
60. K. Schmidt-Rohr, H.W. Spiess, Multi-dimensional solid-state NMR and polymers, Academic Press, San Diego, 1994
61. P. Sotta, B. Deloche, Uniaxiality induced in a strained poly(dimethylsiloxane) network, Macromolecules 23 (1990) 1999–2007
62. M.G. Brereton, M.E. Ries, An Analytic Study of the NMR Properties for for deformed polymer networks blended with free chains, Macromolecules 29 (1996) 2644–2651
63. P. Sotta, Local Order and Induced Orientation in PDMS Model Networks Studied by ^{2}H NMR, Macromolecules 31 (1998) 3872–3879
64. K. McLoughlin, J.K. Waldbieser, C. Cohen, T.M. Duncan, End-Linked Poly(dimethylsiloxane) Elastomers: ^{2}H-Nuclear Magnetic Resonance Investigations of Compression-Induced Segment Anisotropy, Macromolecules 30 (1997) 1044–1052
65. W. Gronski, R. Stadler, M.M. Jacobi, Evidence of Nonaffine and Inhomogeneous Deformation of Network Chains in Strained Rubber-Elastic Networks by Deuterium Magnetic Resonance, Macromolecules 17 (1984) 741–748]
66. M.E. Ries, M.G. Brereton, P.G. Klein, I.M. Ward, P. Ekanayake, H. Menge, H. Schneider, Contributions to the Total Orientation of Deformed Elastomers Arising from the Network Structure and Chain Interactions As Measured by NMR, Macromolecules 32 (1999) 4961-4968
67. H. Menge, P. Ekanayake, M.E. Ries, M.G. Brereton, M. Findeisen, Local order and strain-induced orientation in poly(butadiene) networks studied by 2H NMR, Polymer Bulletin 43 (1999) 371–378
68. C.-D. Poon, E.T. Samulski, A.I. Nakatani, Chain orientation in deformed networks via NMR, Makromolekulare Chemie. Macromol. Symp. 40 (1990) 109–120
69. A. Dardin, R. Stadler, C. Boeffel, H.W. Spiess, Molecular dynamics of new thermoplastic elastomers based on hydrogen bonding complexes: a deuteron nuclear magnetic resonance investigation, Macromol. Chem. 194 (1993) 3467–3477
70. W. Gronski, F. Forster, W. Pyckhout-Hintzen, T. Springer, Molecular aspects of polymer network deformation - small angle neutron scattering and NMR studies, Makromol. Che. Macrom. Symp. 40 (1990) 121–137
71. V.M. Litvinov, H.W. Spiess, Molecular mobility in the adsorption layer and chain orientation in strained poly(dimethylsiloxane) networks by ^{2}H NMR, Die Makromol. Chem. 193 (1992) 1181–1194
72. V.M. Litvinow, R.A. Orza, M. Klüppel, M. van Duin, P.C.M.M. Magusin, Rubber-Filler Interactions and Network Structure in Relation to Stress-Strain Behavior of Vulcanized, Carbon Black Filled EPDM, Macromolecules 44 (2011) 4887–4900

73. B. Deloche, E.T. Samulski, Short-range nematic-like orientational order in strained elastomers: a deuterium magnetic resonance study, Macromolecules 14 (1981) 575–581
74. B. Deloche, A. Dubault, J. Herz, A. Lapp, Orientation of Free Polymer Chains Dissolved in a Strained Elastomer: A Deuterium Magnetic-Resonance Study, Europhysics Letters 1 (1986) 629–635
75. S. Valić, P. Judeinstein, B. Deloche, Analysis of deuterium NMR spectra of probe chains diffusing in a stretched polybutadiene network, Polymer 44 (2003) 5263–5267
76. J. Rault, J. Marchal, P. Judeinstein, P.A. Albouy, Chain orientation in natural rubber, Part II: ^{2}H-NMR study, The European Physical Journal E, 21 (2006) 243–261
77. J. Rault, J. Marchal, P. Judeinstein, P.A. Albouy, Stress-Induced Crystallization and Reinforcement in Filled Natural Rubbers: ^{2}H NMR Study, Macromolecules 39 (2006) 8356–8368
78. P. Sotta, B. Deloche, J. Herz, Effect of dilution on the orientational order induced in strained polymer networks, as measured by ^{2}H nuclear magnetic resonance, Polymer 29 (1988) 1171–1178
79. R. Tycko, F.J. Blanco, Y. Ishii, Alignment of Biopolymers in Strained Gels: A New Way To Create Detectable Dipole−Dipole Couplings in High-Resolution Biomolecular NMR, J. Am. Chem. Soc. 122 (2000) 9340–9341
80. Y. Ishii, M.A. Markus, R. Tycko, Controlling residual dipolar couplings in high-resolution NMR of proteins by strain induced alignment in a gel, Journal of Biomolecular NMR 21 (2001) 141–151
81. J.C. Freudenberger, P. Spiteller, R. Bauer, H. Kessler, B. Luy, Stretched Poly(dimethylsiloxane) Gels as NMR Alignment Media for Apolar and Weakly Polar Organic Solvents: An Ideal Tool for Measuring RDCs at Low Molecular Concentrations J. Am. Chem. Soc. 126 (2004) 14690–14691
82. B. Blümich, Anferova, S., Sharma, S., Segre, A.L., Federici, C., Unilateral NMR for Quality Control: The NMR-MOUSE®, Spectroscopy 18 (2003) 18–32
83. P. Blümler, B. Blümich, Investigation of Stress Distributions in Filled Polysiloxanes by NMR Imaging, Acta Polymerica 44 (1993) 125–131
84. K.K. Goga N.O., Blümich B., Zerstörungsfreie Qualitätskontrolle in der Reifenproduktion: Die „NMR-MOUSE“, GAK Gummi Fasern Kunststoffe 58 (2005) 104–108
85. H. Yasunaga, H. Kurosu, I. Ando, Spatial information on a polymer gel as studied by proton NMR imaging. 1. Image analysis of stress-strain, Macromolecules 25 (1992) 6505–6509
86. M. Klinkenberg, P. Blümler, B. Blümich, ^{2}H NMR Imaging of Strained Elastomers, J. Magn. Reson. Series A 119 (1996) 197–203
87. M. Klinkenberg, P. Blümler, B. Blümich, ^{2}H-NMR Imaging of Stress in Strained Elastomers†, Macromolecules 30 (1997) 1038–1043
88. M. Schneider, D.E. Demco, B. Blümich, ^{1}H NMR imaging of residual dipolar couplings in cross-linked elastomers: dipolar-encoded longitudinal magnetization, double-quantum, and triple-quantum filters, J. Magn. Reson. 140 (1999) 432–441.
89. M. Schneider, D.E. Demco, B. Blümich, NMR Images of Proton Residual Dipolar Coupling from Strained Elastomers, Macromolecules 34 (2001) 4019–4026
90. J.L. Herberg, S.C. Chinn, A.M. Sawvel, E. Gjersing, R.S. Maxwell, Characterization of local deformation in filled-silicone elastomers subject to high strain – NMR MOUSE and Magnetic Resonance Imaging as a diagnostic tool for detection of inhomogeneities, Polym. Degrad. Stabil. 91 (2006) 1701–1710
91. B.P. Mayer, J.A. Reimer, R.S. Maxwell, A Methodology for the Indirect Determination and Spatial Resolution of Shear Modulus of PDMS−Silica Elastomers, Macromolecules 41 (2008) 1323–1327
92. D. Hauck, P. Blümler, B. Blümich, NMR imaging of technical SBR vulcanizates under dynamic mechanical load, Macromol. Chem. Phys. 198 (1997) 2729–2742
93. W. Selby, P. Garland, I. Mastikhin, Dynamic mechanical analysis with portable NMR, J. Magn. Reson. 339 (2022) 107211
94. W. Selby, B.J. Balcom, B. Newling, I. Mastikhin, Using phase interference to characterize dynamic properties—a review of constant gradient, portable magnetic resonance methods, Frontiers in Physics 11 (2023) 1201032
95. R. Muthupillai, D.J. Lomas, P.J. Rossman, J.F. Greenleaf, A. Manduca, R.L. Ehman, Magnetic Resonance Elastography by Direct Visualization of Propagating Acoustic Strain Waves, Science 269 (1995) 1854–1857

96. I. Sack, G. Buntkowsky, J. Bernarding, J. Braun, Magnetic Resonance Elastography: A Method for the Noninvasive and Spatially Resolved Observation of Phase Transitions in Gels, J. Am. Chem. Soc. 123 (2001) 11087–11088
97. S. Catheline, J.-L. Gennisson, G. Delon, M. Fink, R. Sinkus, S. Abouelkaram, J. Culioli, Measurement of viscoelastic properties of homogeneous soft solid using transient elastography: An inverse problem approach, J Acoust. Soc. Am. 116 (2004) 3734–3741
98. G. Madelin, N. Baril, J.D. de Certaines, J.-M. Franconi, E. Thiaudière, NMR Characterization of Mechanical Waves, in: Annual Reports NMR Spectr. 53 (2004) 203–244
99. R. Muthupillai, R.L. Ehman, Magnetic resonance elastography, Nature Medicine, 2 (1996) 601–603
100. R.J. Okamoto, E.H. Clayton, P.V. Bayly, Viscoelastic properties of soft gels: comparison of magnetic resonance elastography and dynamic shear testing in the shear wave regime, Phys. Med. Biol. 56 (2011) 6379
101. S. Hirsch, F. Beyer, J. Guo, S. Papazoglou, H. Tzschaetzsch, J. Braun, I. Sack, Compression-sensitive magnetic resonance elastography, Phys. Med. Biol. 58 (2013) 5287
102. G. Low, S.A. Kruse, D.J. Lomas, General review of magnetic resonance elastography, World J. Radiol. 8 (2016) 59–72
103. I. Sack, Magnetic resonance elastography from fundamental soft-tissue mechanics to diagnostic imaging, Nature Reviews Physics 5 (2023) 25–42
104. R.A.C. Deblieck, D.J.M. van Beek, K. Remerie, I.M. Ward, Failure mechanisms in polyolefines: The role of crazing, shear yielding and the entanglement network, Polymer 52 (2011) 2979–2990
105. J.A. Sauer, Deformation, yield and fracture of polymers at high pressure, Polymer Engineering & Science 17 (1977) 150–164
106. A. Adams, B. Blümich, Single-Sided NMR of Semicrystalline Polymers, Macromol. Symp. 327 (2013) 29–38
107. B. Blümich, F. Casanova, A. Buda, K. Kremer, T. Wegener, Mobile NMR for Analysis of Polyethylene Pipes, Acta Physica Polonica A 108 (2005) 13–23
108. A. Adams, M. Adams, B. Blümich, H.-J. Kocks, O. Hilgert, S. Zimmermann, Optimierung der Umhüllung von Stahlrohren, 3R international 49 (2010) 216–225
109. C. Hedesiu, D.E. Demco, K. Remerie, B. Blümich, V.M. Litvinov, Study of Uniaxially Stretched Isotactic Poly(propylene) by ^{1}H Solid-State NMR and IR Spectroscopy, Macromol. Chem. Phys. 209 (2008) 734–745
110. L.S. Loo, R.E. Cohen, K.K. Gleason, Chain Mobility in the Amorphous Region of Nylon 6 Observed under Active Uniaxial Deformation, Science 288 (2000) 116–119
111. L.S. Loo, R.E. Cohen, K.K. Gleason, Deuterium nuclear magnetic resonance of deuterium oxide in nylon 6 under active uniaxial deformation, Polymer 41 (2000) 7699–7704
112. C. Li, Z. Xia, L. Wu, Y. Xiong, W. Chen, Strain-Dependent Evolution of the Rigid Amorphous Fraction of Low-Density Polyethylene under Deformation, Macromolecules 58 (2025) 2320–2335
113. F.M. Capaldi, M.C. Boyce, G.C. Rutledge, Enhanced Mobility Accompanies the Active Deformation of a Glassy Amorphous Polymer, Phys. Rev. Lett. 89 (2002) 175505
114. F.M. Capaldi, M.C. Boyce, G.C. Rutledge, Molecular response of a glassy polymer to active deformation, Polymer 45 (2004) 1391–1399
115. [115] M.T. Hansen, B. Bluemich, C. Boeffel, H.W. Spiess, L. Morbitzer, A. Zembrod, Influence of tensile stress on the phenylene flips in polycarbonate studied by two-dimensional solid-state NMR, Macromolecules 25 (1992) 5542–5544
116. D.J. Schaefer, R.J. Schadt, K.H. Gardner, V. Gabara, S.R. Allen, A.D. English, Microscopic Dynamics and Macroscopic Mechanical Deformation of Poly(p-phenyleneterephthalamide) Fibers, Macromolecules 28 (1995) 1152—1158
117. M. Utz, A.S. Atallah, P. Robyr, A.H. Widmann, R.R. Ernst, U.W. Suter, Solid-State NMR Investigation of the Structural Consequences of Plastic Deformation in Polycarbonate. 1. Global Orientational Order, Macromolecules 32 (1999) 6191–6205
118. M. Utz, P. Robyr, U.W. Suter, Solid-State NMR Investigation of the Structural Consequences of Plastic Deformation in Polycarbonate. 2. Local Orientational Order, Macromolecules 33 (2000) 6808–6814
119. P.T. Eles, C.A. Michal, A DECODER NMR Study of Backbone Orientation in Nephila clavipes Dragline Silk under Varying Strain

and Draw Rate, Biomacromolecules 5 (2004) 661–665
120. B. Blümich, P. Blümler, E. Günther, G. Schauss, H.W. Spiess, Nondestructive Evaluation of Polymer Materials by Solid-State NMR Imaging, Makromol. Chem. Macromol. Symp. 44 (1991) 37–45
121. U. Scheler, G. Schauβ, B. Blümich, H.W. Spiess, Spatially resolved solid-state MAS-NMR-spectroscopy, Solid State Nucl. Magn. Reson. 6 (1996) 375–388
122. E. Günther, B. Blümich, H.W. Spiess, Spectroscopic imaging of solids by deuteron magic-angle-spinning NMR, Chem. Phy. Lett. 184 (1991) 251–255
123. E. Günther, B. Blümich, H.W. Spiess, Deuteron double-quantum NMR imaging of molecular order and mobility in solid polymers, Molecular Physics 71 (1990) 477–489
124. B. Blümich, P. Blümler, E. Günther, J. Jansen, G. Schauß, H.W. Spiess, NMR Imaging of Polymers: Methods and Applications, in: B. Blümich, W. Kuhn, eds., Magnetic Resonance Microscopy: Methods and Applications in Materials Science, Agriculture, and Biomedicine, VCH, Weinheim, 1992
125. P. Blümler, B. Blümich, E. Günther, H.W. Spiess, Methods and applications of NMR imaging in polymer research, Polymer Preprints 33 (1992) 759–760
126. B. Traub, S. Hafner, U. Wiesner, H.W. Spiess, Investigation of Mechanical Deformation in Rigid Polymers by 2D Solid-State NMR Imaging, Macromolecules 31 (1998) 8585–8589
127. M. Gentzler, S. Patil, J.A. Reimer, M.M. Denn, Molecular motion and orientation distributions in melt-processed, fully aromatic liquid crystalline polyesters from ^{1}H NMR, Solid State Nucl. Magn. Reson. 12 (1998) 97–112
128. P. Adriaensens, L. Storme, R. Carleer, D. Vanderzande, J. Gelan, V.M. Litvinov, R. Marissen, Visualization of Tensile Stress Induced Material Response at a Crack Tip in Polymers under Critical Load by NMR Imaging, Macromolecules 33 (2000) 4836–4841
129. P. Adriaensens, L. Storme, R. Carleer, J. D'Hae, J. Gelan, V.M. Litvinov, R. Marissen, J. Crevecoeur, NMR Imaging Study of Stress-Induced Material Response in Rubber Modified Polyamide 6, Macromolecules 35 (2002) 135–140

Nanomaterials and Polymers Innovations Vol. 1, No. 1 (2025); 19-31
ISSN: 3102-0798 (Online). Available online at www.nepalpolymer.org
DOI: https://doi.org/.....xyz.....xyz (to be updated)

Original research paper

Cellulose Nanocrystals-Based Nanocomposites for Magnetic Solid-Phase Extraction of PAHs from Water Samples

Luciana Costa dos Reis[1], Isabella Karoline Ribeiro Dias[2], Valdeir Arantes[2], Elizabete Fernandes Lucas[1,3*], Bluma Guenther Soares[1,3]

[1]*Universidade Federal do Rio de Janeiro, Instituto de Macromoléculas Professora Eloisa Mano, Rio de Janeiro, Brazil; elucas@ima.ufrj.br*

[2]*Universidade de São Paulo, Escola de Engenharia de Lorena, Departamento de Biotecnologia Industrial/DEBIQ, Lorena, Brazil*

[3]*Universidade Federal do Rio de Janeiro, Programa de Engenharia Metalúrgica e de Materiais/COPPE, Rio de Janeiro, Brazil*

ORCID: 0000-0002-9454-9517 (EFL), ORCID: 0000-0002-1273-7574 (BGS), and ORCID: 0000-0001-9461-7914 (LCdR)

Abstract: An eco-friendly magnetic nanocomposite based on cellulose nanocrystals (CNCs) was synthesized through a rapid and straightforward method, utilizing electrostatic interactions between Fe_2O_3 nanoparticles and CNCs (CNCs/Fe_2O_3). These nanocomposites were characterized by scanning electron microscopy-energy dispersive X-ray spectrometry (SEM-EDX) and Fourier transform infrared spectroscopy (FTIR). These hybrid materials were effectively employed for the adsorption of three polycyclic aromatic hydrocarbons (PAHs), naphthalene, fluorene and pyrene from water samples, using magnetic solid-phase extraction (MSPE) as the preconcentration technique. Among the tested formulations, the CNCs/Fe_2O_3 with a mass ratio of 3/1 demonstrated the highest adsorption capacity for all three PAHs. The following order was observed for the extraction efficiency: pyrene > fluorene > naphthalene. MSPE process was optimized using a Plackett–Burman design to identify the most influential experimental parameters.

Keywords: cellulose nanocrystals; polycyclic aromatic hydrocarbons; preconcentration; sorbent

शोधसार: प्रस्तुत अनुसन्धानमा फेरिक अक्साइड र सेलुलोजका नानोकणिकाहरु बिचको स्थिर विद्युतिय अन्तरक्रियाको उपयोग गरेर चुम्बकीय गुणयुक्त वातावरणमैत्री नानोसमिश्रण संश्लेषण गर्ने छिटो र सरल विधिको अध्ययन गरिएको थियो । यसरी तयार गरिएका समिश्रणहरूको अनेकन विशेषताहरु निर्धारण गर्नका लागि स्क्यानिङ इलेक्ट्रोन माइक्रोस्कोपी–इनर्जी डिस्पर्सिभ एक्स-रे स्पेक्ट्रोमेट्री (SEM-EDX) र फोरिएर ट्रान्सफर्म इन्फ्रारेड स्पेक्ट्रोस्कोपी जस्ता उपकरणहरु प्रयोग गरिएका थिए । उक्त समिश्रणहरूलाई *चुम्बकीय ठोस निष्कर्षण प्रविधि* (MSPS) समेत अपनाएर पानीलाई नराम्ररी दुषित गर्ने ३ बिभिन्न प्रकारका पोलिएरोम्याटिक हाइड्रोकार्बनहरू (जस्तैः नाफ्थालिन, फ्लोरिन र पाइरिन) को प्रभावकारी अवशोषणका लागि प्रयोग गरियो । परीक्षण गरिएका नमुनाहरू मध्ये सेलुलोज र फेरिक अक्साइडका नानोकणिकाहरुको मात्रात्मक अनुपात ३:१ रहेको नानोसमिश्रणले देहाय अनुसारको क्रममा सर्वोत्तम अवशोषण क्षमता प्रदर्शन गरेको पाईयो: पाइरिन > फ्लोरिन > नाफ्थालिन । निष्कर्षमा दुषित-जल-प्रशोधन प्रयोजनार्थ प्रभावी प्रयोगात्मक सुचकहरूको पहिचान हेतु प्लाकेट्-बर्मन डिजाइनको उपयोग गरी उल्लेखित चुम्बकीय ठोस निष्कर्षण प्रविधिको पनि सुधार गरिएको थियो ।

INTRODUCTION

Water is extensively used in the petroleum industry to enhance oil production. The resulting byproduct, known as produced water or oily water, is extracted from the reservoir alongside crude oil. This mixture

Corresponding author, E-mail: *elucas@ima.ufrj.br*
© Nepal Polymer Institute, Kathmandu, Nepal
Received: April 25, 2025; Revised: May 11, 2025, Accepted: May 12, 2025; Published: May 19, 2025

comprises formation water (naturally occurring water within the reservoir) and connate water (injected water used to boost oil extraction and maintain the reservoir pressure). Produced water contains elevated level of organic pollutants, notably polycyclic aromatic hydrocarbons (PAHs) (Amakiri et al., 2024). Other prevalent contaminants include BTEX compounds (benzene, toluene, ethylbenzene, xylenes, and phenol), all classified as high-priority chemicals by the EPA (2019) and WHO (2019). Nowadays, global oil production increases to supply energy demand. Consequently, the volume of produced water also escalates. (Amakiri et al., 2022).

PAHs are persistent organic pollutants characterized by two or more condensed aromatic rings. They are hazardous to both the environment and human health, exhibiting carcinogenic, mutagenic, and immunosuppressive properties (EPA, 2019; WHO 2019). The discharge of the produced water into marine environments is a significant source of PAH contamination. Studies have identified and quantified PAHs in oily water samples (Binet et al., 2011; Gabardo et al., 2011; Venkatesan and Wankat, 2017). PAHs present low water solubility, low volatility, and tend to accumulate in organisms and aquatic sediments (Zhang et al., 2016).

Concentrations of PAHs in produced water range from about 0.01 µg L^{-1} to 1512 µg L^{-1}, with naphthalene and fluorene among the most prevalent (**Table 1**) (Pampani and Sydnes, 2013; Petrobras, 2021). Variations in concentration levels are attributed to differences in oil field locations and reservoir characteristics.

Naphthalene is genotoxic and induces tumors in experimental animals (IARC, 1985; IARC, 2012). Additionally, naphthalene irritates human skin and can cause allergic reaction in both humans and animals (IARC, 2012). Fluorene is not classified as a carcinogen; however, studies on oral exposure in humans demonstrated a decrease in red blood cell count, packed cell volume, and hemoglobin levels (EPA, 1990a). Pyrene is not classified as carcinogenic by the EPA (1990b); nevertheless, it is a skin irritant, a suspected mutagen, and a possible tumor-causing agent (EPA, 1990b).

Table 1. Concentration values (µg L^{-1}) of major PAHsin produced water from various marine regions (Pampanim and Sydnes, 2013; PETROBRAS, 2021.

Compound	Great Britain North Sea[a]	Scotian Shelf Canada[a]	North America Gulf of Mexico[a]	Brazil Santos Basin FPSO* Mangaratiba[b]	Brazil Santos Basin FPSO* P-66 Angra dos Reis[b]
Pyrene	0.03 - 1.9	0.36	0.01 - 0.29	0 - 0.40	<0.05 - 0.12
Naphthalene	237 – 394	1512	5.3 - 90.2	17.3 - 33.5	20.2 - 80.3
Fluorene	2.6 - 21.7	13	0.06 - 2.8	1.2 - 1.8	0.80 - 4
Phenanthrene	1.3 - 32.0	4.0	0.11 - 8.8	0 - 7.0	2.7 – 16.5
Anthracene	ND	0.26	0.45	ND	<0.05
Total PAHs	419 - 1559	2148	40 - 600	27.6 - 39	23.8 - 101

[a] (Pampanim and Sydnes, 2013);
[b] (PETROBRAS, 2021).
*Floating Production Storage Offloading Unit

Produced water treatment typically occurs at the oil field surface, utilizing separation tanks, hydrocyclones and floaters units. The disposal process follows the guideline established by CONAMA Resolution 393/2007, which allows for an average concentration of oil and grease up to 29 mg L^{-1}, and a maximum daily limit of 42 mg L^{-1} (CONAMA, 2007; Petrobras, 2022). For marine disposal, the resolution also establishes monitoring of additional parameters, including organic

compounds (PAHs, BTEX, phenols and evaluation of total hydrocarbons) (CONAMA, 2007).

Precisely measuring PAH levels in water samples is crucial to ensure adherence to environmental regulations. This requires effective sample preparation and extraction techniques. The common analytical techniques for PAHs detection include high-performance liquid chromatography (HPLC) with UV-visible or fluorescence detection, gas chromatography-mass spectrometry (GC-MS), and fluorescence spectroscopy (Gratz et al., 2000; Song et al., 2012).

Gabardo et al. collected water samples from Guanabara Bay (Rio de Janeiro, Brazil), storing them in dark containers at temperatures below 5 °C. PAHs were extracted using liquid-liquid extraction with n-hexane and analyzed by UV-fluorescence spectrometry. PAHs concentrations ranged from 0.04 to 24.48 μg L^{-1} (Gabardo et al., 2001).

Delgado et al. collected seawater samples from a Spanish beach near an oil industry and analyzed the presence of PAHs by liquid chromatograph equipped with a scanning fluorescence detector. Subsequent quantification by HPLC allowed the determination of 13 PAHs, with limits of detection up to 23 mg L^{-1} and an average total relative standard deviation (RSD) of 9.2 % (Delgado et al., 2004).

Analyzing PAHs in water requires indirect methods, as direct detection is often challenging due to the complex composition of the produced water. Therefore, the determination of the concentration of each compound requires a sample preparation process, including efficient extraction techniques. One of the miniaturized extraction techniques that has been widely used for the extraction of PAHs is magnetic solid phase extraction (MSPE). This is a miniaturized method that becomes popular for PAH extraction. In MSPE, a magnetic hybrid adsorbent is dispersed in the liquid sample, favoring interaction between the sample and the extracting solid phase (Šafaříková and Šafařík, 1999). The magnetic component allows for easy handling using an external magnetic field (magnet), while the extracting phase adsorbs the target analytes through various chemical interactions (Sasaki and Tanaka, 2011). Selecting appropriate adsorbent materials enhances extraction selectivity and efficiency, and, in some cases, the materials can be reused (Yaping et al., 2014).

The magnetic phase in MSPE technique often consists of iron-based minerals or iron oxides, such as magnetite (Fe_3O_4) or maghemite (γ-Fe_2O_3). The extracting phase may include organic and inorganic compounds forming composites (Yang et al., 2019). Some of them include carbon nanotubes integrated into iron-based metal-organic frameworks (Yang et al., 2022), or graphene oxide modified with polyaniline (Manousi et al., 2021) among others. The main adsorption mechanism for PAHs is based on π-π interactions between the aromatic structures and those of the adsorbent material. Consequently, an ideal solid adsorbent should possess a high surface area and abundant conjugated double bonds (Zhang et al., 2011). Carbon-based materials are commonly used for PAH adsorption due to their high specific surface area and presence of π orbitals (Kong et al., 2011).

The cellulose nanocrystals (CNCs) are renewable nanomaterial that serve as green alternatives to traditional sorbents for the sample preparation techniques due to their biocompatibility, biodegradability, and chemical stability (Dufresne, 2013). CNCs exhibit strong intermolecular and intramolecular hydrogen bonds enhancing their reactivity (Ruiz-Palomero et al., 2017). Additionally, CNCs can be easily coupled with magnetic nanoparticles to form magnetic nanocomposites, offering efficient and economical options for preconcentration, clean-up and extraction operations. These composites are hydrophilic with controlled retention of the target analytes and can be rapidly recovered using a magnet (Abujaber et al., 2019).

The multifunctional properties of the nanocellulose-based offer significant advantages in the application of adsorbent composite materials (Soares et al., 2024). These materials have garnered attention in the treatment of heavy metal wastewater due to their increased number of adsorption active sites and greater biocompatibility (Habibi, 2014; Bhatnagar et al., 2015). These inherent qualities make it suitable as a material for oil-water separation. Bio-based nanocellulose materials are also effective in the adsorption and degradation of organic pollutants due to their excellent physicochemical properties (Aoudi et al., 2022). Nanocellulose can remove several pollutants from water such as heavy metal ions, nitrates, phosphates, dyes, oils, pesticides and

pharmaceuticals due to the possibility of modifying their hydroxyl groups (Mautner, 2020).

In this work, cellulose nanocrystals (CNCs), previously produced by an enzyme-mediated method (Arantes et al., 2020a), an eco-friendly and low-cost method compared to traditional processes, was used to synthesize a magnetic nanocomposite. In aqueous solution, the CNCs are dispersed and negatively charged, allowing the formation of a nanocomposite through electrostatic attraction with positively charged iron oxide (Fe_2O_3) magnetic nanoparticles. The magnetic composite was employed as a sorbent in the MSPE technique. This technique, using the newly produced CNCs/Fe_2O_3 nanocomposite, enabled the isolation and preconcentration of naphthalene, fluorene and pyrene in water. These PAHs were selected due to their high abundance in the produced water by the petroleum industry.

MATERIALS AND METHODS

Materials

The CNCs sample used in the synthesis of the magnetic nanocomposite was previously obtained by enzyme-mediated isolation from a Eucalyptus bleached Kraft pulp according to the literature (Arantes et al., 2020a; 2020b) and dispersed in water at a concentration of 0.3 wt%. $FeCl_3$-$6H_2O$ and $FeSO_4$-$7H_2O$, as well as naphthalene, fluorene and pyrene (analytical standard) were purchased from Sigma-Aldrich (St. Louis, MO, USA), NaOH (97 % purity, pellets) and HNO_3 65 % were acquire from Vetec Química Fina (Xerém, RJ, Brazil). Distilled water (pH 5) was prepared on a water purification system (Q341) supplied by Quimis. The organic solvents (acetonitrile, hexane, methanol, dichloromethane and pentane) were obtained from Labsynth (Diadema, SP, Brazil). Stock standard solutions of each PAH (100 mg L^{-1}) were prepared in acetonitrile. Working solution (10 mg L^{-1}) of the three PAHs was prepared daily by diluting the stock standard solutions with distilled water. All solutions were stored protected from the light at 4 °C.

Fe_2O_3 synthesis

The magnetic component of nanocomposite, iron oxide (Fe_2O_3), was synthesized exactly according to the literature (Fernández and Vidal, 2016). Briefly, 0.780 g of $FeCl_3.6H_2O$ and 0.400 g of $FeSO_4.7H_2O$ were dissolved in 250 mL of distilled water. Then, a 5 M NaOH solution was added dropwise under constant stirring to precipitate the iron oxide. The resulting Fe_2O_3 nanoparticles were washed with distilled water until the pH of the washings reached 7, separated from non-magnetic nanoparticles using a neodymium magnet, and dried at 60 °C overnight.

Synthesis of CNCs/Fe_2O_3 nanocomposite

The CNCs/Fe_2O_3 nanocomposites were synthesized based on a method described by Costa dos Reis et al. (2017). A dispersion of CNC in distilled water (1 mg mL^{-1}) was prepared using ultrasound energy (Fisherbrand CPX3800) for 1 h. CNC possess hydroxyl (-OH) groups on their surface, which, upon ultrasound treatment, loose hydrogen ion rendering the surface negatively charged. Separately, Fe_2O_3 nanoparticles were dispersed in 1M HNO_3 and sonicated for 30 min to achieve a concentration of 150 mg mL^{-1}. This process produces a positive charge in their surface. The two dispersions were then mixed, and the pH of the mixture (CNCs solution + Fe_2O_3 solution) was adjusted to 2. The mixture was vigorously stirred for 1 h, allowing the electrostatic self-assembly occur, forming the CNCs/Fe_2O_3 nanocomposite. The nanocomposite was separated using an external magnetic field and dried in an oven at 60 °C overnight. CNCs/Fe_2O_3 ratios of 1/1 and 3/1 (w/w) were prepared. **Figure 1** illustrates the synthesis procedure.

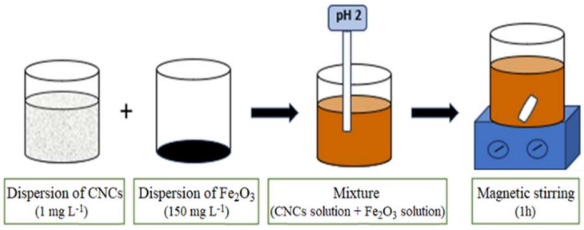

Figure 1. Synthesis procedure of CNCs/Fe_2O_3 nanocomposite.

Magnetic solid-phase extraction procedure

The CNCs/Fe_2O_3 nanocomposite developed in this study was used as adsorbent in the aqueous sample pretreatment technique known as MSPE. The studies employed fluorene, pyrene and naphthalene as model analytes. Standard solutions of each PAH were prepared in acetonitrile at concentrations of 100 mg L^{-1}. A working aqueous solution containing 10 mg L^{-1} of each PAH was then prepared by

diluting the standard solutions. The MSPE procedure is illustrated in **Figure 2**.

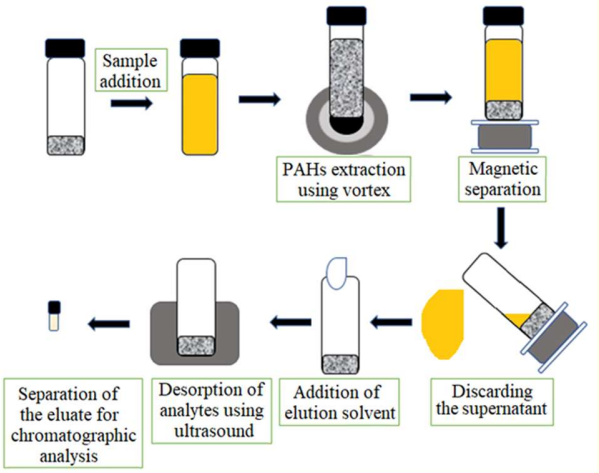

Figure 2. MSPE procedure for the preconcentration of PAHs (prepared by the author).

In the MSPE procedure, 20 mg of CNCs/Fe_2O_3 nanocomposite (1/1 and 3/1 mass ratios) were mixed with 10 mL of work solution. The mixture was agitated for 10 min and the vial was placed on a neodymium magnet to separate the nanocomposite, which was deposited at the bottom due to magnetic attraction. The liquid phase was discarded.

For the adsorption of PAHs, the nanoparticles of the nanocomposite were treated with 0.5 mL of hexane (eluent) in an ultrasonic bath for 5 min. The eluate was separated from the nanocomposite using magnetic separation and transferred to a chromatography vial for analysis. Acetonitrile/dichloromethane mixture was also used as eluent.

Gas chromatography- Flame ionization detection (GC-FID) analysis

Eluates obtained from the MSPE procedure, along with standard solutions containing the three PAHs, were analyzed using a gas chromatograph (Shimadzu, model QP2010) equipped with a split/splitless automatic injector and a flame ionization detector, Japan. A capillary column RTX-5 (diphenyl dimethyl polysiloxane, 30 m x 0.25 mm ID, 0.25 µm film thickness) was used. The injector temperature was set at 250 °C and the injection volume was 1 µL in splitless mode. The oven temperature program was as follows: initially set at 50 °C (held for 3 min), then increased at 30 °C/min to 300 °C (held for 4 min). Helium (99.999 %) at a flow rate of 30 mL min^{-1} was used as carrier gas. The detector temperature was set at 320 °C.

SEM-EDX analysis

The morphology of the nanoparticles was examined using scanning electron microscopy (SEM) with a TESCAN VEGA III microscope (Czech Republic), operating at 20 kV. Elemental analysis was performed with an energy dispersive X-ray (EDX) detector from Bruker Nano GmbH (Germany), model XFlash 630M. EDX microanalysis is an elemental analysis technique associated with SEM, based on the generation of characteristic X-rays that reveals the presence of elements in the sample.

Particle size analysis

Particle size and particle size distribution was determined using a laser diffraction particle size analyzer (Mastersizer 3000, Malvern Instruments). The analyzer employs two light sources: red (632.8 nm) and blue (470 nm), allowing measurement of the hydrodynamic diameter of particles in the range of 10 nm to 3500 µm. Analyses were conducted at low obscuration (0.5 – 4 %), with a stir rotation speed fixed at 3500 rpm, without sonication. The input parameters were manually set to assume a non-spherical particle model, and the refractive index for cellulose (1.4683) was used (Sultanova et al., 2013). Each analysis was performed in duplicate, with three runs, each comprising five successive laser diffraction measurements, totaling 15 readings per sample. Before each analysis, the dispersion unit was automatically cleaned three times with ultrapure water.

Changes in particle size distribution were evaluated by comparing the reduction in peak height after enzymatic treatment to that of the untreated reference pulp (BEKP). The particle size metrics, Dx (10), Dx (50) Dx (90), represent the diameters below which 10 %, 50 % and 90 % of the particles fall, respectively, indicating the distribution of particle sizes within the sample.

FTIR analysis

Fourier Transform Infrared Spectroscopy (FTIR) was employed to investigate the chemical structure of the samples. Measurements were performed using a Perkin Elmer FTIR Spectrometer (Frontier, Perkin Elmer, UK), operating with scanning in the

range of 400 to 4000 cm^{-1}, with a resolution of 1 cm^{-1}, and 32 scans.

Data processing

The optimization of the MSPE conditions was carried out using NEMRODW® statistical software (version 2007/2010) ("New Efficient Methodology for Research using Optimal Design") developed by LPRAI (Marseille, France). This software facilitated the construction of experimental design matrices and the analysis of response variables. The peak areas from chromatographic analysis of each PAH were used as the response function to evaluate extraction efficiency. All experimental procedures were conducted in compliance with laboratory safety protocols and adhered to principles of good scientific practice and research integrity.

RESULTS AND DISCUSSION

Characterization of CNCs/Fe_2O_3 nanocomposites

Figure 3 shows the FTIR spectra of CNCs, Fe_2O_3, and the CNCs/Fe_2O_3 nanocomposites. The CNCs spectrum exhibits a broad absorption band centered around 3420 cm^{-1}, which is attributed to the O-H stretching vibrations of hydroxyl groups in cellulose and absorbed water (Maria Claro et al., 2024). A distinct peak at approximately 2900 cm^{-1} corresponds to the C-H stretching vibration. The absorption band observed near 1640 cm^{-1} is also indicative of absorbed water in the sample (Maria Claro et al., 2024). Additionally, the band at 1200 - 1000 cm^{-1} region is associated with C-O stretching vibrations, characteristic of the cellulose backbone. In the Fe_2O_3 spectrum, a broad band around 3400 cm^{-1} is attributed to O-H stretching vibrations, while a small peak at 1640 cm^{-1} confirms the presence of absorbed water. A prominent absorption band at around 630 cm^{-1} is assigned to the Fe-O stretching vibration, in agreement with previously reported results (Farahmandjou and Soflaee, 2015). The CNCs/Fe_2O_3 nanocomposite spectrum displays key absorption features: a band at 1640 cm^{-1} consistent with absorbed water, a peak around 1390 cm^{-1} corresponding to C–H bending vibrations, and a band near 607 cm^{-1} attributed to Fe–O bond stretching. The overall spectral profile of the nanocomposite closely resembles that of the CNCs spectrum, which can be explained by the high proportion of CNCs in the composite (3/1 w/w).

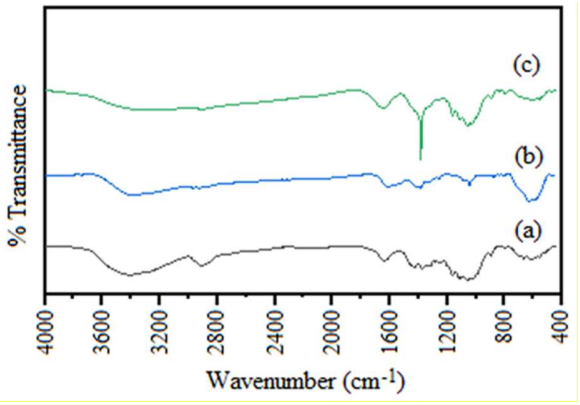

Figure 3. FTIR spectra of (**a**) CNCs, (**b**) Fe_2O_3 and (**c**) CNCs/Fe_2O_3 nanocomposite.

Figure 4 exhibits the SEM micrographs and the corresponding EDX analysis of CNCs, Fe_2O_3 and the CNCs/Fe_2O_3 (3/1) nanocomposite. The Fe_2O_3 nanoparticles appear as irregularly shaped agglomerates (**Figure 4a**) (Costa dos Reis et al., 2017). EDX analysis confirms the presence of iron (58.23 %) and oxygen (36.01 %), consistent with iron oxide composition. The SEM image of the CNCs (**Figure 4b**) reveals sheets-like structures, which contribute to a high surface area, advantageous for extraction purpose. The corresponding EDX spectrum (**Figure 4e**) indicates a high carbon content (63.44 %), followed by oxygen (33.55 %). A small amount of iron detected in the CNCs sample is likely due to contamination of CNCs during the enzymatic hydrolysis of eucalyptus Kraft pulp.

Figure 4c shows SEM image of the CNCs/Fe_2O_3 (3/1) nanocomposite. The image indicates that the smaller Fe_2O_3 nanoparticles are anchored as discrete clusters on the surface of the CNCs sheets. This morphology is attributed to electrostatic self-assembly (Han et al., 2012; Costa dos Reis, 2017), driven by the interaction between the positively charged Fe_2O_3 surface and the negatively charged CNCs in aqueous solution. As expected, the quantity of Fe_2O_3 in the particle is virtually lower than that of CNCs, reflecting the 3/1 (w/w) composition. The EDX spectrum of the nanocomposite (**Figure 2f**) shows a predominant carbon signal (27.41 %) from the nanocellulose matrix, along with oxygen (22.92 %) from both CNCs and Fe_2O_3 , and iron (12.08 %), confirming the successful incorporation of Fe_2O_3 into the nanocomposite.

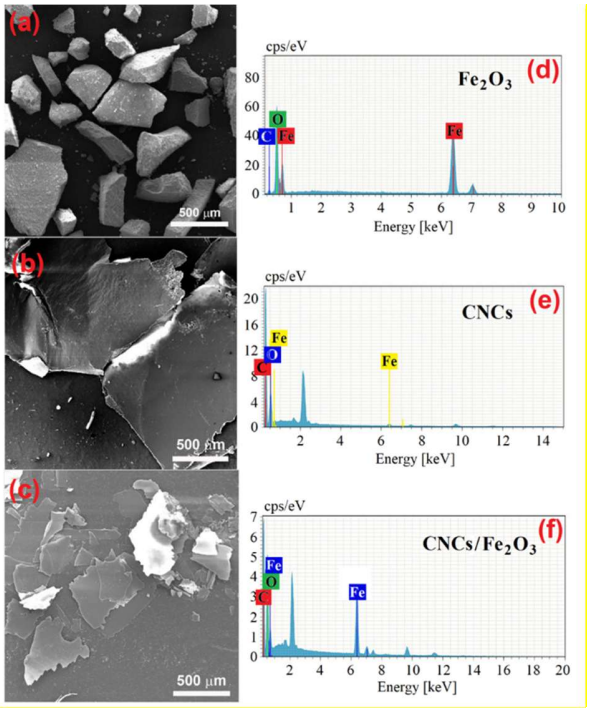

Figure 4. SEM images and EDX spectra of (**a,d**) Fe_2O_3 (**b,e**) CNCs and (**c,f**) CNCs/Fe_2O_3 nanocomposite.

Figure 5 illustrates the particle distribution of Fe_2O_3, CNCs and CNCs/Fe_2O_3 (3/1) nanocomposite. According to the results, Fe_2O_3 nanoparticles presented the average size of 0.46 µm, CNCs nanoparticles and CNCs/Fe_2O_3 (3/1) nanocomposite particles presented the average size of 0.49 µm and 0.89 µm, respectively. These results suggest that Fe_2O_3 nanoparticles were anchored as clusters onto the surface of the CNCs nanoparticles. The particle size of the CNCs/Fe_2O_3 (3/1) nanocomposite reduced drastically (0.89 µm) in comparison to Fe_2O_3 and CNCs. The decrease in size could be attributed to the breakage of CNCs particles during the formation of the nanocomposite carried out under vigorous stirring of the mixture of Fe_2O_3 and CNCs solutions.

Evaluation of the nanocomposite's ability to adsorb PAH

Preliminary investigations into the adsorption performance of the CNCs/Fe_2O_3 nanocomposite were conducted by varying the CNCs/Fe_2O_3 mass ratio. The adsorption efficiency was assessed based on the area of the chromatographic peak, since it is proportional to the concentrations of the analyte. The preconcentration factor (PF) was calculated as the ratio *Ae/Ao*, where *Ao* and *Ae* represent the chromatographic area of the PAH in the standard solution and in the eluate after the extraction, respectively. Experiments were initially carried out with nanocomposite synthesized at pH 2. Using the CNCs/Fe_2O_3 (1/1) nanocomposite, the PF values obtained for naphthalene, fluorene and pyrene were 0.1, 0.1 and 0.2, respectively. These results suggest that pyrene exhibited the highest affinity for the adsorbent material.

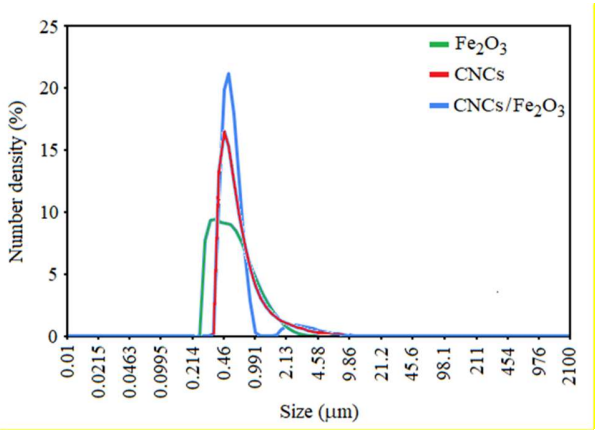

Figure 5. Particle size distribution of Fe_2O_3, CNCs and CNCs/Fe_2O_3 (3/1) nanocomposite.

When the CNCs/Fe_2O_3 mass ratio was increased to 3/1, the PF values improved significantly, reaching 0.5 for naphthalene, 0.87 for fluorene, and 1.64 for pyrene. This indicates that the adsorption efficiency is enhanced by increasing the proportion of CNCs in the composite, because of their high surface area and the electron delocalization (Arantes et al., 2020). These findings support the hypothesis that CNCs serve as the primary adsorptive component in the nanocomposite. Higher CNCs contents were not tested, as an adequate proportion of Fe_2O_3 is necessary to ensure magnetic responsiveness. A significant imbalance between the mass of the adsorbent and the magnetic phase could impair the efficiency of the magnetic solid-phase extraction (MSPE) process.

Based on the improved performance of the CNCs/Fe_2O_3 (3/1) nanocomposite prepared at pH 2, additional batches of this nanocomposite were synthesized at pH 7 and pH 10 to evaluate the influence of the pH during the synthesis on adsorption capacity. **Figure 6** shows the average chromatographic peak areas for naphthalene,

fluorene and pyrene extracted using composites prepared at different pH values.

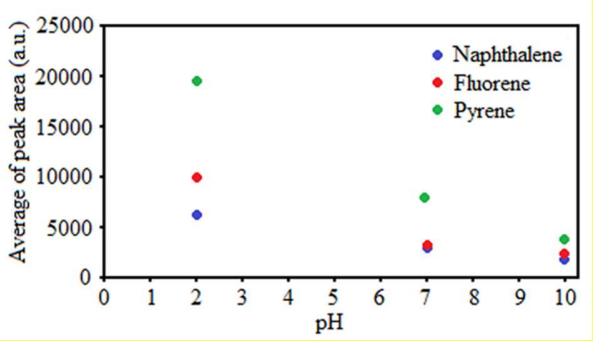

Figure 6. Average chromatographic area for naphthalene, fluorene and pyrene obtained in MSPE´s using nanocomposites synthesized with different pH´s. Synthesis conditions: CNCs/Fe_2O_3 ratio (*w/w*) 3/1 and 1 h of magnetic stirring. Extraction conditions: nanocomposite = 20 mg; standard solution = 20 mL; extraction time = 10 min; eluent = 1 mL; desorption time = 5 min; pH = 5; without NaCl addition.

The highest adsorption capacity was observed with the nanocomposite synthesized at pH 2. This result can be attributed to the electrostatic self-assembly process that occurs between the negatively charged CNCs and the positively charged Fe_2O_3 nanoparticles (Costa dos Reis et al., 2017). At a neutral pH (7), the concentration of H^+ ions is insufficient to fully protonate the Fe_2O_3 particles, reducing the extent of positive charge. Consequently, the electrostatic attraction between Fe_2O_3 and CNCs is weakened, resulting in and inadequately formed composite with fewer magnetic nanoparticles, which negatively affect its adsorption capacity.

In MSPE, nanocomposites with a low proportion of the magnetic phase can present challenges in the separation step. To further optimize the synthesis conditions, nanocomposites with CNCs/Fe_2O_3 mass ratio of 3/1 were prepared at pH 2 with different stirring durations - 1 h and 3 h. These composites were then evaluated for their performance in the preconcentration of naphthalene, fluorene and pyrene. The highest chromatographic peak areas were achieved using the nanocomposite synthesized with 1 h of magnetic stirring.

In conclusion, the optimal synthesis conditions for the CNCs/Fe_2O_3 nanocomposite synthesis were determined to be: CNCs/Fe_2O_3 mass ratio of 3/1, pH 2 and 1 h of magnetic stirring.

Optimization of the MSPE procedure

The optimization study employed a Plackett-Burman design, a two-level fractional factorial design suitable for evaluating up to K = N − 1 variables in N experimental runs, where N is a multiple of 4. This design assumes that interactions between factors are negligible, allowing the main effects to be estimated with a reduced number of experiments (Draper, 1985). In this study, an experimental matrix was constructed to evaluate eight factors, as shown in Table **2**.

Based on the selected experimental design, twelve independent trials were conducted in a random order. The resulting data were analyzed using analysis of variance (ANOVA), and the influence of each factor on the response variables was illustrated using Pareto charts for each PAH, as shown in **Figure 7**. In these charts, the length of each bar represents the magnitude of the factor's effect. Factors with bar extending beyond the reference vertical line are considered statistically significant at a 95 % confidence level.

Additionally, the sign of each event (negative or positive) indicates whether the response decreases or increases, respectively, when the factor changes from its low to high level.

Table 2. Factors and levels of Plackett-Burman design.

Factor	Low level (-1)	High level (+1)
Amount of nanocomposite (mg)	20	40
Vortex extraction time (min)	5	10
Type of eluent	acetonitrile/dichloromethane	hexane
Volume of eluent (mL)	0.5	1
Desorption time in ultrasound (min)	2.5	5
Sample pH	5	12
Volume of sample (mL)	10	20
Ionic strength (% of NaCl)	0	15

In the Pareto charts for all three analytes studied, naphthalene, fluorene, and pyrene, the graphic values for each factor did not exceed the reference line, indicating that none of the evaluated factors were statistically significant for the magnetic solid phase extraction (MSPE) process at the 95 % confidence level. Despite this, the direction of each factor's effect (positive or negative) was used to guide the selection of optimal conditions.

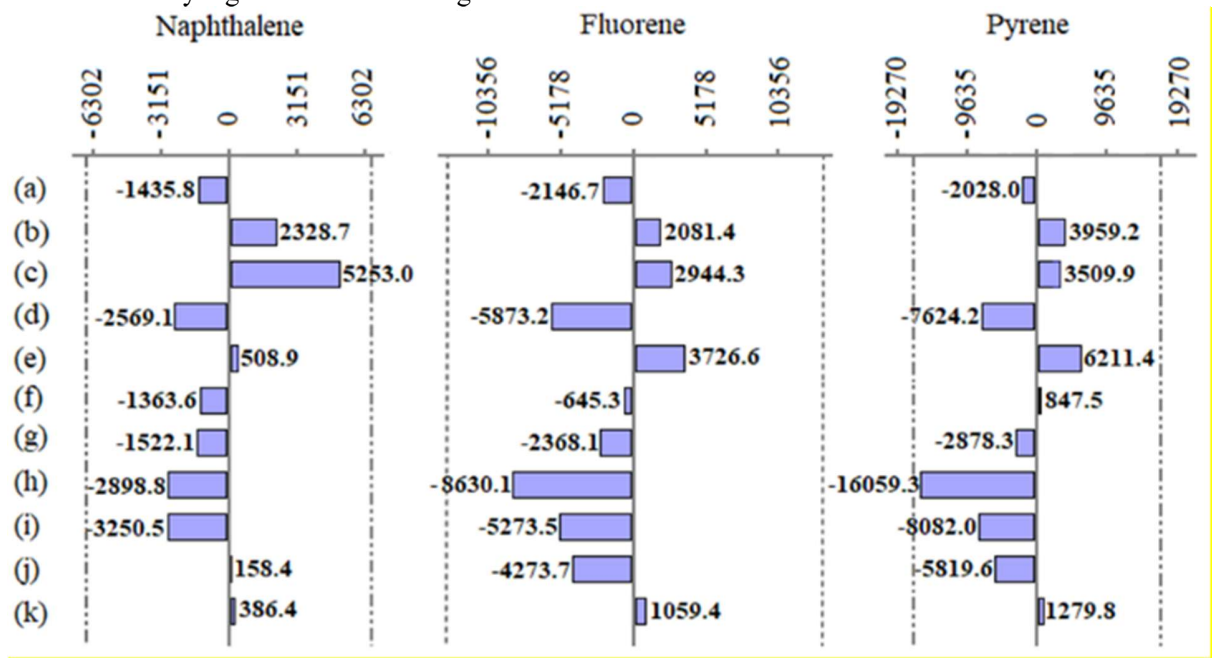

Figure 7. Pareto chart of the Plackett-Burman design for naphthalene, fluorene and pyrene: (**a**) amount of nanocomposite; (**b**) vortex extraction time; (**c**) type of eluent; (**d**) volume of eluent; (**e**) desorption time in ultrasound; (**f**) sample pH; (**g**) volume sample; (**h**) ionic strength; (**i**) ghost 1; (**j**) ghost 2; and (**k**) ghost 3.

For all three PAHs, the following factors showed negative effect on the response: amount of nanocomposite (20 mg), eluent volume (0.5 mL), sample volume (10 mL), and ionic strength (0 % NaCl). Conversely, the following factors had a positive influence: vortex extraction time (10 min), eluent type hexane), and desorption time in an ultrasound (5 min). Sample pH showed a negative effect for naphthalene and fluorene, but a slight positive effect for pyrene. However, due to the minimal impact observed for pyrene, the sample pH was fixed at its lowest tested value (pH 5).

According to the Plackett-Burman experimental design (Draper, 1985), the optimal MSPE conditions for the extraction of naphthalene, fluorene and pyrene were established as follows: 20 mg of CNCs/Fe_2O_3 (3/1) nanocomposite, vortex extraction for 10 min, hexane as the eluent, 0.5 mL of eluent volume, 5 min of ultrasonic desorption time, sample pH of 5, 10 mL of sample volume and no added NaCl.

MSPE under optimal conditions

Three replicate MSPE procedures were performed under the optimal conditions, and the preconcentration factors (PFs) were calculated for each PAH. The PF values were 2 for naphthalene, 4 for fluorene, and 7 for pyrene. These results indicate that the CNCs/Fe_2O_3 (3/1) nanocomposite synthesized under optimal conditions exhibits a greater adsorption - desorption efficiency for pyrene. However, the relatively low PF observed for naphthalene suggests that the current MSPE protocol is suboptimal for its preconcentration. A separate optimization study would be necessary to enhance the extraction efficiency for naphthalene specifically.

CONCLUSION

Based on the findings of this study, the following conclusions can be drawn:

A scalable and efficient method for preparing CNCs/Fe_2O_3 hybrid particles was described, which

relies on the electrostatic attraction between both components.

Magnetic solid-phase extraction (MSPE) was used, to isolate the PAHs from the aqueous phase. Among the composites used, the CNCs/Fe_2O_3 (3/1) exhibited the highest adsorption efficiency. This result suggests that CNCs serves as the primary adsorptive component, while Fe_2O_3 contributes to magnetic separation.

The best extraction performance was observed at pH 2, with the adsorption efficiency following the order: pyrene > fluorene > naphthalene.

To further optimize the extraction process, a Plackett–Burman experimental design was applied to investigate the effects of several variables. The optimal MSPE conditions determined through this design included: 20 mg of CNCs/Fe_2O_3 nanocomposite, 10 minutes of vortex extraction, hexane as the eluent (0.5 mL), 5 minutes of ultrasonic desorption, a sample pH of 5, and a total sample volume of 10 mL.

In conclusion, the CNCs/Fe_2O_3 (3:1) nanocomposite offers a fast, simple, and environmentally sustainable option as an adsorbent in MSPE procedures for the preconcentration of PAHs. It is scalable and eco-friendly synthesis, ease of handling, and effective preconcentration—especially for fluorene and pyrene—underscore its potential in environmental applications, particularly for water quality monitoring and pollutant remediation.

The adsorption-desorption performance demonstrated here may be extended to other PAHs commonly found in produced water.

Availability of Data and Materials

The sets of data generated during and/or analysed during the research work can be available from the corresponding author on logical request.

Funding

The research received grant from: Programa de Recursos Humanos da Agência Nacional do Petróleo, Gás Natural e Biocombustíveis – PRH16.1- ANP; CNPq (305.565/2022-2) and FAPERJ (E-26/204.066/2024).

Author Contributions

Luciana Costa conceived, designed and performed the experiments. Isabella Dias and Valdeir Arantes provided the CNCs (BR 10 2020 025815 0 A2) and provided scientific support on the characteristics and properties of CNCs. Isabella Dias performed particle size and FTIR analyses. Luciana Costa and Bluma Soares performed SEM/EDX analysis. Elizabete Lucas and Bluma Soares analyzed the data. Luciana Costa, Elizabete Lucas and Bluma Soares wrote the paper.

Conflicts of Interest

The authors declare no conflict of interest.

Declarations

No experimental procedure requiring ethical concern was established during this research work. Thus, ethical approval is not required.

Acknowledgments

The authors thank the financial support from "Programa de Recursos Humanos da Agência Nacional do Petróleo, Gás Natural e Biocombustíveis – PRH16.1- ANP". Elizabete Lucas thank the Brazilian Agencies: CAPES, CNPq (305.565/2022-2) and FAPERJ (E-26/204.066/2024). Bárbara Pereira, technician of the "Laboratory of Applied Bionanotechnology of the Department of Biotechnology in the Engineering School of Lorena" (Lorena, São Paulo, Brasil).

REFERENCES

Amakiri KT, Ogolo NA, -Dimakis AA, Albert O. Produced water treatment by semi-continuous sequential bioreactor and microalgae photobioreactor. Bioresources and Bioprocessing. 2024 Jun 8:87-95. DOI: https://doi.org/10.1186/s40643-024-00775-3

Amakiri KT, Canon AR, Molinari M, Angelis-Dimakis A. Review of oilfield produced water treatment technologies. Chemosphere. 2022 Jul 298:1-20. DOI: https://doi.org/10.1016/j.chemosphere.2022.134064

Abujaber F, Jiménez-Moreno M, Bernardo FJG, Martín-Doimeadios RCR. Simultaneous extraction and preconcentration of monomethylmercury and inorganic mercury using magnetic cellulose nanoparticles. Microchimica Acta. 2019 Jun 186:400. DOI: https://doi.org/10.1007/s00604-019-3492-8

Aoudi B, Boluk Y, Gamal El-Din M. Recent advances and future perspective on nanocellulose-based materials in diverse water treatment applications. Science of the Total Environment. 2022 Oct 843:156903. DOI: https://doi.org/10.1016/j.scitotenv.2022.156903

Arantes V, Dias IKR, Berto GL, Pereira B, Marotti BS, Nogueira CFO. The current status of the enzyme-mediated isolation and functionalization of nanocelluloses: production, properties, techno-economics, and opportunities. Cellulose. 2020 Jul 27:10571-10630. (a). DOI: https://doi.org/10.1007/s10570-020-03332-1

Arantes V, Dias IKR, Santos JC, Hilares RT. Processo de Preparação de Soluções Estáveis de Nanocristais de Celulose por Meio de Pós-tratamento por Cavitação Hidrodinâmica. Holder: Universidade de São Paulo. BR 10 2020 025815 0 A2. Deposit: Dec 17, (2020). Concession: Jun 28, 2022. Int. Ci. D21C 9/00 (2006.01), D21C 3/00 (2006.01). (b).

Bhatnagar A, Sillanpaa M, Witek-Krowiak A. Agricultural waste peels as versatile biomass for water purification – A review. Chemical Engineering Journal. Jun 2015 270:244-271. DOI: https://doi.org/10.1016/j.cej.2015.01.135

Binet MT, Stauber JL, Winton T. The Effect of Storage Conditions on Produced Water Chemistry and Toxicity. In Lee, K., Neff, J. (eds) Produced Water 2011. Springer, New York. DOI: https://doi.org/10.1007/978-1-4614-0046-2_7

CONAMA RESOLUTION 393, August 8, 2007; "Establishes provisions for the continuous release of processed water or water produced on oil and natural gas sea platforms and makes other provisions; Published in Official Gazette 153 on August 9, Section 1, pages 72-73.

Costa dos Reis L, Vidal L, Canals A. Graphene oxide/Fe_3O_4 as sorbent for magnetic solid-phase extraction coupled with liquid chromatography to determine 2,4,6-trinitrotoluene in water samples. Analytical and Bioanalytical Chemistry. 2017 Feb 409:2665-2674. DOI: https://doi.org/10.1007/s00216-017-0211-3

Delgado B, Pino V, Ayala JH, González V, Afonso AM. Nonionic surfactant mixtures: a new cloud-point extraction approach for the determination of PAHs in seawater using HPLC with fluorimetric detection. Analytica Chimica Acta. 2004 Aug 518:165-172. DOI: https://doi.org/10.1016/j.aca.2004.05.005

Draper NR. Plackett and Burman designs. In: Kotz S, Johnson L, editors. Encyclopedia of Statistical Sciences 1985. New York: John Wiley & Sons.

Dufresne A. Nanocellulose: a new ageless bionanomaterial. Materials Today. 2013 Jun 16:220-227. DOI: https://doi.org/10.1016/j.mattod.2013.06.004

EPA "Industrial Wastewater Treatment Technology". United States Environmental Protection Agency. 2019 [12/05/2025] Available from: Final Report: Oil and Gas Extraction Wastewater Management | US EPA

EPA, "IRIS Assessment". United States Environmental Protection Agency. 1990 [12/05/2015] Available from: Fluorene CASRN 86-73-7 | IRIS | US EPA, ORD (12/05/2025) (a).

EPA, "IRIS Assessment". United States Environmental Protection Agency. 1990 [12/05/2025] Available from: Pyrene (CASRN 129-00-0) | IRIS | US EPA (b).

Farahmandjou M, Soflaee F. Synthesis and characterization of α-Fe_2O_3 nanoparticles by simple co-precipitation method. Physical Chemistry Research. 2015 Sep 3:191-196. DOI: https://doi.org/10.22036/pcr.2015.9193

Fernández E, Vidal L, Canals A. Zeolite/iron oxide composite as sorbent for magnetic solid-phase extraction of benzene, toluene, ethylbenzene and xylenes from water samples prior to gas chromatography/mass spectrometry. Journal of Chromatography A. 2016 Aug 1458:18-24. DOI: https://doi.org/10.1016/j.chroma.2016.06.049

Gabardo IT, Meniconi MFG, Falcão LV, Vital NAA, Pereira RCL, Carreira RS. Hydrocarbon and Ecotoxicity in seawater and sediment samples of Guanabara Bay after the oil spill. International Oil Spill Conference Proceedings 2001. 2:941-950. DOI: https://doi.org/10.7901/2169-3358-2001-2-941

Gabardo IT, Platte EB, Araujo AS, Pulgatti FH, Evaluation of Produced Water from Brazilian Offshore Platforms. In: Lee, K., Neff, J. (eds) Produced Water 2011. Springer, New York. DOI: https://doi.org/10.1007/978-1-4614-0046-2_3

Gratz LD, Bagley ST, Leddy DG, Johnson JH, Chiu C, Stommel P. Interlaboratory Comparison of HPLC-Fluorescence Detection and GC/MS: Analysis of PAH Compounds Present in Diesel Exhaust. Journal of Hazardous Materials. 2000 May 74:37-46. DOI: https://doi.org/10.1016/s0304-3894(99)00197-1

Habibi Y. Key advances in the chemical modification of nanocelluloses. Chemical Society Reviews. 2014 43:1519-1542. DOI: https://doi.org/10.1039/C3CS60204D

Han Q, Wang Z, Xia J, Chen S, Zhang X, Ding M. Facile and tunable fabrication of Fe_3O_4/graphene oxide nanocomposites and their application in the magnetic solid-phase extraction of polycyclic aromatic hydrocarbons from environmental water samples. Talanta. 2012 Nov 101:388–395. DOI: https://doi.org/10.1016/j.talanta.2012.09.046

IARC, International Agency for Research on Cancer 1985 [12/05/2025] Available from: http://monographs.iarc.fr/ENG/Monographs/vol1-42/mono35.pdf.

IARC, International Agency for Research on Cancer 2012 [12/05/2025] Available from: http://monographs.iarc.fr/ENG/Monographs/vol100F/mono100F.pdf.

Kong H, He J, Gao Y, Han J, Zhu X. Removal of Polycyclic Aromatic Hydrocarbons from Aqueous Solution on Soybean Stalk–based Carbon. Journal of Environmental Quality. 2011 Nov. 40:1737-1744. DOI: https://doi.org/10.2134/jeq2010.0343

Manousi N, Deliyanni EA, Rosenberg E, Zachariadis GA. Ultrasound-assisted magnetic solid-phase extraction of polycyclic aromatic hydrocarbons and nitrated polycyclic aromatic hydrocarbons from water samples with a magnetic polyaniline modified graphene oxide nanocomposite. Journal of Chromatography A. 2021 May 1645: 462104. DOI: https://doi.org/10.1016/j.chroma.2021.462104

Maria Claro A., Dias IKR, Fontes ML, Colturato VMM, Lima LR, Sávio LB, Berto GL, Arantes V, Barud HS. Bacterial cellulose nanocrystals obtained through enzymatic and acidic routes: A comparative study of their main properties and in vitro biological responses. Carbohydrate Research. 2024 Apr 539: 109104. DOI: https://doi.org/10.1016/j.carres.2024.109104

Mautner A. Nanocellulose water treatment membranes and filters: a review. Polymer International. 2020 Feb 69:741-751. DOI: https://doi.org/10.1002/pi.5993

Pampanin DM, Sydnes MO. Polycyclic aromatic hydrocarbons a constituent of petroleum: presence and influence in the aquatic environment. In Hydrocarbon 2013. InTech, Rijeka, Croatia. DOI: https://doi.org/10.5772/48176

PETROBRAS "Relatório Anual de Monitoramento da Água Produzida Descartada em Plataformas" 2021 [12/05/2025]. Available from: Relatórios Anuais: transparência é fundamental | Petrobras

PETROBRAS 2022 [12/05/2025]. Available from: Monitoramento de Água Produzida | Comunicação Bacia de Santos (petrobras.com.br)

Ruiz-Palomero C, Soriano ML, Valcárcel M. Nanocellulose as analyte and analytical tool: Opportunities and challenges. TrAC-Trends in Analytical Chemistry. 2017 Feb 87:1-18. DOI: https://doi.org/10.1016/j.trac.2016.11.007

Šafaříková M, Šafařík I. Magnetic solid-phase extraction. Journal of Magnetism and Magnetic Materials. 1999 Ap 194:108-112. DOI: https://doi.org/10.1016/S0304-8853(98)00566-6

Sasaki T, Tanaka S. Adsorption behavior of some aromatic compounds on hydrophobic magnetite for magnetic separation. Journal of Hazardous Materials. 2011 Nov 196:327-334. DOI: https://doi.org/10.1016/j.jhazmat.2011.09.033

Soares APS, Marques MFV, Mothé MG. Green Composite Sorbents from Coffee Capsule Waste and Eucalyptus urograndis Holocellulose. Arabian Journal for Science and Engineering. 2024 Mar 14:4539-4553. DOI: https://doi.org/10.1007/s13369-025-10030-2

Song X, Li J, Xu S, Ying R, Ma J, Liao C, Liu D, Yu J, Chen L. Determination of 16 polycyclic aromatic hydrocarbons in seawater using molecularly imprinted solid-phase extraction coupled with gas chromatography-mass spectrometry. Talanta. 2012 sep 99:75-8. DOI: https://doi.org/10.1016/j.talanta.2012.04.065

Sultanova NG, Kasarova SN, Nikolov ID. Characterization of optical properties of optical polymers. Optical and Quantum Electronics. 2013 Sep 45:221-232. DOI: https://doi.org/10.1007/s11082-012-9616-6

Venkatesan A, Wankat PC. Produced water desalination: An exploratory study. Desalination. 2017 Feb 404:328-340. DOI: https://doi.org/10.1016/j.desal.2016.11.013

WHO – World Health Organization "Water, Sanitation, hygiene and Health" 2019 [12/05/2025]. Available from: https://www.who.int/publications/i/item/9789240013391

Yang X, Yin Y, Zong Y, Wan T, Liao X. Magnetic nanocomposite as sorbent for magnetic solid phase extraction coupled with high performance liquid

chromatography for determination of polycyclic aromatic hydrocarbons. Microchemical Journal. 2019 Mar 145:26-34. DOI: https://doi.org/10.1016/j.microc.2018.10.013
Yang J, Zhang X, Wang X, Wang H, Zhao J, Zhou Z, Du X, Lu X. In situ anchor of multi-walled carbon nanotubes into iron-based metal-organic frameworks for enhanced adsorption of polycyclic aromatic hydrocarbons by magnetic solid-phase extraction. Journal of Chromatography A. 2022 Oct 1681:463459. DOI: https://doi.org/10.1016/j.chroma.2022.463459
Yaping L, Qi L, Shen Y, Ma H. Facile preparation of surface-exchangeable core@shell iron oxide@gold nanoparticles for magnetic solid-phase extraction: Use of gold shell as the intermediate platform for versatile adsorbents with varying self-assembled monolayers. Analytica Chimica Acta. 2014 Feb 811:36-42. DOI: https://doi.org/10.1016/j.aca.2013.12.020
Zhang S, Du Z, Li G. Layer-by-Layer Fabrication of Chemical-Bonded Graphene Coating for Solid-Phase Microextraction. Analytical Chemistry. 2011 Aug. 83:7531-7541. DOI: https://doi.org/10.1021/ac201864f
Zhang A, Zhao S, Wang L, Yang X, Zhao Q, Fan J, Yuan X. Polycyclic aromatic hydrocarbons (PAHs) in seawater and sediments from the northern Liaodong Bay, China. Marine Pollution Bulletin. 2016 Dec 113:592-599. DOI: https://doi.org/10.1016/j.marpolbul.2016.09.005

Nanomaterials and Polymers Innovations Vol. 1, No.1 (2025); 32-39
ISSN: 3102-0798 (Online). Available online at www.nepalpolymer.org
DOI:https://doi.org/……xyy……xyz (to be updated)

Original research article

Dip-Coated Cobalt Oxide Thin Film: A Facile Approach for Oxygen Evolution Reaction

Sharmila Pradhan[1], Mani Ram Kandel[1*], Leela Pradhan Joshi[2], Dinesh Kumar Chaudhary[2], Sheikh Manjura Hoque[3], Chhabi Lal Gnawali [4], Shankar Prasad Shrestha [5*]

[1] Department of Chemistry, Amrit Campus, Tribhuvan University, Kathmandu 44600, Nepal
[2] Department of Physics, Amrit Campus, Tribhuvan University, Kathmandu 44600, Nepal
[3] Material Science Division, Atomic Energy Centre, Dhaka, Bangladesh
[4] Institute of Engineering, Pulchowk Campus, Tribhuvan University, Lalitpur 44700, Nepal
[5] Department of Physics, Patan Multiple Campus, Tribhuvan University, Lalitpur 44700, Nepal

Abstract: This study presents a low-cost and scalable dip-coating approach for synthesizing nanoparticles of cobalt oxide (Co_3O_4) thin films on stainless-steel substrate and assesses electrochemical performances in alkaline water electrolysis (AWE). Electrochemical assessment via linear sweep voltammetry (LSV) exhibited that the 10L Co_3O_4-coated steel exhibited reduced overpotentials of 258, 350, and 430 mV at current densities of 10, 50, and 100 $mAcm^{-2}$, respectively, compared to uncoated steel, highlighting the influence of film thickness on OER performance. The OER activities of the as-synthesized electrocatalyst are due to the intrinsic electronic structure, promising oxidation states of Co, and catalytic properties. This study brings a cost-effective and controllable synthesis approach for cobalt oxide thin films, presenting insights into the influence of layer deposition on electrocatalytic activity.

Keywords: dip-coating, nanoparticles, linear sweep voltammetry, oxygen evolution reaction, thin film

शोधसार: यो अध्ययनले स्टेनलेस स्टिल सब्सट्रेटमा कोबाल्ट अक्साइड (Co_3O_4) न्यानोपार्टिकलहरू समाविष्ट थिन फिल्महरू तयार गर्नका लागि कम लागतमा र ठूलो परिमाणमा उपयोग गर्न मिल्ने डिप-कोटिङ प्रविधि प्रस्तुत गर्दछ । साथै यसले उक्त सामग्रीको क्षारीय जल इलेक्ट्रोलाइसिस (AWE) मा इलेक्ट्रोरासायनिक कार्यसम्पादनको मूल्याङ्कन पनि गर्दछ। लिनियर स्वीप भोल्टामेट्री (LSV) मार्फत गरिएको परीक्षणमा १० लिटर कोबाल्ट अक्साइड-लेपित स्टिलले १०, ५०, र १०० मिलिएम्पेएर प्रति वर्ग सेन्टिमिटर धारा घनत्वमा क्रमशः २५८, ३५०, र ४३० मिलिभोल्टको घटाइएको ओभरपोटेन्सियल देखाएको छ, जुन लेप नगरिएको स्टिलको तुलनामा उल्लेखनीय सुधार हो। यसले थिन फिल्मको मोटाइले अक्सिजन इभोलुसन रिएक्सन (OER) कार्यसम्पादनमा महत्वपूर्ण प्रभाव पार्ने कुरा स्पष्ट गर्छ। तयार गरिएको इलेक्ट्रोक्याटालिस्टको OER सक्रियता यसको अन्तर्निहित इलेक्ट्रोनिक संरचना, कोबाल्टको अनुकूल अक्सिडेशन अवस्थाहरू, र उत्कृष्ट उत्प्रेरक गुणहरूका कारण देखिन्छ । समग्रमा, यो अध्ययनले कोबाल्ट अक्साइड थिन फिल्महरू निर्माणका लागि लागत-प्रभावकारी र नियन्त्रणयोग्य संश्लेषण विधि प्रस्तुत गर्दछ । साथै यसले तह-लेपनको इलेक्ट्रोक्याटालिटिक कार्यसम्पादनमा पार्ने प्रभावसम्बन्धी उपयोगी जानकारी पनि प्रदान गर्दछ।

INTRODUCTION

Fossil fuel combustion is a major contributor to air pollution, posing severe environmental challenges [1–3]. As global energy demands continue to rise, transitioning to sustainable energy sources is essential to mitigate ecological damage [4,5]. Renewable alternatives such as solar, wind, and hydrogen energy offer practical solutions, as they produce power with minimal environmental impact [6]. Among these, oxygen and hydrogen are particularly promising energy carriers, capable of meeting the world's growing energy needs. Their production is primarily driven by water-splitting reactions, namely the oxygen evolution reaction (OER) and hydrogen evolution reaction (HER), which are electrochemical processes facilitated by electrocatalysis at the electrode-electrolyte interface [7,8]. However, achieving long-term stability under operational conditions remains a significant challenge, as only a few electrocatalytic materials

* Corresponding authors, E-mail: mrk.shringa4@gmail.com (MRK), shankarpds@yahoo.com (SPS)
© Nepal Polymer Institute, Kathmandu, Nepal
Received: April 23, 2025; Revised: May 11, 2025; Accepted: May 12, 2025; Published: May 19, 2025

demonstrate the necessary durability [9]. To improve reaction efficiency, both cathodic and anodic processes typically require catalysis, with noble metals (Pt, Ru, and Ir) and their oxides (PtO_2, IrO_2, and RuO_2) being the most used electrodes [10–12]. Nevertheless, the scarcity and high cost of noble metal-based materials demand the exploration of alternative, efficient, and eco-friendly electrocatalysts based on transition metals [13,14]. Exploring such alternatives opens new avenues for developing cost-effective, high-performance catalysts, which are crucial for advancing hydrogen-based energy systems [4,15,16].

Transition metal oxides (TMO) are promising electrocatalysts due to their excellent mechanical and chemical stability, as well as their high charge transfer capacity, even in amorphous states, highlighting their versatility. Their electronic structure can also be finely tuned, making them ideal candidates for water splitting applications [10,17]. For example, NiO/NF exhibits an overpotential of 310 mV at 10 mA cm^{-2}, while $NiCo_2O_4$ synthesized via the hydrothermal method shows an overpotential of 390 mV under the same conditions [18]. Another study found that mesoporous $NiCo_2O_4$ achieved a lower overpotential of 350 mV at 10 mA cm^{-2} [19]. However, challenges such as stability issues and relatively high overpotentials of transition metal-based monometallic oxides during OER must be addressed through various synthetic strategies [10]. The synthesis methods for metal oxides play a crucial role in determining their morphology and particle size. Various techniques, including the sol-gel method, chemical vapor deposition (CVD), co-precipitation, electrodeposition, and hydrothermal synthesis, have been employed [20]. However, these methods have limitations such as temperature control issues in sol-gel processes, impurity incorporation and low crystallinity in co-precipitation, and hydrolysis-related contamination in hydrothermal synthesis [20,21].

Thin-film deposition offers an alternative and effective approach for synthesizing OER transition metal oxide electrocatalysts, as it enables precise control over film thickness, morphology, and composition, all of which significantly impact catalytic performance and stability [22,23]. This technique allows us to produce uniform, defect-free films with adjustable electronic properties [24]. Furthermore, thin films enhance the active surface area, electrical conductivity, and long-term durability, making them ideal for water-splitting applications [25]. Previous literature has shown the synthesis of various transition metal-based electrocatalysts. For instance, $CoFeO_x$ and CoO_x nanowires synthesized exhibited superior overpotential due to their tuned electronic structure and charge transfer capacitance. Similarly, cobalt oxides and their composites exhibit high reactivity and self-repair capabilities. Additionally, their nano-sized hierarchical structures and doping potential enhance their efficiency and cost-effectiveness as electrocatalysts [25]. Several studies have demonstrated enhanced OER performance of transition metal oxide thin films. For instance, the NiO thin films displayed better OER performance, attributed to their good electrocatalytic behavior [26]. Similarly, spray-assembled nanoscale CoO_x exhibited better OER performance due to their high electrochemically active surface area and favorable electrode kinetics [27]. Wu et al. reported mesostructured Co_3O_4 thin film delivered a low OER potential 340 mV@10 mA cm^{-2}, owing to enhanced electrode-electrolyte interface [28]. In another study, CoO_x thin films fabricated by two-step electrolytic method exhibit an overpotential of 362 mV at 10 mA/cm^2 for OER, further highlighting the effectiveness of tailored thin-film architectures in boosting activity [29]. Although the overpotential reported here is slightly higher than that of the reported value, the simplicity of the preparation technique could undoubtedly reduce the cost of the electrode for OER. Further, cobalt oxide is recognized as an effective electrocatalyst for water splitting due to its unique characteristics, including the formation of heterogeneous interfaces, nanoscale structures, and the dynamic oxidation states of Co^{2+} and Co^{3+} during electrochemical reactions [30,31]. Their nanostructured and porous nature increases the available surface area and improves reaction kinetics [17]. However, challenges such as low electrical conductivity and stability must be addressed through structural modifications, surface treatments, or hybridization with conductive materials. These improvements make Co_3O_4 a promising candidate for efficient and durable OER applications. Therefore, this work focuses on the effect of cobalt oxide layers on water electrolysis.

Herein, a thin film of Co_3O_4 was synthesized using the cost-effective dip coating technique, which was

chosen for its low cost, simplicity, and non-hazardous nature. Co_3O_4 nanoparticles are highly effective catalysts for the oxygen evolution reaction (OER) due to their spinel structure, which contains both Co^{2+} and Co^{3+} ions that facilitate electron transfer. During OER, Co^{3+} is converted to Co^{4+}, generating active sites for oxygen formation through a sequence of hydroxide adsorption, oxidation, and molecular oxygen release. Given these characteristics, the as-synthesized electrocatalyst is considered an effective OER electrocatalyst prepared via the dip coating method.

MATERIALS AND METHODS

Chemicals

Cobalt chloride hexahydrate ($CoCl_2.H_2O$, Purity > 99%, Sigma Aldrich) of A. R grade, acetone (99%, Sigma Aldrich), ethanol (99%, Sigma Aldrich), potassium hydroxide (KOH), distilled water was used for the experiment. Stainless steel pieces were brought from the local market.

Precleaning of Stainless-Steel Substrate

Prior to deposition, contaminants such as dirt, grease, and others organic residues were removed from the stainless-steel substrate. Initially, the substrate was immersed in 30 ml acetone and ultrasonicated for 15 minutes to remove organic residues and grease, followed by cleaning with distilled water under sonication for 10 minutes. Next, the cleaned substrate was immersed in 30 ml ethanol and sonicated for 15 minutes to disregard the residual contaminants. After that, the substrate was dried and stored in a dust free chamber at room temperature.

Synthesis of Electrocatalyst Cobalt Oxide (Co_3O_4)

A thin film of cobalt oxide (Co_3O_4) was synthesized using cost-effective dip coating technique. Briefly, 0.1 M cobalt chloride hexahydrate ($CoCl_2.6H_2O$) solution was prepared by dissolving 1.22 g of $CoCl_2.6H_2O$ in distilled water, followed by continuous stirring at 60 °C for 2 hours. Pure stainless-steel substrates (5 × 2.5) cm^2 were employed for thin-film deposition. The dip-coating process was conducted at a withdrawal rate of 50 mm/min, with an immersion time of 1 s and an air-drying period of 1 min. The cycle of dipping, withdrawal, and drying at 100 °C was repeated multiple times to fabricate films with varying thicknesses. Thin films comprising 5, 10, and 15 layers (5L, 10L, and 15L) of Co_3O_4 were synthesized and subsequently subjected to annealing at 300 °C for 2 hours.

Physicochemical Characterization and Electrochemical Characterization

X-ray diffraction (XRD) analysis was achieved using a Rigaku Ultima IV diffractometer (Rigaku Corporation, Japan) with Cu Kα radiation (λ = 1.5406 Å) to investigate the crystal structure, phase composition, and particle size of OER electrocatalysts, supporting the identification of active phase metal oxides [32,33]. Variations in peak positions and broadening provide information on structural distortions and nanoscale characteristics, which are crucial for electrocatalytic efficacy. Likewise, UV-Vis spectroscopy is utilized to explore the optical properties and electronic structure of the as-synthesized electrocatalysts. By examining absorption spectra and employing Tauc plots, the bandgap energy can be determined, offering insights into charge transfer processes and metal oxidation states. This technique is principally convenient in assessing the light absorption potential of photo-assisted OER electrocatalysts and understanding their electronic interactions and catalytic behaviour.

For electrochemical characterization of the OER, a workstation typically includes an electrochemical setup designed to operate experiments and assess electrocatalytic activities. The core component is a potentiostat which regulates the applied potential or current while recording electrochemical responses, enabling methods such as LSV (34). Electrochemical measurements were conducted using a CORRTEST CS310M electrochemical workstation (Wuhan Corrtest Instruments Corp., Ltd., China). The system employs a three-electrode setup, where the working electrode (WE) consists of the catalyst-coated electrode. The counter electrode (CE) is platinum wire, while the reference electrode (RE) is a stable standard like Hg/HgO to ensure precise potential measurements. The electrochemical cell is operated with a suitable 1M KOH electrolyte at room temperature. This setup enables the reliable evaluation of OER electrocatalysts in terms of their efficiency, durability, and reaction kinetics.

RESULTS AND DISCUSSION

Cobalt oxide thin films were successfully synthesized using a dip-coating method, offering a cost-effective and controllable approach to film

deposition (**Scheme 1**). The synthesis involved dissolving cobalt chloride hexahydrate in water to create a uniform precursor solution. During dip coating, the substrate was immersed in the solution, forming a thin layer that underwent gradual hydrolysis and oxidation upon exposure to air. To ensure complete phase transformation, the coated films were annealed at 300°C, promoting the conversion of precursor materials into the spinel Co_3O_4 phase through oxidation. The number of coating cycles (5L, 10L, and 15L) directly influenced the thickness and crystallinity of the films. Based on the controlled dip-coating procedure and consistent solution concentrations, we anticipate that the film thickness increases proportionally with the number of coating layers (i.e., 5L, 10L, and 15L). This relative increase is also supported by the observed trends in electrochemical performance. Thermal treatment further enhanced crystallite formation, improved film adhesion, and eliminated residual solvents. The presence of mixed-valence cobalt ions (Co^{2+}/Co^{3+}) within Co_3O_4 contributes to its electrocatalytic performance, particularly in the OER, by facilitating electron transfer and providing active catalytic sites.

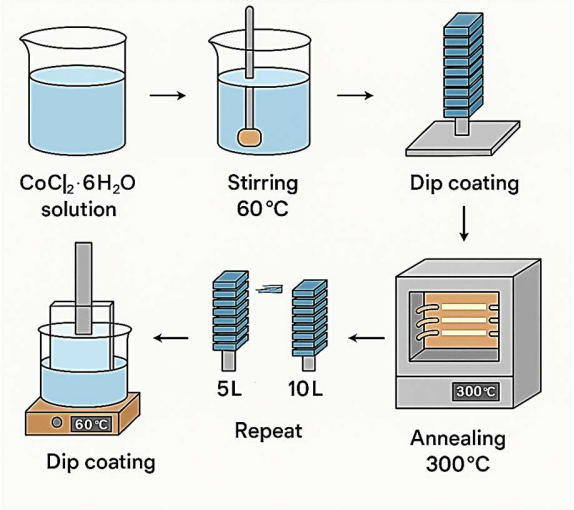

Scheme 1. Schematic diagram of the synthesis of Co_3O_4 electrocatalyst.

Crystallography and Morphological Analysis

The structural properties of cobalt oxide thin films were analysed using the X-ray diffraction technique over a Bragg's angle (2θ) range from 10° to 80°, as displayed in **Figure 1**. The diffraction pattern shows sharp peaks at 43.27° and 74.44°, corresponding to the (400) and (620) crystal planes of Co_3O_4, in agreement with JCPDS file no. 43 – 1003. The XRD results confirm the fruitful formation of the cobalt oxide phase, consistent with earlier reported literature [35,36]. Furthermore, the diffraction pattern reveals the formation of Co_3O_4 thin film with face-centred cubic spinel crystal. An extra peak observed at 50° is attributed to reflection from the steel substrate. The additional peak observed at around 50° is attributed to the underlying stainless-steel substrate, which contributes to the overall diffraction pattern of the coated sample. Since the cobalt oxide thin films were deposited directly on a stainless-steel substrate, certain substrate reflections (especially from Fe or Cr constituents) can appear in the XRD pattern, especially if the film thickness is not sufficient to completely mask substrate contributions.

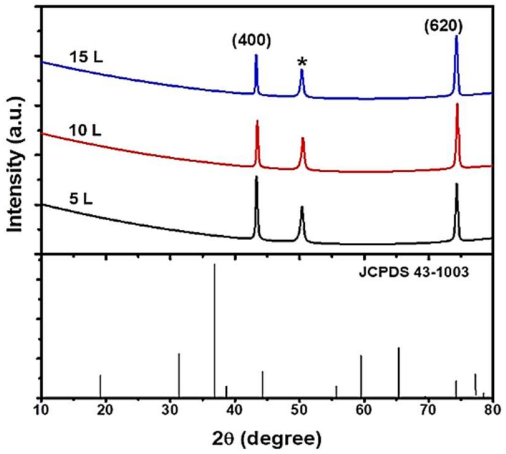

Figure 2. X-ray diffraction pattern of Co_3O_4 electrocatalyst.

Table 1. Structural parameters of thin layers of cobalt oxide Co_3O_4.

Sample (L)	B	Obs d	Rep. d	β	D	Avg. Crys.
	43.36	2.084	2.087	0.285	30.00	
5	74.34	1.28	1.27	0.377	26.48	28.24
10	43.34	2.085	2.02	0.2903	29.46	
	74.44	1.27	1.27	0.4139	24.10	26.78
15	43.30	2.089	2.087	0.2741	31.26	
	74.29	1.27	1.27	0.4493	22.50	26.88

B=Bragg's angle (2θ, degree), obs d=observed d spacing (Å), Rep. d= reported d spacing (Å), β=FWHM (degree), D=Crystallite size(nm), Avg Crys. = Average crystallite size (nm).

The crystallite size of he as fabricated electrode material was determined using Debye Scherrer's equation (37).

$$D = K\lambda/\beta cos\theta \ldots\ldots\ldots\ldots\ldots\ldots\ldots\ldots (1)$$

where K= 0. 9, λ = 0.154 nm, and β = full width at half maximum (FWHM) obtained from Gaussian fitting of the diffraction peak. **Table 1** displays the observed and stated values of d-spacing along with crystallite size. The calculated average crystallite size of 5, 10 and 15L Co_3O_4 thin film is found to be 28.24, 26.78 and 26.88 nm, respectively. The reduction in crystallite size for 10 and 15 L films proposes an augmented active surface area compared to 5L films, which could be improve the electrocatalytic performance.

UV-Vis Spectroscopy

Optical properties of cobalt oxide thin film were explored using transmittance spectra within the wavelength range 420 to 900 nm. Fig. 2(a) shows the variation of the absorbance of Co_3O_4 film with wavelength. The figure depicts two broad absorbance at wavelengths of 440 nm and 760 nm lying in the visible light region, attributing for the two optical transitions. In general, the edge of the absorbance is determined by the Tauc formula, equation (2)(37).

$$(\alpha hv) = A\left(hv - E_g\right)^n \ldots\ldots\ldots\ldots\ldots\ldots\ldots (2)$$

where

α is the absorption coefficient

hυ - the photon energy

E_g - the optical band gap

A – the constant depending on the effective masses of electrons in the conduction band and holes in the valence band. n- takes the values ½, 2, 3/2, or 3.

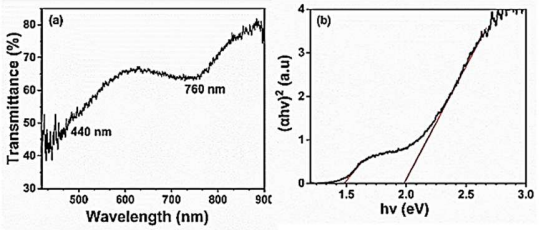

Figure 2. (a) Transmittance vs wavelength of 5L cobalt oxide film prepared by dip coating technique; (b) Tauc plot of the same sample.

It is n=1/2 for direct allowed one, n=2 for indirect allowed, n=3/2 for direct unallowed, and n= 3 for indirect unallowed transition [37]. Fig. 2(b) shows the Tauc plot of $(\alpha h\upsilon)^2$ versus $h\upsilon$ of Co_3O_4 thin films.

The extrapolation of the linear portion to zero absorption coefficient gives band gap energy (E_g) of the sample. The plot consists of two straight line regions, designated as A) at low energy side, and B) at higher energy side. The extrapolation of low energy region (A) leads to the intercept at 1.48 eV whereas in region (B), the extrapolation leads to the intercept at 1.98 eV. These intercepts give band gap (E_{g1} and E_{g2}) of deposited films which quite match with that of the literature [38].

ELECTROCATALYTIC CHARACTERIZATION FOR OER

Linear Sweep Voltammetry Analyses

Oxygen Evolution Reaction (OER) of cobalt oxide thin film of different layer was studied using 0.1 M KOH electrolyte. The OER of alkaline water electrolysis was explored with linear sweep voltammetry (LSV) at applied voltage range of 0 V to 0.08 V and scan rate of 10 mV/s. The voltammograms of cobalt oxide thin films of 5, 10 and 15 L, along with uncoated (0 L) steel are presented in **Figure 3.**

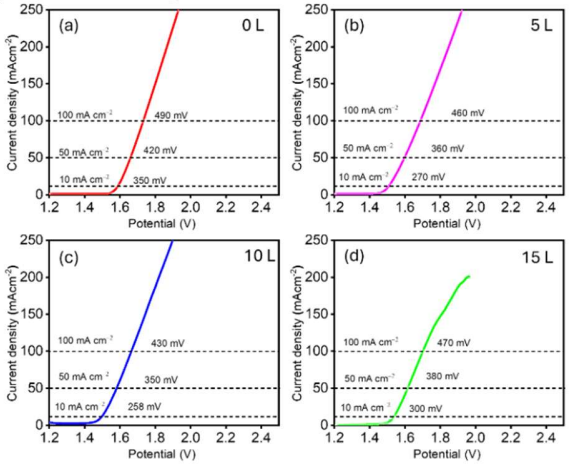

Figure 3. Linear sweep voltammogram of various layered dip-coated cobalt oxide films (a) 0 L, (b) 5 L, (c) 10 L, (d) 15 L measured at 10 mV/s scan rate.

The figure clearly shows that the variation of OER overpotentials of cobalt oxide-coated thin films is lower than that of uncoated steel. It indicates that cobalt oxide-coated thin films evolve oxygen with less energy. E_{RHE} is calculated from the Nernst equation as depicted in equation 3.

$$E_{RHE} = E_{observed} + E^0\,(\text{SCE}) + 0.059^*\ \text{pH} \ldots\ldots\ldots\ldots [3]$$

The overpotential (η) of thin films at 10 $mAcm^{-2}$ current density was calculated using the relation, overpotential, η (V) = E_{RHE} - 1.23

In **Figure 3**, the LSV curves show the variation in OER overpotentials. For the 0 L electrode, the overpotentials are 350, 420, and 490 mV at current densities of 10, 50, and 100 mA cm^{-2}, respectively. In addition, For the 5 L electrode, the overpotentials are 270, 360, and 460 mV at current densities of 10, 50, and 100 mA cm^{-2}, respectively. For the 10 L electrode, the overpotentials are 258, 350, and 430 mV at current densities of 10, 50, and 100 mA cm^{-2}, respectively. For the 15 L electrode, the overpotentials are 300, 380, and 470 mV at current densities of 10, 50, and 100 mA cm^{-2}, respectively. From the as aforementioned electrode and respective OER potentials, it can be observed that the overpotential at current densities 10, 50, and 100 $mAcm^{-2}$ gradually decreased with an increase in the number of layers of cobalt oxide up to 10L, beyond that, it tends to fluctuate.

The variation in overpotentials with increasing cobalt oxide layers can be attributed to changes in active surface area, charge transfer efficiency, and material properties. Up to 10L, the decreasing overpotential suggests improved catalytic performance due to an expansion of the electrochemically active surface area, as supported by XRD findings. This enhancement facilitates better charge transfer and increases the accessibility of active sites, optimizing OER activity. However, beyond 10L, the overpotential begins to fluctuate, likely due to mass transport constraints, higher charge transfer resistance, and structural issues arising from excessive film thickness. A thicker layer may reduce electrical conductivity and limit active site exposure, thereby lowering catalytic efficiency. Additionally, the increase in current density at a fixed potential with more layers indicates enhanced charge transport and surface reactivity up to 10L. Overall, the LSV results suggest that 10L provides the ideal balance between the surface area, conductivity, and charge transfer, making it the most effective for OER.

Conclusions

In this study, cobalt oxide (Co_3O_4) thin films were successfully synthesized using a simple yet effective dip-coating technique. The optical absorbance peaks at 440 nm and 760 nm in the visible light spectrum confirm the formation of Co_3O_4, further validated by the Tauc plot, which revealed two distinct band gaps of 1.48 eV and 1.98 eV, corresponding to direct allowed and forbidden transitions. XRD analysis confirmed the formation of nanostructured Co_3O_4 thin films with well-defined crystallinity. Electrochemical assessment via linear sweep voltammetry (LSV) exhibited that the 10L Co_3O_4-coated steel exhibited reduced overpotentials of 258, 350, and 430 mV at current densities of 10, 50, and 100 mA cm^{-2}, respectively, compared to uncoated steel, highlighting the influence of film thickness on OER performance. LSV also demonstrated that increasing the number of Co_3O_4 layers leads to a significant reduction in overpotential, enhancing OER efficiency. Moreover, a notable increase in current density at a fixed voltage with additional layers indicates improved charge transport and an expanded electrochemically active surface area. These findings underscore the potential of Co_3O_4 thin films as efficient electrocatalysts, highlighting the importance of precise thickness control to optimize performance in energy conversion applications.

Acknowledgments

The authors extend their gratitude to Amrit Campus (ASCOL), Tribhuvan University, for providing laboratory facilities. The authors would like to thank for ISP, UU Sweden for partial support for in completing this research under grant NEP:01, Material Science Division, Atomic Energy Centre Dhaka, Bangladesh for XRD characterization.

Author Contributions

SP: Methodology, Investigation, Formal analysis, Data curation, Writing-original draft preparation **MRK:** Conceptualization, Writing-original draft preparation, Formal analysis, Data curation **LPJ:** Formal analysis and Writing-review and Editing **DKC:** Formal analysis and Editing **SMH:** Formal analysis and Editing **CLG:** Formal analysis and Editing **SPS:** Conceptualization, Resources, Writing-review and Editing, supervision

Conflicts of Interest

The authors declare no conflict of interest.

REFERENCES

1. Gong M, Dai H. A mini review of NiFe-based materials as highly active oxygen evolution reaction electrocatalysts. Nano Res. 2015 Jan 3;8(1):23–39.
2. Kandel MR, Pan UN, Dhakal PP, Ghising RB, Nguyen TT, Zhao J, et al. Unique heterointerface engineering of Ni_2P−MnP nanosheets coupled Co_2P nanoflowers as hierarchical dual-functional electrocatalyst for highly proficient overall water-splitting. Appl Catal B Environ. 2023 Aug;331(February):122680.
3. Bhandari G, Dhakal PP, Tran DT, Nguyen TH, Dinh VA, Kim NH, et al. Pt Single Atom-Doped Triphasic VP-Ni_3P-MoP Heterostructure: Unveiling a Breakthrough Electrocatalyst for Efficient Water Splitting. Small. 2024; 2405952:1–15.
4. Zhao J, Zhang JJ, Li ZY, Bu XH. Recent Progress on NiFe-Based Electrocatalysts for the Oxygen Evolution Reaction. Small. 2020;16(51):1–23.
5. Adhikari A, Chhetri K, Rai R, Acharya D, Kunwar J, Bhattarai RM, et al. (Fe-Co-Ni-Zn)-Based Metal–Organic Framework-Derived Electrocatalyst for Zinc–Air Batteries. Nanomaterials. 2023 Sep 21;13(18):2612.
6. Zheng D, Yu L, Liu W, Dai X, Niu X, Fu W, et al. Structural advantages and enhancement strategies of heterostructure water-splitting electrocatalysts. Cell Reports Phys Sci. 2021;2(6):100443. Available from: https://doi.org/10.1016/j.xcrp.2021.100443
7. Zhang H, Maijenburg AW, Li X, Schweizer SL, Wehrspohn RB. Bifunctional Heterostructured Transition Metal Phosphides for Efficient Electrochemical Water Splitting. Adv Funct Mater. 2020;30(34).
8. Kandel MR, Pan UN, Paudel DR, Dhakal PP, Kim NH, Lee JH. Hybridized bimetallic phosphides of Ni–Mo, Co–Mo, and Co–Ni in a single ultrathin-3D-nanosheets for efficient HER and OER in alkaline media. Compos Part B Eng. 2022;239(March):109992.
9. Tourneur J, Joanny L, Perrin L, Paul S, Fabre B. Efficient and Highly Stable 3D-Printed NiFe and NiCo Bifunctional Electrodes for Practical HER and OER. ACS Appl Eng Mater. 2023;1(10):2676–84.
10. Al-Naggar AH, Shinde NM, Kim J, Mane RS. Water splitting performance of metal and non-metal-doped transition metal oxide electrocatalysts. Coord Chem Rev. 2023 Jan; 474:214864.
11. Kandel MR, Pan UN, Dhakal PP, Ghising RB, Sidra S, Kim DH, et al. Manganese-Doped Bimetallic $(Co,Ni)_2P$ Integrated CoP in N, S Co−Doped Carbon: Unveiling a Compatible Hybrid Electrocatalyst for Overall Water Splitting. Small. 2024 May 21;20(18):1–18.
12. Dhakal PP, Pan UN, Kandel MR, Ghising RB, Prabhakaran S, Kim DH, et al. Cobalt nanoparticles confined nitrogen–doped carbon integrated bimetallic Co_2P–VP heterostructure composite: A MOF integrated 3D arrays for catalytic water splitting. Compos Part B Eng. 2024;283(March):111640.
13. Jamesh MI, Sun X. Recent progress on earth abundant electrocatalysts for oxygen evolution reaction (OER) in alkaline medium to achieve efficient water splitting – A review. J Power Sources. 2018;400(August):31–68.
14. Pan UN, Kandel MR, Tomar AK, Kim NH, Lee JH. Synchronous Surface-Interface and Crystal-Phase Engineered Multifaceted Hybrid Nanostructure of Fe-(1T) -VSe_2 Nanosheet and Fe-$CoSe_2$ Nanorods Doped with P for Rapid HER and OER, Kinetics. Small. 2023 Oct 9; 02305519.
15. Anjum MAR, Bhatt MD, Lee MH, Lee JS. Sulfur-Doped Dicobalt Phosphide Outperforming Precious Metals as a Bifunctional Electrocatalyst for Alkaline Water Electrolysis. Chem Mater. 2018;30(24):8861–70.
16. Chaudhari A, Kandel MR, Ali A, Paudel DR, Dahal B, Subedi S. Ni-doped Co-layered Double Hydroxides as High-performance Electrocatalyst for the Hydrogen Evolution Reaction. J Nepal Chem Soc. 2025 Jan 31;45(1):66–75.
17. Song F, Bai L, Moysiadou A, Lee S, Hu C, Liardet L, et al. Transition Metal Oxides as Electrocatalysts for the Oxygen Evolution Reaction in Alkaline Solutions: An Application-Inspired Renaissance. J Am Chem Soc. 2018;140(25):7748–59.
18. Babar PT, Lokhande AC, Gang MG, Pawar BS, Pawar SM, Kim JH. Thermally oxidized porous NiO as an efficient oxygen evolution reaction (OER) electrocatalyst for electrochemical water splitting application. J Ind Eng Chem. 2018; 60:493–7.
19. Broicher C, Zeng F, Artz J, Hartmann H, Besmehn A, Palkovits S, et al. Facile Synthesis of Mesoporous Nickel Cobalt Oxide for OER – Insight into Intrinsic Electrocatalytic Activity. ChemCatChem. 2019;11(1):412–6.

20. Althomali RH, Adeosun WA. Wet chemically synthesized metal oxides nanoparticles, characterization and application in electrochemical energy storage: An updated review. Synth Met. 2023;298(May):117424. Available from: https://doi.org/10.1016/j.synthmet.2023.117424
21. Munawar K, Mansoor MA, Naeem R, Rizwan M, Ahmad MS, Zaharinie T, et al. Effect of deposition temperature on topography and electrochemical water oxidation of NiO thin films. Thin Solid Films. 2023;782(October 2022):140031.
22. Morales-Guio CG, Liardet L, Hu X. Oxidatively Electrodeposited Thin-Film Transition Metal (Oxy)hydroxides as Oxygen Evolution Catalysts. J Am Chem Soc. 2016;138(28):8946–57.
23. Li SY, Nguyen TX, Su YH, Lin CC, Huang YJ, Shen YH, et al. Sputter-Deposited High Entropy Alloy Thin Film Electrocatalyst for Enhanced Oxygen Evolution Reaction Performance. Small. 2022;18(39):1–11.
24. Sun H, Kim H, Xu X, Fei L, Jung W, Shao Z. Thin Films Fabricated by Pulsed Laser Deposition for Electrocatalysis. Renewables. 2023 Feb 8;1(1):21–38.
25. Trotochaud L, Ranney JK, Williams KN, Boettcher SW. Solution-cast metal oxide thin film electrocatalysts for oxygen evolution. J Am Chem Soc. 2012;134(41):17253–61.
26. S. C. Bulakhe, R. J. Deokate. Nickel Oxide Thin Films for Oxygen Evolution Reaction. Int J Adv Res Sci Commun Technol. 2023 Mar 16;3(1):543–7.
27. Babar N-U-A, Asghar MN, Hussain F, Joya KS. Spray-assembled nanoscale cobalt-oxide as highly efficient and durable bifunctional electrocatalyst for overall water splitting. Mater Today Energy. 2020 Sep; 17:100434.
28. Wu Q, Mellin M, Lauterbach S, Tian C. Materials Advances. Mater Adv. 2024; 5:2098–109.
29. Mokdad S, Boukazoula A, Chouchane K, Saib F, Trari M, Abdi A. Electrocatalytic activity of electrodeposited - CoO_x thin film on low - carbon unalloyed steel substrate toward electrochemical oxygen evolution reaction (OER). Chem Pap. 2023;77(9):4979–92.
30. Liu H, Li Z, Hu J, Qiu Z, Liu W, Lu J, et al. Self-supported cobalt oxide electrocatalysts with hierarchical chestnut burr-like nanostructure for efficient overall water splitting. Chem Eng J. 2022;435(P2):134995. Available from: https://doi.org/10.1016/j.cej.2022.134995
31. Acedera RAE, Gupta G, Mamlouk M, Balela MDL. Solution combustion synthesis of porous Co_3O_4 nanoparticles as oxygen evolution reaction (OER) electrocatalysts in alkaline medium. J Alloys Compd. 2020; 836:154919.
32. Ghising RB, Pan UN, Kandel MR, Dhakal PP, Prabhakaran S, Kim DH, et al. Bimetallic–organic frameworks derived heterointerface arrangements of V, N co-doped Co/Fe–selenide nanosheets electrocatalyst for efficient overall water-splitting. Mater Today Nano. 2023 Dec;24(August):100390.
33. Dhakal PP, Pan UN, Kandel MR, Ghising RB, Nguyen TH, Dinh VA, et al. Cobalt phosphide integrated manganese-doped metallic 1T-vanadium disulfide: Unveiling a 2D-2D tangled 3D heterostructure for robust water splitting. Chem Eng J. 2023 Oct;473(August):145321.
34. Ghising RB, Pan UN, Kandel MR, Dhakal PP, Sidra S, Kim DH, et al. Ruthenium single atoms implanted on NiS_2-FeS_2 nanosheet heterostructures for efficacious water electrolysis. J Mater Chem A. 2024;12(6):3489–500.
35. Chougule MA, Pawar SG, Godse PR, Sakhare RD, Sen S, Patil VB. RETRACTED ARTICLE: Sol–gel derived Co_3O_4 thin films: effect of annealing on structural, morphological and optoelectronic properties. J Mater Sci Mater Electron. 2012 Mar 12;23(3):772–8.
36. Vasant Dilwale G. Chemical Synthesis of Cobalt Oxide and Study of Structural Properties. Int J Sci Res. 2021 Nov 27;10(11):839–41.
37. Louardi A, Rmili A, Ouachtari F, Bouaoud A, Elidrissi B, Erguig H. Characterization of cobalt oxide thin films prepared by a facile spray pyrolysis technique using perfume atomizer. J Alloys Compd. 2011;509(37):9183–9.2011.06.106
38. Louardi A, Rmili A, Chtouki T, Elidrissi B, Erguig H, Bachiri A El. Effect of annealing treatment on Co_3O_4 thin films properties prepared by spray pyrolysis. 2017;8(2):485–93.

Nanomaterials and Polymers Innovations Vol. 1, No. 1 (2025); 40-49
ISSN: 3102-0798 (Online). Available online at www.nepalpolymer.org
DOI:https://doi.org/……xyz……..xyz (to be updated)

Original research article

Synthesis of Zinc Oxide Nanocatalyst and Its Application in Photodegradation of Rhodamine B

Shukra Raj Regmi[1*], Nurul Hoda Khan[1], Narendra Prakash Shawd[1], Dikpal Kumar Shahi[1], Lekha Nath Khatiwada[2], Rameshwar Adhikari[3*]
[1]*Central Department of Biological and Chemical Sciences, Mid-West University, Surkhet, Nepal*
[2]*Department of Customs, Ministry of Finance, Tripureshwar, Kathmandu, Nepal*
[3]*Research Centre for Applied Science and Technology (RECAST), Tribhuvan University, Kirtipur, Kathmandu 44618, Nepal*

Abstract: We synthesized zinc oxide nanoparticles (ZnO-NPs) by the co-precipitation method for the catalytic degradation of Rhodamine B. The obtained nanoparticle was characterized by a UV-visible spectrophotometer, FTIR (Fourier Transform Infra-Red), EDX (Energy Dispersive X-ray), and XRD crystallography. The ZnO-NPs have shown maximum absorbance intensity at 365 nm, and an optical band gap of 3.29 eV based on Tauc plot. The FTIR spectra reveal strong stretching of Zn-O at 779.11 cm^{-1}. The EDX spectra depicted 81.90 % zinc (Zn), and 17.99 % oxygen (O) as an elemental composition. The XRD spectra show hexagonal wurtzite geometry. Solving Scherrer's equation, we obtained the average size of the particle 23.9 nm, and the crystallinity 75.43%. The solar light intensity 5.74±0.14 kWh/m^2/day was used to degrade Rhodamine B completely within 140 minutes with ≈80% catalytic efficiency, and in the dark medium, the degradation is found prolonged up to 220 minutes with ≈15% efficiency. The degradation in heat and light is achieved in 110 minutes at 110 °C. The degradation of dye obeys pseudo-first-order kinetics and the rate constant is obtained at 0.01274 min^{-1} in light. The finding reveals that photocatalytic degradation under controlled temperature is superior to the degradation achieved in light and dark. The mineralization of Rhodamine B demonstrates the potential application of ZnO-NPs as a photocatalyst.

Keywords: photocatalysis, ZnO-NPs, Rhodamine B, dye degradation, nanocatalyst

शोधसार: प्रस्तुत अनुसन्धानमा हामीले रोडामिन बी को उत्प्रेरक क्षयका लागि को-प्रेसिपिटेसन विधिबाट जिंक अक्साइड न्यानोपार्टिकल्स (ZnO-NPs) संश्लेषण गरेका छौं। प्राप्त न्यानोपार्टिकललाई यूभी-भिजिबल स्पेक्ट्रोफोटोमिटर, FTIR (फोरियर ट्रान्सफर इन्फ्रारेड), EDX (एनर्जी डिस्पर्सिभ एक्स-रे), र XRD क्रिस्टालोग्राफीद्वारा विशेषण गरिएको छ। ZnO-NPs ले ३६५ nm मा अधिकतम अवशोषण तीव्रता देखाएको छ र टक प्लटको आधारमा ३.२९ eV को अप्टिकल ब्यान्ड ग्याप पाइएको छ। FTIR स्पेक्ट्राले ७७९.११ cm^{-1} मा Zn-O को बलियो स्ट्रेचिङ देखाउँछ। EDX स्पेक्ट्राले तत्त्वीय संरचना अनुसार ८१.९०% जिंक (Zn) र १७.९९% अक्सिजन (O) रहेको देखाएको छ। XRD स्पेक्ट्राले हेग्जागोनल वुर्टजाइट ज्यामिती देखाउँछ। शेरेरको समीकरण प्रयोग गर्दा, कणको औसत आकार २३.९ nm र क्रिस्टलिनिटी ७५.४३% पाइएको छ। सौर्य प्रकाशको तीव्रता ५.७४±०.१४ kWh/m^2/day प्रयोग गरेर रोडामिन बी लाई १४० मिनेटभित्र पूर्ण रूपमा क्षय गरिएको छ, जसमा ≈८०% उत्प्रेरक दक्षता देखिएको छ; अन्धकार वातावरणमा क्षय प्रक्रिया २२० मिनेटसम्म विस्तार भएको छ र दक्षता ≈१५% मात्र देखिएको छ। ताप र प्रकाशमा भने क्षय ११०°C मा ११० मिनेटभित्र सम्पन्न भएको छ। रङको क्षय प्रक्रियाले स्यूडो-प्रथम-अर्डर काइनेटिक्स पालना गर्छ र प्रकाशमा क्षय दर स्थिरांक ०.०१२७४ प्रतिमिनेट पाइएको छ। अनुसन्धानले देखाउँछ कि नियन्त्रित तापक्रममा गरिएको फोटोउत्प्रेरक क्षय प्रक्रियाले केवल प्रकाश वा अन्धकारमा गरिएको क्षयभन्दा उत्कृष्ट परिणाम दिन्छ। रोडामिन बी को मिनरलाइजेसनले ZnO-NPs लाई फोटोउत्प्रेरकको रूपमा प्रयोग गर्न सकिने सम्भावना देखाएको छ।

INTRODUCTION

Zinc oxide is a naturally intrinsic n-type semiconductor having a wide band gap of 3.37 eV (1). It is considered one of the most promising nanocompounds in the multidisciplinary field, and it is used in industries, medicine, electrical

Corresponding authors, E-mails: shukra.regmi@mu.edu.np (SRR) and nepalpolymer@yahoo.com (RA)
© Nepal Polymer Institute, Kathmandu, Nepal
Received: April 18, 2025; Revised: May 5, 2025; Accepted: May 12, 2025; Published: May 19, 2025

appliances, advanced semiconducting materials, research, and innovation (2). Zinc oxide-based nano derivatives have revolutionized the world with their tremendous applications in each field, including the polymer industry, drug design, pollutant remover, sensors, cosmetic products, and anti-cancerous and photosensitive products (3). The burgeoning use of ZnO-NPs has made an inalienable bond between technology and human welfare (4). The cost-efficient and less toxic nature of ZnO-NPs synthesis has made the research community a favorite nanomaterial in different research fields. The high electron mobility and wide band gap have made the ZnO-NPs a unique semiconductor, so; it is kept as one of the most prominent and promising candidates in material science (5).

Recently, different techniques are frequently used for the synthesis of ZnO-NPs, including precipitation/co-precipitation, hydrothermal technique, physical vapor deposition, impeded laser beam, sol-gel method, green synthesis, thermal decomposition, spray pyrolysis, and various mechano-chemical processing (6). The common approach applied in the synthesis of ZnO-NPs is the precipitation method. Reports have shown that different precursor concentrations based on zinc acetate $Zn(CH_3COO)_2.2H_2O$, zinc nitrate ($ZnNO_3$), zinc chloride ($ZnCl_2$), zinc sulphate ($ZnSO_4$) with appropriate stabilizers like gelatin, starch, DEA (diethanolamine), under suitable temperature give fine ZnO-NPs with variable shape and size. The precursor solution of zinc sulphate and sodium hydroxide, when vigorously shaken and followed by calcination, gives fine ZnO-NPs (7). Another report has shown that a mixture of zinc salt with precipitant NaOH in an ethanol solution stirred at 9 0°C for 1 hour gives ZnO nanorods (8). A similar process for the solvothermal process gives 33±2 nm, and 48±7 nm ZnO-NPs by taking $Zn(NO_3)_2.6H_2O$ precursor with ethanol solution (9). Another faster and cost-efficient method shows that 0.1 M concentration of zinc acetate dihydrate with propanol boiling with constant stirring at 70 °C turns into a milky solution, which is stabilized by 5-6 drops of DEA (diethanolamine), giving a transparent solution. The spin coating on the substrate by heating the film at 120°C for 5 minutes and annealing at 350°C for 15 minutes gives ZnO thin film (10).

For the synthesis of ZnO-NPs, different factors should be maintained under the laboratory parameters such as the concentration of precursor, pH of the solution, aging of the solution while stirring and settling precipitation, purification, and finally drying (11). These factors generally control the shape, size, crystallinity, and morphology of the particles. Reports show that the precursor concentration highly influences the formation of particle size. High precursor concentration increases the rate of nucleation of the particle and enhances the chance for the formation of smaller nanoparticles, which increases surface reactivity by affecting the surface area to volume ratio. Sensing and catalytic properties are determined by the smaller particles (12,13). Moreover, low precursor concentration forms larger nanoparticles and reduces the chances of nucleation under controlled circumstances; as a result, less reactive particles with a smaller surface area to volume ratio are obtained (14). Size and morphology maintenance is another tedious task in ZnO-NPस synthesis. Higher precursor concentrations increase the chances of aggregation to get fine and homogeneous particles; however, irregular and non-crystalline particles are synthesized by the low precursor concentration due to low agglomeration. Precursor concentration also affects the optoelectronic properties, band gap energy, and size of particles (15). In the present work, we have synthesized ZnO-NPs for the catalytic degradation of Rhodamine B under controlled pH conditions to compare the catalytic efficiency with existing parameters.

Although we have existing studies to explore photocatalytic degradation by ZnO-NPs in different parameters, controlled pH with tailored temperature-based synthesis is specifically remarkable. Such a method provides the variation in size of the particle, is easy to control, and allows the formation of defect-free particles. The pure ZnO-NPs effectively show their optical property, which avoids possible recombination. This study aims to degrade Rhodamine B to establish the catalytic strength in controlled laboratory parameters. The fundamental rationale for choosing Rhodamine B is considering it as a model pollutant dye. The excess

use of Rhodamine B in textile, leather, dye industry, biological processing, as a tracer in underground water flow, biological strain, and florescent has made the water resources a pollutant. In the present work, our objective is to investigate the minimum quantity of ZnO-NPs requirement for the effective mineralization of dye for the purification of wastewater(16–19).

MATERIALS AND METHODS

Materials

Zinc acetate dihydrate ($Zn(CH_3COO)_2.2H_2O$, CAS no. 5970-45-6, 219.50 g/M, 98.5 %) and sodium hydroxide (NaOH, CAS no. 1310-73-2, 40 g/M, 97 %) were purchased from Qualigen, India. Polyethylene glycol (PEG, $HO(C_2H_4O)_n^7H$, 100 g/L, CAS no. 25322-68-3) was purchased from Merc, India. Ethanol (C_2H_5OH, 99.99 %, 46.06 g/M, CAS no. 64-17-5) was purchased from Fusion Biotech, India. Rhodamine B ($C_{28}H_{31}ClN_2O_3$, 479.02 g/M, CAS no. 81-88-9) was purchased from Sigma, Aldrich Chemicals, Pvt., India.

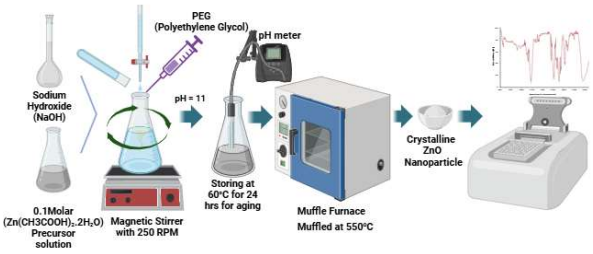

Figure 1. The schematic representation for the synthesis pathway of ZnO-NPs and its characterization.

The overall research design of the present project is depicted in Fig. 1. The decimolar zinc acetate dihydrate precursor was prepared by adding 21.95 g in 1L deionized distilled water. Similarly, decimolar sodium hydroxide was prepared by dissolving 4 gm in 1L water. Both solutions were stirred for 20 minutes at 25ºC. The process was achieved by dropping sodium hydroxide from the burette until the pH of the solution was maintained at 11, at constant stirring of 250 rpm in 50 mL zinc acetate solution. The synthetic pathway is carried out by the formation of zinc hydroxide. The polyethylene glycol (PEG) was added continuously dropwise to avoid the agglomeration of the precipitate mass. After 1 hour of stirring in a thermoregulatory stirrer, the mass was kept for one hour at room temperature for aging. The process was followed by keeping the obtained mass at 80ºC in a hot-air oven. The dry zinc hydroxide mass was scrapped and kept on a silica crucible for calcination at 550 °C. The dry crystalline white powder obtained is represented as ZnO-NPs in the experiment, which was stored in a dry borosilicate airtight container.

Characterization of ZnO-NPs

The synthesized zinc oxide nanoparticles (ZnO-NPs) are characterized by modern spectroscopic techniques. The UV-visible spectrophotometer (UV-1900i, Shimadzu, Japan) was used to find out the maximum absorbance of the nanoparticle. The Fourier-Transform Infrared Spectroscopy (FTIR, IR Affinity-1s, Shimadzu, Japan) was used to find out the vibrational spectra of the zinc oxide bond. The energy-dispersive X-ray (EDX-8000, Shimadzu, Japan) was used to find out the elemental composition of the nanoparticles. The crystallographic indices of the nanoparticle were obtained by XRD (Bruker, D2 Phaser, Massachusetts, USA).

Photocatalytic activity of ZnO-NPs

Photocatalytic degradation was achieved in the solar light having an intensity of 5.64 ± 0.14 kWh/m^2/day. The solar intensity is measured by CMP3 pyranometer. Zinc oxide is a semiconductor that absorbs light having an intensity equal to the band gap or greater than the band gap. The ZnO-NPs are an intrinsic n-type semiconductor that absorbs photons that excites the electron from the valence band to the conducting band as a result free electron-hole pairs are formed. These pairs form free radicals and superoxide, which causes the mineralization of dye. Generally, photocatalytic degradation obeys zero-order kinetics, which can be determined by the following relations.

$$-K_t = \ln \frac{C_t}{C_o} \quad \ldots\ldots\ldots (1)$$

where, 'k_t' = Rate constant for Pseudo-First-Order Kinetics, 'C_t' = Concentration of dye at the time't', and 'C_o' = Initial concentration of dye.

The following relation calculates the catalytic efficiency (20).

$$\text{Degradation (\%)} = \frac{C_o - C_t}{C_o} \quad \ldots\ldots\ldots\ldots (2)$$

The photocatalytic degradation mechanism can be explained in the following chemical equations.

$$\text{ZnO-NPs} \xrightarrow{h\nu} \text{ZnO}(e^-)_{CB} + \text{ZnO}(H+)_{VB} \quad \ldots(3)$$

$$\text{ZnO(Hole+)}_{VB} + H_2O \rightarrow H^+ + OH^- \text{(ions)} \quad \ldots(4)$$

$$\text{ZnO (Hole+)}_{VB} + OH^- \rightarrow OH^{\cdot} \text{(Radicals)} \quad \ldots(5)$$

$$4OH^- \text{(Solution)} \rightarrow 2H_2O + O_2 \quad \ldots(6)$$

$$\text{ZnO(e-)}_{CB} + O_2 \rightarrow {}^{\cdot}O_2^- \text{(Superoxide)} \quad \ldots(7)$$

$$\text{Rhodamine B} + OH^- \text{(Radical)} \rightarrow CO_2 + H_2O \ldots(8)$$

$$\text{Rhodamine B} + O_2^- \rightarrow CO_2 + H_2O \quad \ldots(9)$$

RESULTS AND DISCUSSION

UV-visible Spectra of ZnO-NPs

The results obtained from the UV-vis spectrophotometry are presented in Fig. 2

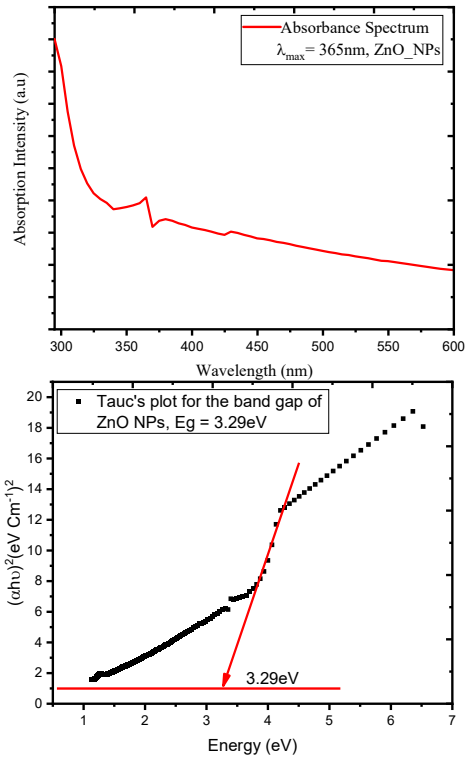

Figure 2: UV-visible spectra of ZnO-NPs showing maximum absorbance at 365 nm (a) and Tauc plot for the determination of band gap of ZnO-NPs showing E_g = 3.29 eV (b).

The maximum wavelength absorbed by ZnO-NPs was found at 365 nm (Fig. 2a). The Tauc plot was obtained based on the absorbance (Fig. 2b). The band gap of ZnO-NPs is found to be 3.29 eV, which is almost equal to the reported band gap (21). The calculation shows that the synthesized ZnO-NPs have a wide band gap but are very efficient in absorbing light. This band gap signifies that the nanomaterial is thermally stable and has a low intrinsic carrier to conduct electricity in the conductance band (22,23). By solving Brus's equation, we obtained the size of particle 1.31 nm at wavelength 365 nm. The optical band gap 3.29 eV is obtained using Tauc plot. The Brus's equation can be defined as:

$$E_{QD} = E_g + \frac{h^2\pi^2}{2R^2}\left(\frac{1}{m_e} + \frac{1}{m_h}\right) - \frac{1.8e^2}{4\pi\ {}_o\varepsilon R} \quad \ldots\ldots(10)$$

where, 'E_{QD}' is the band energy of quantum dot, 'E_g' is the bulk band gap, 'm_e' and 'm_h' are the mass of electron and hole, ϵ_o is the permittivity of vacuum, and ε is the dielectric constant (24). Tauc's equation is used to calculate optical band gap (25).

$$\alpha h\vartheta = A(h\vartheta - E_g)^n \quad \ldots\ldots\ldots\ldots (11)$$

The energy $h\vartheta$(eV), is calculated as;

$$h\vartheta(\text{eV}) = \frac{1240}{\lambda} \ldots\ldots\ldots\ldots\ldots\ldots\ldots (12)$$

FTIR Spectra Analysis for ZnO-NPs

FTIR analysis of ZnO-NPs shows its characteristic peak in different wavenumbers (Fig. 3). The particles show the trapped water molecule showing its strong O-H stretching in 3448.96 cm^{-1}. Spectra also reveals O-H bending at 1597.83 cm^{-1}.

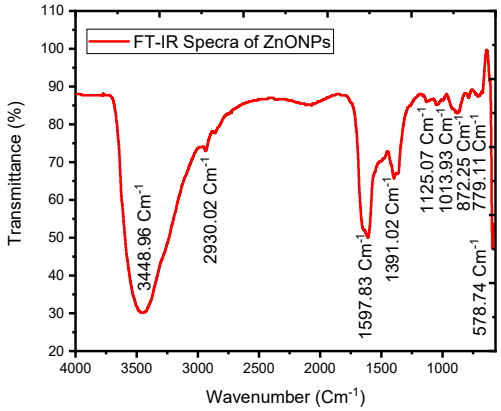

Figure 3: FTIR analysis for zinc oxide nanoparticles (ZnO-NPs)

The small extent of bending found in 2930.02 cm^{-1} shows the stretching of the C-H bond found in the sample, which is due to the precursor of zinc acetate

prepared in organic solvent. The distinct stretching in 578.74 cm^{-1} shows the presence of Zn-O in the sample. The additional bending of Zn-O found in 1013.93, 827.25, 779.11 cm^{-1} confirms the presence of zinc oxide nanoparticles in the sample (26–29).

EDX Analysis for Elemental Composition

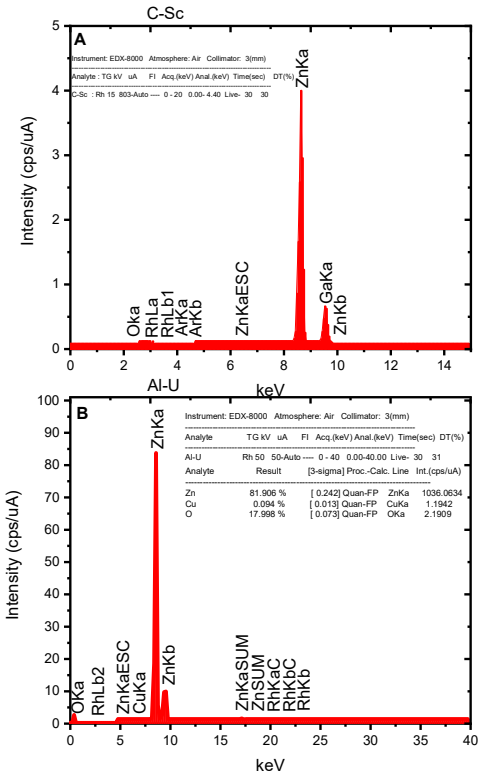

Figure 4: A) EDX spectra of ZnO-NPs showing the elemental composition in C-Sc, and B) EDX spectra of ZnO-NPs showing high resolution of Al-U mode, showing the elemental composition of zinc and oxygen.

The EDX spectra of the samples presented in Fig. 4 reveal that the elemental composition of 81.90% zinc (Zn) and 19.99% oxygen (O). The sharp and significant peak obtained in different energy ranges shows the presence of zinc oxide nanoparticles. The dispersive peak spectra obtained at Al-U mode show the oxygen peak of energy 3.56 keV and Intensity (0.23 cps/uA). Furthermore, the peak of zinc shows an energy of 8.59 keV and an Intensity of 84.63 cps/uA). The peak obtained for zinc with an energy of 9.52 keV, and an intensity of 10.78 also confirms the presence of zinc oxide nanoparticles in the sample (30–32).

XRD Crystallographic Analysis for the ZnO-NPs

Crystallography of ZnO-NPs depicts its sharp peak at the plane 101 (2θ = 35.5°), 111 (2θ = 34.28°), 102 (2θ = 47.30°), 110 (2θ = 56.47°), 103 (2θ = 62.67°), 112 (2θ = 67.79°), 200 (2θ = 68.86°, Intensity 388.37), 201 (2θ = 76.74°, Intensity 106.96), 202 (2θ = 81.23°), 002 (2θ = 29.59°). For ZnO-NPs, the obtained 2θ = 36.5° for 111 plane which gives 0.3185 radians. The FWHM (β) obtained ≈0.35°, and β radians = 0.00611. Solving Scherrer's equation the diameter of the ZnO-NPs gives a crystallite size of 23.9 nm and crystallinity of 75.43 %. The obtained crystalline size and crystallinity confirms the presence of ZnO NPs (33,34)

$$D = \frac{K\lambda}{\beta \text{Cos}\theta} = \frac{0.9 \text{ x } 1.5406 \text{ x } 10^{-10}}{0.00611 \text{ x Cos } (0.3185)}$$

$$= 2.39 \text{ x } 10^{-8} \text{ meter } = 23.9 \text{ nm}$$

The crystallinity is obtained by the following relation.

$$\text{Crystallinity}(\%) = \frac{\text{Crystalline Area}}{\text{Total Area (Crystalline + Amorphous)}} \text{x} 100$$

$$= \frac{12759.66}{16914.58} \text{ x } 100 = 75.43\%$$

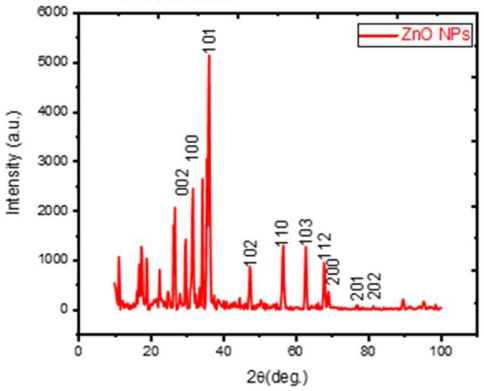

Figure 5: X-ray diffraction pattern of ZnO-NPs.

The X-ray diffractogram of the NPs is presented in Fig. 5. The analysis of the X-RD crystallographic peaks confirms the presence of zinc oxide nanoparticles with wurtzite geometry. The 3D geometric pattern of the particle shows the distinct lattice parameters having bond length (a = 3.22, b = 3.22, c = 5.20), and bond angle (α = 90°, β = 90°, γ = 120°). The unit cell volume for the wurtzite structure is found to be 46.962348 $Å^3$. The three-

dimensional crystal structure of the ZnO-NPs is presented in Fig. 6.

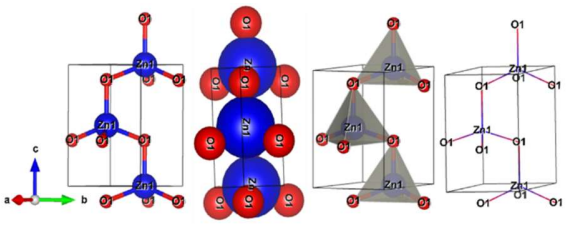

Figure 6: 3D geometric structure of zinc oxide nanoparticles showing the representation in Ball and stick, space-filling, polyhedral, and wireframe structure drawn from VESTA (Visualizing Crystal structures) based on crystallographic open databases (35).

Influence of Light Intensity on ZnO-NPs

Photocatalytic degradation was carried out in the average intensity of light 5.76±0.14 kWh/m^2/day obtained by pyranometer in the days of August 2024. The results are plotted in Fig. 7.

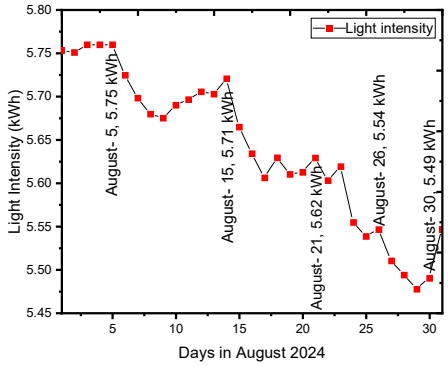

Figure 7: Photo intensity of light in August 2024, obtained by using CMP3 pyranometer in Gurashe, Surkhet, Nepal

The photocatalytic degradation of Rhodamine B was achieved by the action of ZnO-NPs in the presence of light. When ZnO-NPs are added to Rhodamine B dye, the degradation process starts on exposure to light with an intensity of 5.76±0.14 kWh/m^2/day. The degradation process was carried out by adding 10 mg of the NPs in 100 mL of Rhodamine B solution. The degradation mechanism is achieved by the absorption of light by ZnO-NPs that excites the electron from the valence band to the conduction band (see Fig. 8). The process of absorption and excitation of electrons ultimately creates the electron-hole pairs, which convert OH^- ions into $OH^\cdot$ free radical and superoxide O_2^{-}. The free radicals and superoxides are very reactive intermediates that degrade Rhodamine B into simple molecules like CO_2 and H_2O. Hence, mineralization takes place. The degradation process ultimately discharges the pink color Rhodamine B into the colorless solution, that is measured by the intensity of absorbance on the spectrophotometer. The maximum absorption intensity and degradation intensity of Rhodamine B is recorded at a wavelength of 555 nm.

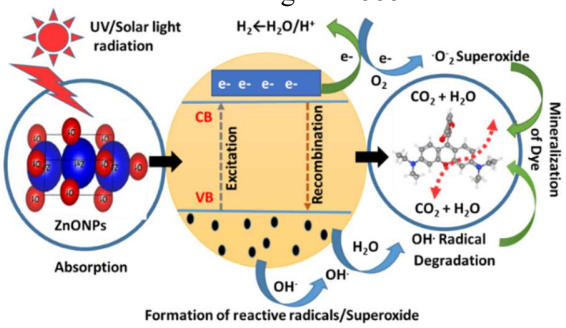

Figure 8: Photocatalytic degradation mechanism of Rhodamine B.

The illustrative mechanism presented in Fig. 8 shows the absorption of photo light, excitation of an electron from the particle surface and formation of holes, formation of hydroxide and superoxide radicals, and recombination and mineralization of dye.

Photocatalytic Degradation of Rhodamine B by ZnO-NPs

The photocatalytic process was carried out by the absorption of photo-light intensity from the exposure of solution over the light having an intensity of 5.76±0.14 kWh/m^2/day. The results are presented in Fig. 9A. Photocatalytic reactions on semiconductor materials like ZnO are very sensitive. Though the calculated band gap is considerably high for the synthesized material, the intensity of solar radiation is huge to generate free radicals and superoxide in the solution. The process is distinctly explained by absorption, excitation, radical and superoxide radical formation, recombination, and mineralization. When 10 mg ZnO-NPs are added to 100 mL of 20 mg/L

Rhodamine B solution in a borosilicate conical flask in exposure to light, the degradation process starts. The initial time at dark was assumed to be zero, and the successive reading was taken in 10 minutes. The light source was not interrupted while the degradation process continued.

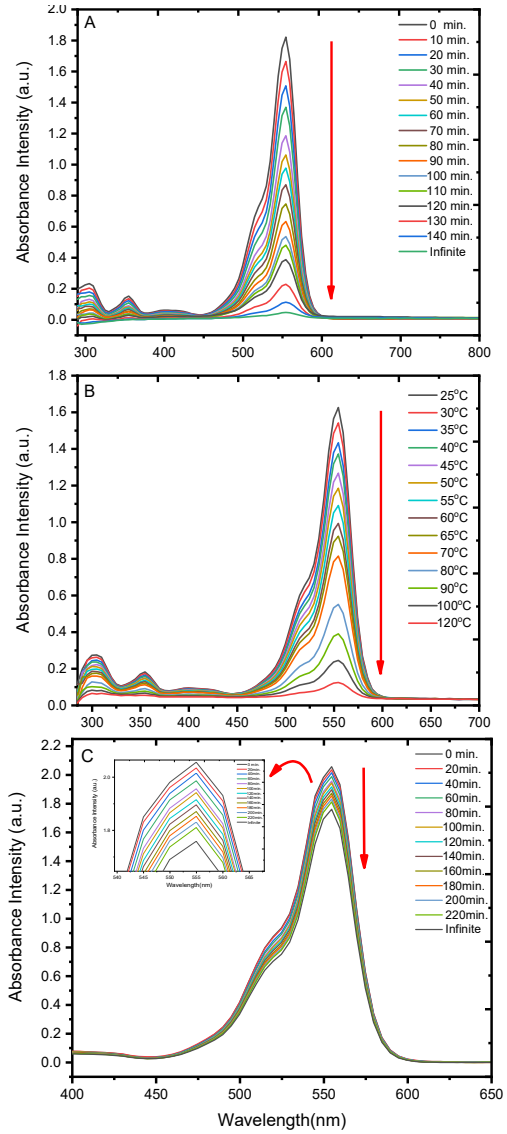

Figure 9: A) Photocatalytic degradation of Rhodamine B in light by ZnO-NPs; B) Photocatalytic degradation of Rhodamine B on increasing temperature by ZnO-NPs, and C) Catalytic degradation of Rhodamine B by ZnO-NPs in dark medium.

The photocatalytic degradation persisted up to 120 minutes for Rhodamine B, which was confirmed by the complete discharge of color and having no absorbance in the spectrophotometer. After the decolorization of pink-colored Rhodamine B, the entire solution was centrifuged at 5400 rpm, where the intact ZnO-NPs settled down at the bottom of the falcon tube that was further used in successive cycles of degradation. Furthermore, the dark medium degradation was achieved by repeating the same process in the absence of light in the dark room (see Fig. 9C). The dark medium degradation was very slow and incomplete up to 220 minutes in consistence with the literature (38,39).

The heating degradation was also achieved in the presence of light. When 10 mg ZnO-NPs were added on 100 mL of 20 mg/L Rhodamine B solution at 25°C, the degradation process was started. The process was continued till the complete degradation occurred for 10-minute intervals in 10 °C difference temperatures (Fig. 9B). The heating degradation was considerably faster than the light and dark medium discharge of Rhodamine B (36,37).

Kinetics of Photocatalytic Degradation for Rhodamine B by ZnO-NPs

The catalytic degradation of Rhodamine B by the ZnO-NPs strictly obeys pseudo-first-order kinetics, as it can be evident from Fig. 10. In the light, the degradation was achieved very fast; the statistical analysis reveals that the linear fitting of $\ln(C/C_o)$ vs. time gives a straight line with a slope -0.01274 and intercept 0.6723 ± 0.0279. The Pearson's 'r' obtained for the degradation is -0.994, with the correlation coefficient (R^2) is 0.989. Similarly, in the dark medium, the degradation was found to fit linearly with a slope of -0.0637 and an intercept of 0.07315 ± 0.02793. The Pearson's coefficient 'r' obtained for dark medium is -0.994 with an adjusted correlation coefficient (R^2) is 0.989, which is equal to the degradation in light. Furthermore, the photocatalytic degradation with the increase in temperature shows the linear fitting with a slope -0.026 ± 0.00058 and intercept of 0.76283 ± 0.11058. The Pearson coefficient 'r' was found -0.9777 with an adjusted correlation coefficient (R^2) is 0.9555.

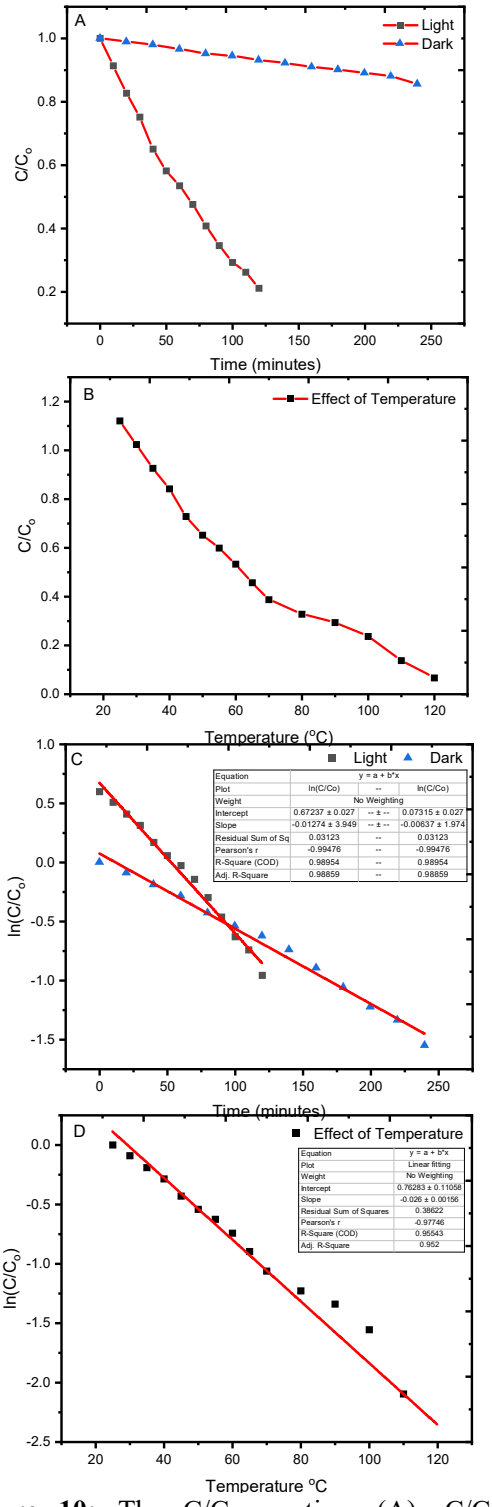

Figure 10: The C/C_o vs time (A), C/C_o vs Temperature (B), and $\ln(C/C_o)$ vs time and temperature plots (C, and D) for the systems studied.

Catalytic Efficiency of ZnO-NPs

The catalytic efficiency of the NPs was calculated by plotting the percentage efficiency versus time (Fig. 11A). For photocatalytic degradation, the efficiency was obtained ≈80% in 120 minutes. Similarly, in the dark, the catalytic efficiency was obtained ≈15% up to 250 minutes, but the efficiency increased ≈90% for the degradation of Rhodamine B in light by heating continuously up to 120 °C (see Fig. 11B).

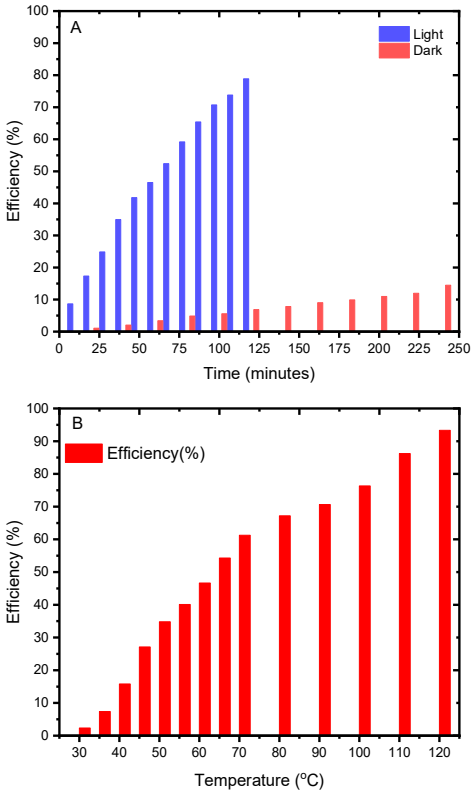

Figure 11: (A) Catalytic efficiency of ZnO-NPs in light and dark, (B). Increased efficiency with temperature in light

Conclusion

The toxicity of dyes on the human body is severe; their degradation into toxic compounds shows several magnitudes of pernicious effects. For the degradation purpose, we synthesized zinc oxide nanoparticles (ZnO-NPs) by the co-precipitation method under controlled pH. The synthesized materials are characterized by a UV-visible spectrophotometer, which gave the maximum absorbance at 365 nm. The band gap was calculated from Tauc's plot, which gave 3.29 eV by the

extrapolation of the obtained plot. The FTIR spectra revealed that Zn-O stretching at 779.11 cm^{-1}. The EDX spectra depicted the elemental composition in the nanoparticles and showed 81.90% zinc (Zn), 17.99% oxygen (O), and trace 0.004 % copper (Cu). The XRD spectra revealed that the ZnO-NPs have wurtzite geometry. On solving Scherer's equation, we obtained the size of particle 23.9 nm and the crystallinity obtained was 75.43 %. The photocatalytic degradation was carried out in 5.74 ± 0.14 kWh/m^2/day light intensity. It was found that the photocatalytic degradation of Rhodamine B obtained in 140 minutes with approximately 80 % catalytic efficiency and in the dark medium, the degradation was very slow and incomplete up to 220 minutes with efficiency ≈15%. The photocatalytic degradation process was completed in 110 minutes at 110°C. The degradation in dark and light both obey pseudo-first-order kinetics and the rate constant was found to be 0.01274 min^{-1} in light and 0.00637 min^{-1} in dark.

Availability of Data and Materials

The data will be made available at any time when requested.

Funding

No funding was available for this research project.

Author Contributions

SR and NHK: raw materials arrangement, preparation, conducting experiments, and manuscript drafting; NPS: analyzing data, literature survey, DKS: results analysis and interpretation; LNK: EDX analysis and supervision; RA: manuscript editing and supervision.

Conflicts of Interests

The authors declare they have no conflict of interest.

Acknowledgments

The authors would like to acknowledge the Nanotechnology Research Laboratory at RECAST, Tribhuvan University, and Mid-West University, Graduate School of Science & Technology, Chemistry Laboratory, for providing the research facilities. Mr. Ramesh Puri's contribution is highly acknowledged for arranging the UV-spectrophotometer through donation.

REFERENCES

1.Vinitha V, Preeyanghaa M, Vinesh V, Dhanalakshmi R, Neppolian B, Sivamurugan V. Two is better than one: Catalytic, sensing and optical applications of doped zinc oxide nanostructures. Emergent Mater. 2021;4:1093,124.

2.Soriano ML, Zougagh M, Valcárcel M, Ríos Á. Analytical Nanoscience and Nanotechnology: Where we are and where we are heading. Talanta. 2018;177:104–21.

3. Jiang J, Pi J, Cai J. The advancing of zinc oxide nanoparticles for biomedical applications. Bioinorg Chem Appl. 2018;2018(1):1062562.

4. Sun Q, Li J, Le T. Zinc oxide nanoparticle as a novel class of antifungal agents: current advances and future perspectives. J Agric Food Chem. 2018;66:11209–20.

5.Kumar SG, Rao KSRK. Zinc oxide based photocatalysis: tailoring surface-bulk structure and related interfacial charge carrier dynamics for better environmental applications. Rsc Adv. 2015;5:3306–51.

6. Zeb A, Gul M, Nguyen TTL, Maeng HJ. Recent progress and drug delivery applications of surface-functionalized inorganic nanoparticles in cancer therapy. J Pharm Investig. 2023;53(6):743–79.

7. Kumar SS, Venkateswarlu P, Rao VR, Rao GN. Synthesis, characterization and optical properties of zinc oxide nanoparticles. Int Nano Lett. 2013;3:1–6.

8.Oliveira APA, Hochepied JF, Grillon F, Berger MH. Controlled precipitation of zinc oxide particles at room temperature. Chem Mater. 2003;15(16):3202–7.

9. Zak AK, Razali R, Majid WHA, Darroudi M. Synthesis and characterization of a narrow size distribution of zinc oxide nanoparticles. Int J Nanomedicine. 2011;1399–403.

10. Ghimire RR, Mondal S, Raychaudhuri AK. Synergistic ultraviolet photoresponse of a nanostructured ZnO film with gate bias and ultraviolet illumination. J Appl Phys. 2015;117(10).

11.Shaba EY, Jacob JO, Tijani JO, Suleiman MAT. A critical review of synthesis parameters affecting the properties of zinc oxide nanoparticle and its application in wastewater treatment. Appl Water Sci. 2021;11(2):48.

12.Zhang R, Khalizov A, Wang L, Hu M, Xu W. Nucleation and growth of nanoparticles in the atmosphere. Chem Rev. 2012;112(3):1957–2011.

13.An K, Somorjai GA. Size and shape control of metal nanoparticles for reaction selectivity in catalysis. ChemCatChem. 2012;4(10):1512–24.

14. Meulenkamp EA. Synthesis and growth of ZnO nanoparticles. J Phys Chem B. 1998;102(29):5566–72.

15. Ischenko V, Polarz S, Grote D, Stavarache V, Fink K, Driess M. Zinc oxide nanoparticles with defects. Adv Funct Mater. 2005;15(12):1945–54.

16. Chong MN, Jin B, Chow CWK, Saint C. Recent developments in photocatalytic water treatment technology: A review. Water Res [Internet]. 2010;44(10):2997–3027.

tps://www.sciencedirect.com/science/article/pii/S00431
35410001739
17.Dihom HR, Al-Shaibani MM, Radin Mohamed RMS, Al-Gheethi AA, Sharma A, Khamidun MH Bin. Photocatalytic degradation of disperse azo dyes in textile wastewater using green zinc oxide nanoparticles synthesized in plant extract: A critical review. J Water Process Eng [Internet]. 2022;47:102705. Available from: https://www.sciencedirect.com/science/article/pii/S2214
714422001489
18.Dodoo-Arhin D, Asiedu T, Agyei-Tuffour B, Nyankson E, Obada D, Mwabora JM. Photocatalytic degradation of Rhodamine dyes using zinc oxide nanoparticles. Mater Today Proc [Internet]. 2021;38:809–15. Available from: https://www.sciencedirect.com/science/article/pii/S2214
785320332193
19.Lam SM, Sin JC, Abdullah AZ, Mohamed AR. Degradation of wastewaters containing organic dyes photocatalysed by zinc oxide: a review. Desalin Water Treat [Internet]. 2012;41(1–3):131–69. Available from: https://doi.org/10.1080/19443994.2012.664698
20.Regmi S, Ghimire KN, Pokhrel MR, Khadka DB. Adsorptive removal and recovery of aluminium (III), iron (II), and chromium (VI) onto a low cost functionalized phragmities karka waste. J Inst Sci Technol. 2015;20(2):145–52.
21.Srikant V, Clarke DR. On the optical band gap of zinc oxide. J Appl Phys. 1998;83(10):5447–51.
22.Özgür Ü, Alivov YI, Liu C, Teke A, Reshchikov MA, Doğan S, et al. A comprehensive review of ZnO materials and devices. J Appl Phys. 2005;98(4).
23.Janotti A, Van de Walle CG. Fundamentals of zinc oxide as a semiconductor. Reports Prog Phys. 2009;72(12):126501.
24.Brus L ~E. Electron-electron and electron-hole interactions in small semiconductor crystallites: The size dependence of the lowest excited electronic state. \jcp. 1984 May;80(9):4403–9.
25.Tauc J, Grigorovici R, Vancu A. Optical properties and electronic structure of amorphous germanium. Phys status solidi. 1966;15(2):627–37.
26.Alwan RM, Kadhim QA, Sahan KM, Ali RA, Mahdi RJ, Kassim NA, et al. Synthesis of zinc oxide nanoparticles via sol–gel route and their characterization. Nanosci Nanotechnol. 2015;5(1):1–6.
27.Fakhari S, Jamzad M, Kabiri Fard H. Green synthesis of zinc oxide nanoparticles: a comparison. Green Chem Lett Rev. 2019;12(1):19–24.
28. Kulkarni SS, Shirsat MD. Optical and structural properties of zinc oxide nanoparticles. Int J Adv Res Phys Sci. 2015;2(1):14–8.
29.Tang E, Cheng G, Ma X, Pang X, Zhao Q. Surface modification of zinc oxide nanoparticle by PMAA and its dispersion in aqueous system. Appl Surf Sci. 2006;252(14):5227–32.
30.Das D, Nath BC, Phukon P, Dolui SK. Synthesis of ZnO nanoparticles and evaluation of antioxidant and cytotoxic activity. Colloids Surfaces B Biointerfaces. 2013;111:556–60.
31.Janaki AC, Sailatha E, Gunasekaran S. Synthesis, characteristics and antimicrobial activity of ZnO nanoparticles. Spectrochim Acta Part A Mol Biomol Spectrosc. 2015;144:17–22.
32. Li LH, Deng JC, Deng HR, Liu ZL, Xin L. Synthesis and characterization of chitosan/ZnO nanoparticle composite membranes. Carbohydr Res. 2010;345(8):994–8.
33. Tian ZR, Voigt JA, Liu J, Mckenzie B, Mcdermott MJ, Rodriguez MA, et al. Complex and oriented ZnO nanostructures. Nat Mater [Internet]. 2003;2(12):821–6. Available from: https://doi.org/10.1038/nmat1014
34.Bindu P, Thomas S. Estimation of lattice strain in ZnO nanoparticles: X-ray peak profile analysis. J Theor Appl Phys [Internet]. 2014;8(4):123–34. Available from: https://doi.org/10.1007/s40094-014-0141-9
35. Momma K, Izumi F. VESTA: a three-dimensional visualization system for electronic and structural analysis. J Appl Crystallogr. 2008;41(3):653–8.
36.Varadavenkatesan T, Lyubchik E, Pai S, Pugazhendhi A, Vinayagam R, Selvaraj R. Photocatalytic degradation of Rhodamine B by zinc oxide nanoparticles synthesized using the leaf extract of Cyanometra ramiflora. J Photochem Photobiol B Biol. 2019;199:111621.
37.Sapkota KP, Lee I, Shrestha S, Islam A, Hanif A, Akter J, et al. Coherent CuO-ZnO nanobullets maneuvered for photocatalytic hydrogen generation and degradation of a persistent water pollutant under visible-light illumination. J Environ Chem Eng [Internet]. 2021;9(6):106497. Available from: https://www.sciencedirect.com/science/article/pii/S2213
343721014743
38. Shahi DK, Regmi SR, Shawad NP, Khan NH, Joshi PR, Khatiwada LN, Adhikari R. Solar Light Driven Degradation of Methylene Blue by Titanium Oxide Nanoparticles (TiO_2 NPs). J Phys Life Sci. 2023;1(1):21–37.
39. Regmi SR, Khan NH, Shawad NP, Shahi DK, Joshi PR, Chetry AB, Khatiwada LN, Adhikari R. Synthesis of Tin Oxide Nanoparticles (SnO_2 NPs) and its Application in the Photocatalytic Degradation of Waste Alizarin dye. J Phys Life Sci. 2023;1(1):38–52.

Nanomaterials and Polymers Innovations Vol. 1, No. 1 (2025); 50-57
ISSN: 3102-0798 (Online). Available online at www.nepalpolymer.org
DOI: https://doi.org/.....xyz.....xyz (to be updated)

Original research paper

Preparation, Structural Characterization, and Biodegradability of Cassava- and Potato-Starch-Based Bioplastics

Aayush Thadarai[1, §], Shreejan Dhakal[1, §], Nelson Rai[1,2,5,6*], Shristi Bhandari[3,5], Bhuwan Budha Magar[1,4], Om Prakash Basyal[2,5,6], Manish Man Shrestha[1,2,5,6*]

[1]*Urbana School of Science, Putalisadak 44605, Kathmandu, Nepal*
[2]*Central Department of Chemistry, Tribhuvan University, Kirtipur 44618, Kathmandu, Nepal*
[3]*Central Department of Zoology, Tribhuvan University, Kirtipur 44618, Kathmandu, Nepal*
[4]*Department of Chemistry, Tri-Chandra M. Campus, Tribhuvan University, Kathmandu, Nepal*
[5]*Research Centre for Applied Science and Technology (RECAST), Tribhuvan University, Kirtipur 44618, Kathmandu, Nepal*
[6]*Nepal Polymer Institute (NPI), P. O. Box 24411, Kathmandu, Nepal*
[*]ORCID: 0009-0003-0086-9689 (MMS)

Abstract: The growing demand for sustainable plastics stems from the environmental hazards posed by conventional petroleum-based products. This study investigates the synthesis and characterization of bioplastics derived from cassava and potato starch and compares their properties with polyethylene. Bioplastics were fabricated using glycerol and acetic acid as plasticizers. Optical microscopy revealed that effective starch gelatinization and uniform plasticizer distribution help prevent microcracking in the material. FTIR (Fourier-transform infrared) spectroscopy confirmed the presence of hydroxyl, carbonyl, and glycosidic bond peaks, indicating successful bioplastic formation. Solubility tests showed that starch-based bioplastics dissolved in both 10% sodium hydroxide and water at 90–100 °C, whereas polyethylene remained insoluble under the same conditions. Moisture interaction tests indicated that cassava bioplastics absorbed water and swelled, while potato-based samples exhibited a weight reduction. Degradability tests demonstrated that cassava and potato bioplastics decomposed within 20 and 15 days, respectively, while polyethylene did not degrade. These findings highlight the potential of starch-based bioplastics as environmentally friendly alternatives to conventional plastics. However, their mechanical properties vary depending on the starch source. Future efforts should focus on optimizing gelatinization and plasticizer incorporation to improve structural integrity and performance.

Keywords: Bioplastic, starch, cassava, potato, polyethylene, biodegradation

शोधसार: परम्परागत प्लास्टिकहरुले वातावरणमा पार्ने नकारात्मक प्रभावका कारण दिगो र वातावरणमैत्री प्लास्टिकको माग दिनप्रतिदिन बढ्दै गएको सन्दर्भमा प्रस्तुत अध्ययनमा स्थानिय बजारमा उपलब्ध एक प्रकारको तरुल र आलुबाट निकलिएको स्टार्चबाट ग्लिसरोल र एसिटिक एसिडलाई प्लास्टिसाइजरका रूपमा प्रयोग गरेर बायोप्लास्टिक बनाई तीनिहरुको गुणहरूलाई पोलीइथिलीनसँग तुलना गरिएको छ। बायोप्लास्टिक बनाउन ग्लिसरिन र एसिटिक एसिड प्रयोग गरिएको छ जसले यसलाई लचिलो बनाउँछ। माइक्रोस्कोपले हेर्दा, स्टार्च राम्रोसँग पकाएर प्लास्टिसाइजर समान रुपले मिलाएमा बायोप्लास्टिक नचर्किने देखियो। फुरियर-ट्रान्सफर्म इन्फ्रारेड परीक्षणले यसमा हाइड्रोक्सिल, कार्बोनिल, र ग्लाइकोसिडिक बोन्डहरू भेटिएकोले बायोप्लास्टिक सफलतापूर्वक बनेको पुष्टि भयो।बायोप्लास्टिकका नमुनाहरुलाई पानी र सोडियम हाइड्रोक्साइडमा परीक्षण गर्दा, ९०–१०० °C मा पग्लिएर घुलेको तर पोलिथिलिन नपग्लिएको पाइयो। पानी अवशोषण परिक्षण अनुसार, नमीले तरुलको बायोप्लास्टिक फुल्लियो भने आलुको बायोप्लास्टिकको तौल घटेको पाइयो। माटोमा कुहिने परिक्षण गर्दा तरुलको बायोप्लास्टिक २० दिनमा र आलुको बायोप्लास्टिक १५ दिनमा कुहिएको तर पोलिथिलिनमा २० दिन सम्म कुनै प्रभाव नपरेको पाइयो। यसले स्टार्चबाट बनेको बायोप्लास्टिक, पेट्रोलियम प्लास्टिकको विकल्प हुन सक्ने देखाउछ। तर तरुल र आलुको बायोप्लास्टिकको गुण फरक फरक छन्। भविष्यमा स्टार्चलाई राम्रोसँग पकाउने र प्लास्टिसाइजर मिलाउने तरिका अझ बढी अध्ययन गर्नुपर्ने देखिन्छ जसवाट ती बायोप्लास्टिकहरुको गुणस्तर र टिकाउपन बढाउन सकिनेछ।

Corresponding author, E-mail: shresthamanishmaan@gmail.com
© Nepal Polymer Institute, Kathmandu, Nepal
Received: April 23, 2025; Revised: May 11, 2025, Accepted: May 12, 2025; Published: May 19, 2025

INTRODUCTION

Bioplastics are materials derived from renewable biological sources such as starch, cellulose, or other polysaccharides, and have emerged as an environmentally favorable alternative to conventional synthetic plastics [1]. Starch is particularly attractive among various biopolymers due to its abundance, low cost, and film-forming capability [2,3]. Starch is a naturally occurring polysaccharide macromolecule that displays polymer-like properties, making it a promising material for producing bioplastics. These bioplastics significantly reduce plastic waste's environmental footprint [4,5]. Many bioplastics allow natural decomposition through micro-organism action because they differ from conventional plastics [6]. In contrast, conventional synthetic polymers like polyethylene (PE), polypropylene (PP), and polystyrene (PS) are produced from petrochemical sources and are characterized as being non-biodegradable and resistant to degradation [7]. However, Plastic has become essential for every aspect of human life, including packaging electronic goods and household items, and transport vehicles. Such polymers derived from non-renewable petroleum resources accumulate in landfills and natural habitats, contributing to pollution and ecological harm that can persist for extended periods of 200 years [8,9]. This increasing concern has accelerated the pursuit of sustainable alternatives, with bioplastics as a strong, promising solution.

Bioplastics exhibit applications across medicine, cosmetics, the automotive industry, food packaging, and agriculture because of their degradability, along with their manufacturing dependence on waste materials [10]. The medical domain discovers beneficial applications for natural waste-based bioplastics because they exhibit reduced potential to cause allergic reactions as compared to petroleum-based materials. Since starch is inexpensive, versatile, and optically clear, it has emerged as the most popular and crucial ingredient in edible and biodegradable films among the different kinds of polysaccharides, including cellulose, gums, starch, and chitosan [11]. The development of advanced technology now enables creative uses of cellulose and starch together with other bio-based materials for food packaging [12,13]. Plastic manufacturers within the sector mostly deploy starch-based polymers together with polylactic acid (PLA) and cellophane materials for their distinct functional properties. The use of biodegradable mulch films in agriculture proves cost-efficient because they reduce both operational expenses and waste disposal expenses as they are designed to be utilized once and then safely combined with soil [14].

However, starch-based bioplastics often face challenges related to mechanical strength, water sensitivity, and durability compared to conventional plastics like polyethylene [15,16]. Recent research has focused on optimizing the formulation of starch-based bioplastics through the use of plasticizers, blending agents, and processing techniques to enhance their physical and chemical properties [17,18]. Comparative studies between bioplastics derived from cassava and potato starch and conventional polyethylene are essential to evaluate their performance, biodegradability, and potential for real-world applications [15].

Another significant concern in bioplastic production is identifying a reliable and sustainable source of starch. Among the various options, cassava and potato starch emerge as promising raw materials, as they are major agricultural sources of starch that are widely cultivated and readily available in many regions [19]. The extraction and development of bioplastics from these starches offers a viable pathway to produce bioplastics. Furthermore, the combined treatment of starch with plasticizers like glycerol and acetic acid allows the creation of flexible and water-soluble films [20]. These films degrade at a much faster rate compared to conventional polyethylene, making them an environmentally friendly alternative [21].

This research article aims to prepare and characterize bioplastics from cassava and potato starch and systematically compare their properties with those of conventional polyethylene. By assessing mechanical, thermal, and biodegradability characteristics, this study seeks to contribute to the development of bioplastics.

MATERIALS AND METHODS

Materials

Cassava and potatoes were obtained from the local market in Kathmandu. Glycerol, acetic acid, 10% NaOH, 10% HNO_3, acetone, benzene, and distilled water were purchased from Kathmandu, manufactured by Himedia Laboratories Pvt. Ltd., India, and used without further purification.

Methods

Preparation of bioplastic: 2 kg of each cassava and potato was weighed, washed, peeled, cut, and soaked in distilled water for 48 hrs. Then they were ground using a clean kitchen blender and decanted for 4 hrs and filtered using a muslin cloth to remove excess water. The filtered mass was then sun-dried for 24 hrs. The dry starch was then mixed with water, glycerol, and acetic acid, which was warmed in a water bath and left to set for a week in a mold [22].

Surface Morphology: Surface morphology characterization was done by using a Boeco BM-800 laboratory binocular microscope and digitally recorded with a Boeco B-CAM 16. The samples were prepared on a glass slide, using immersion oil, and covered with a coverslip.

FTIR analysis: The FTIR spectra were obtained using an IR Affinity-1S FTIR Spectrophotometer (Shimadzu) to analyze species, functional groups, and vibrational modes linked to each peak. The spectra were observed within the 400-4000 cm^{-1} spectral range with a resolution set at 4 cm^{-1}.

Water absorption test: The samples of equal weight (w_1) having similar shapes were prepared and then dipped into the water for 12 hrs. These samples were dried with the help of filter paper to minimize error by removing surface water and weighed (w_2) [22].

Solubility test: The solubility tests were performed in various solvents ranging from polar to non-polar (water, 10% NaOH, 10% HNO_3, ethanol, acetone, and benzene). The prepared samples were cut into small pieces of weight 0.1g and put into 10 mL test tubes containing 5 mL of solvents. The solubility was observed at both room temperature and elevated temperature of 90 °C [22].

Biodegradability test: A biodegradability test was done by using the soil burial method. Samples were cut and weighed to equal 0.1g in similar shapes. These samples were then buried in a box containing moist soil at a depth of 10 cm for 20 days at room temperature and checked for weight loss at every 5-day intervals by cleaning, drying, and weighing the samples [23].

RESULTS AND DISCUSSION

Surface morphology

The study of bioplastic surface features was conducted through optical microscopy. **Figures 1a and 1b** show the distribution of starch and plasticizers, indicating successful blending [24]. These optical micrographs displayed surface fractures accompanied by cracks, which are likely attributed to the presence of α-1,4-glucosidic bonds in the starch matrix, probably due to its naturally amorphous characteristics [25,26].

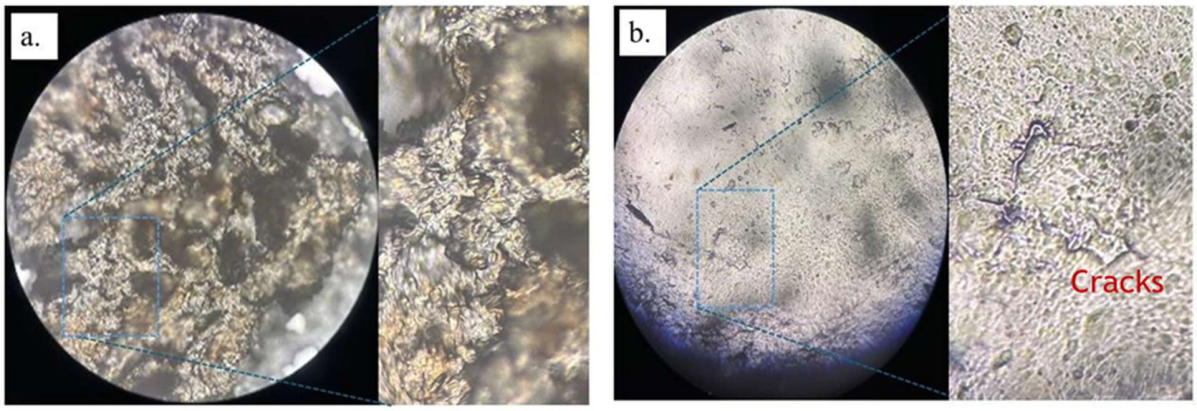

Figure 1. Optical micrographs of **a.** Cassava starch bioplastic and **b.** Potato starch bioplastic.

FTIR analysis

The FTIR spectra of the bioplastics (**Figure 2**) exhibited characteristic peaks confirming the presence of starch, glycerol, and acetic acid. A broad absorption band between 3600–3000 cm^{-1} was observed, corresponding to O–H stretching vibrations, indicating the hydroxyl groups from starch and glycerol [27,28]. The peak at 2929 cm^{-1} was attributed to C–H stretching, representing the alkyl groups present in the biopolymer matrix [27]. A distinct peak at 1643 cm^{-1} was assigned to C=O stretching vibrations, confirming the incorporation of acetic acid within the bioplastic structure [29]. Furthermore, the peak at 1079 cm^{-1} indicated the C–O–C stretching of glycosidic bonds in the starch backbone, while the peak at 1015 cm^{-1} was associated with C–O–H bending vibrations, supporting the presence of polysaccharide and polyol groups [30]. These results collectively confirm the incorporation of glycerol and acetic acid as plasticizers in the successful formation of starch-based bioplastics.

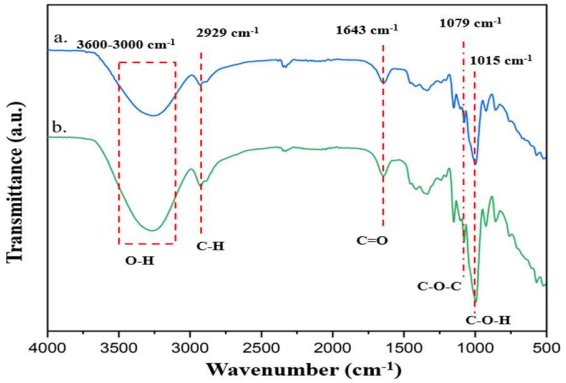

Figure 2. FTIR spectrum of bioplastic **a.** Cassava starch **b.** Potato starch.

Water absorption test

A water absorption analysis involved three plastic types, which included cassava-based bioplastic, potato-based bioplastic, and commercial polyethylene. The weight of each sample before and after being soaked in water was noted as shown in **Table 1**, which is also represented graphically in **Figure 3**.

Table 1. Values of water absorption test on different plastic types.

Sample	Initial Weight (g)	Final Weight (g)	Water Absorption (%)
Cassava bioplastic	0.1	0.17	70
Potato bioplastic	0.1	0.09	-10
Commercial polyethylene	0.1	0.1	0

Among the three samples, cassava showed the highest amount of water absorption, indicating a 70% increase after being soaked in water for 12 hrs. The water molecules entered bioplastics through their porous network and established an interaction with the internal polymer structure [22]. This result was supported by the optical micrograph **(Figure 1),** which indicated the presence of a rupture surface on the plastic materials [26]. The commercial polyethylene sample maintained its constant weight of 0.1 g, indicating 0% water absorption due to its hydrophobic and non-polar structure, as well as its great resistance to water intake [31]. However, the weight of potato-based bioplastic decreased from 0.1 g to 0.09 g after water soaking (**Figure 3**). This is because the materials started dissolving when the aqueous concentration exceeded a specific threshold value [32]. Different water interaction patterns emerge between bioplastic materials and establish synthetic plastic types, according to test observations [33].

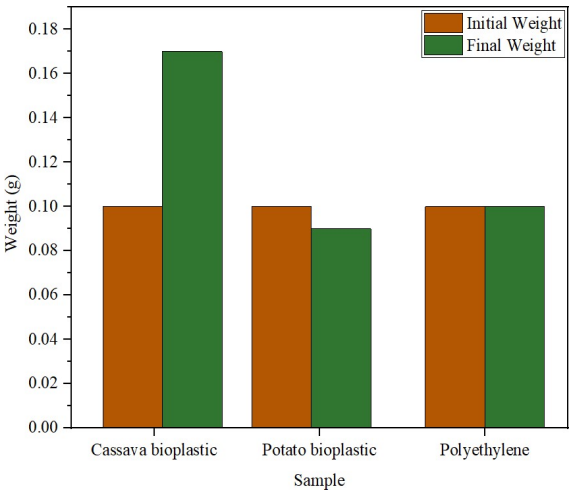

Figure 3. Plot showing weight difference before and after water absorption.

Solubility test

Two types of bioplastics based on cassava starch and potato starch underwent solubility tests involving several solvents under 90 °C and room temperature conditions, which were then compared against traditional polyethylene as indicated in **Table 2**.

Both cassava and potato starch bioplastics showed soluble properties in 10% NaOH at room temperature, yet displayed insolubility against water, 10% HNO_3, ethanol, acetone, and benzene solutions. Exposure to 90 °C allowed the starch-based bioplastics to become partially dissolvable in water and 10% HNO_3, as the elevated temperatures increased their chain network mobility and acidity sensitized them [34]. The dissolving behavior of starch bioplastics in polar solvents and reactive solutions like alkalis and hot water is attributed to the hydrophilic nature of the starch bioplastic that uses hydrogen bonds or hydrolysis to interact with these solvents. The starch-based material's solvent sensitivity matches earlier findings [21,35,36].

Table 2. Solubility test of plastic samples in different solvents.

	Sample	Water	10% NaOH	10% HNO_3	Ethanol	Acetone	Benzene
At room temperature for 24 hrs	Cassava bioplastic	×	✓	×	×	×	×
	Potato bioplastic	×	✓	×	×	×	×
	Commercial polyethylene	×	×	×	×	×	×
At 90 °C	Cassava bioplastic	P. ✓	✓	P. ✓	×	×	×
	Potato bioplastic	P. ✓	✓	P. ✓	×	×	×
	Commercial polyethylene	×	×	×	×	×	×

Note: Insoluble (×), Soluble (✓), Partial soluble (P. ✓)

The tested solvents could not dissolve commercial polyethylene because of its hydrophobic nature, as well as its resistant chemical properties against all solvents [37,38]. This test highlights the biodegradable and environment-responsive characteristics of starch-based bioplastics that are suitable for short-term usage requirements.

Biodegradability test

The test for biodegradability employed the soil burial method. The testing period took place inside one type of soil extending to a depth of 10 cm for 20 consecutive days [39]. The potato starch bioplastic experienced a weight loss of 15% during the first 5 days, and the cassava starch bioplastic lost 20% weight during the same time frame (**Figure 4**). The degradation rate of potato starch bioplastic increased after five days of the experiment and exceeded the degradation rate of cassava starch bioplastic, which may be due to the amylopectin nature, large and porous granules of the potato starch bioplastic that aid the water absorption and increased the rate of degradation process [40,41].

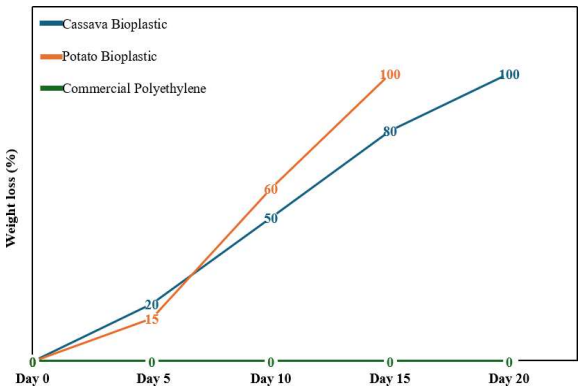

Figure 4. Biodegradability of samples with a percentage loss of the samples at 5-day intervals.

The complete degradation of potato starch bioplastic occurred within 15 days, but cassava starch bioplastic required the full 20-day period to decompose. The film expanded from water absorption from soil and resulted in higher microbial proliferation and enzyme degradation processes that contributed to weight reduction and disruption of the films [23]. On the other hand, the hydroxyl group in starch may have initiated the hydrolysis reaction of the polymer after water absorption, also glycerin, as a hydrophilic plasticizer, reduced the internal hydrogen bond in the polymer chain [42]. Commercial polyethylene did not show any signs of degradation during the 20-day testing period.

CONCLUSION

This research highlights the potential of starch-based bioplastics as a viable biodegradable alternative to conventional plastics. Bioplastic was successfully synthesized using easily available chemicals, making the process accessible and cost-effective. Comprehensive characterization techniques optical microscopy, FTIR spectroscopy, water absorption, solubility, and biodegradability tests, establish the environmental benefits of the starch-based bioplastics. The research showed that commercial polyethylene remained unaffected by all treatment components, confirming its resistance to natural degradation processes. Overall, the results confirm that starch-based bioplastics, particularly those derived from potato starch, exhibit significant environmental compatibility and are well-suited for integration into sustainable manufacturing systems.

Acknowledgments

We thank Dr. Navin Kumar Sharma, Director, and Mr. Ram Tiwari, Principal, Urbana School of Science, Putalisadak, Kathmandu, for providing funding for this research work. We further thank Prof. Dr. Rameshwar Adhikari, Mr. Ramesh Puri, and Ms. Prashamsa Panta for supporting in FTIR and OM experiments on the samples and for fruitful discussions.

Availability of data and materials

The data will be made available at any time when requested.

Funding

The present work was fully supported by the Urbana School of Science, Putalisadak, Kathmandu, Nepal.

Author Contributions

AT and SD: collecting samples and conducting experiments; NR: analyzing FTIR data and contributing in manuscript writing; SB: analyzing biodegradability data, writing and editing; BBM: analyzing solubility data, contributing in manuscript drafting; OPB: graphics design, analysis of water absorption data, manuscript drafting; MMS: supervision, designing experiments, analysis of data, and writing, reviewing, and editing of the manuscript.

Safety and Ethical Declarations

The safety and ethical considerations for the present work were strictly followed under the direct guidance and supervision of the corresponding authors and mentors.

Conflicts of Interest

The authors declare that they have no conflict of interest.

REFERENCES

1. Shafqat A, Tahir A, Mahmood A, Tabinda AB, Yasar A, Pugazhendhi A. A Review on Environmental Significance Carbon Foot Prints of Starch Based Bio-plastic: A Substitute of Conventional Plastics. Biocatal Agric Biotechnol. 2020 Aug;27:101540.
2. Atiwesh G, Mikhael A, Parrish CC, Banoub J, Le TAT. Environmental Impact of Bioplastic Use: A Review. Heliyon [Internet]. 2021 Sep 1 [cited 2025 May 6];7(9). Available from: https://www.cell.com/heliyon/abstract/S2405-8440(21)02021-1
3. Gonçalves EM, Silva M, Andrade L, Pinheiro J. From Fields to Films: Exploring Starch from Agriculture Raw Materials for Biopolymers in Sustainable Food Packaging. Agriculture. 2024 Mar 11;14(3):453.
4. Chapain K, Shah S, Shrestha B, Joshi R, Raut N, Pandit R. Effect of Plasticizers on the Physicochemical Properties of Bioplastic Extracted from Banana Peels. J Inst Sci Technol. 2021 Dec 29;26(2):61–6.

5. Pilla S. Handbook of Bioplastics and Biocomposites Engineering Applications. John Wiley & Sons; 2011. 622 p.
6. Pilla S, editor. Handbook of Bioplastics and Biocomposites Engineering Applications [Internet]. 1st ed. Wiley; 2011 [cited 2025 May 6]. Available from: https://onlinelibrary.wiley.com/doi/book/10.1002/9781118203699
7. Geyer R, Jambeck JR, Law KL. Production, Use, and Fate of All Plastics Ever Made. Sci Adv. 2017 Jul 7;3(7):e1700782.
8. Ezeoha SL. Production of Biodegradable Plastic Packaging Film from Cassava Starch. IOSR J Eng. 2013 Oct;3(10):14–20.
9. Pangestu AR, Shara RT, Mufrodi Z. Biodegradable Plastic from Cassava and Organic Acid as a Synthetic Plastic Replacement. Chem J Tek Kim. 2019 Oct 2;6(1):15–21.
10. Chauhan K, Kaur, Rishpreet, and Chauhan I. Sustainable Bioplastic: A Comprehensive Review on Sources, Methods, Advantages, and Applications of Bioplastics. Polym-Plast Technol Mater. 2024 May 23;63(8):913–38.
11. Bhattarai S, Khanal K, Karki N, Shahi DK, Gc B, Bhatt LR, et al. Synthesis and Characterization of Janus Fenugreek Seed Gum-Based Film for Food Packaging and Wound Dressing Applications. J Nepal Chem Soc. 2024;44.
12. Jabeen N, Majid ,Ishrat, and Nayik GA. Bioplastics and Food Packaging: A Review. Yildiz F, editor. Cogent Food Agric. 2015 Dec 31;1(1):1117749.
13. Mostafa NA, Farag AA, Abo-dief HM, Tayeb AM. Production of Biodegradable Plastic from Agricultural Wastes. Arab J Chem. 2018 May 1;11(4):546–53.
14. Rajgadia N, Debnath M. Biodegradable Mulch Utilizing Bioplastic Biopolymer Polyhydroxyalkanoates. Mater Today Proc. 2023 Jan 1;79:411–9.
15. Adnan NA, Suhaimy SHM, Pauzan MAB, Fauzi B. Effect of Polyvinyl Alcohol on Cassava and Potato Starch Plastic Film: Mechanical, Thermal and Swelling Properties. 2023;3(2).
16. Usman N, Hassan LG, Almustapha MN, Achor M, Agwamba EC. Preparation and Characterization of Thermoplastic Cassava and Sweet Potato Starches. Niger J Basic Appl Sci. 2023 Oct 18;30(2):118–25.
17. Chapain K, Shah S, Shrestha B, Joshi R, Raut N, Pandit R. Effect of Plasticizers on the Physicochemical Properties of Bioplastic Extracted from Banana Peels. J Inst Sci Technol. 2021 Dec 29;26(2):61–6.
18. Marichelvam MK, Manimaran P, Sanjay MR, Siengchin S, Geetha M, Kandakodeeswaran K, et al. Extraction and Development of Starch-Based Bioplastics from *Prosopis Juliflora Plant:* Eco-friendly and Sustainability Aspects. Curr Res Green Sustain Chem. 2022 Jan 1;5:100296.
19. Silveira YDO, Franca AS, Oliveira LS. Cassava Waste Starch as a Source of Bioplastics: Development of a Polymeric Film with Antimicrobial Properties. Foods. 2025 Jan 3;14(1):113.
20. Ben ZY, Samsudin H, Yhaya MF. Glycerol: Its Properties, Polymer Synthesis, and Applications in starch based films. Eur Polym J. 2022 Jul 15;175:111377.
21. Kasirajan S, Ngouajio M. Polyethylene and Biodegradable Mulches for Agricultural Applications: A Review. Agron Sustain Dev. 2012 Apr 1;32(2):501–29.
22. Choubey V, Fatma E, Smriti A, Suman R, Rajak SK. Testing and evaluation of Potato Starch-based Bioplastic. Pharma Innov. 2023 Nov 1;12(11):05–11.
23. Nissa RC, Fikriyyah AK, Abdullah AHD, Pudjiraharti S. Preliminary Study of Biodegradability of Starch-based Bioplastics using ASTM G21-70, Dip-hanging, and Soil Burial Test methods. IOP Conf Ser Earth Environ Sci. 2019 May 1;277(1):012007.
24. Jayarathna S, Andersson M, Andersson R. Recent Advances in Starch-Based Blends and Composites for Bioplastics Applications. Polymers. 2022 Jan;14(21):4557.
25. Rashwan AK, Younis HA, Abdelshafy AM, Osman AI, Eletmany MR, Hafouda MA, et al. Plant Starch Extraction, Modification, and Green Applications: A Review. Environ Chem Lett. 2024 Oct 1;22(5):2483–530.
26. Wu Z, Qiao D, Zhao S, Lin Q, Zhang B, Xie F. Nonthermal Physical Modification of Starch: An Overview of Recent Research into Structure and Property Alterations. Int J Biol Macromol. 2022 Apr 1;203:153–75.
27. Lee S, Kang S, Kwon C, Jung S. Zooglan, An Extracellular Acidic Polysaccharide Isolated from *Zoogloea ramigera* 115 as a novel catalytic

carbohydrate for methanolysis. Carbohydr Polym. 2006 May;64(2):350–4.
28. Shi R, Zhang Z, Liu Q, Han Y, Zhang L, Chen D, et al. Characterization of Citric acid/glycerol Co-plasticized Thermoplastic Starch Prepared by Melt Blending. Carbohydr Polym. 2007 Jul;69(4):748–55.
29. Tang X, Alavi S. Recent Advances in Starch, Polyvinyl Alcohol Based Polymer Blends, Nanocomposites and their Biodegradability. Carbohydr Polym. 2011 Apr;85(1):7–16.
30. Sánchez-González L, Vargas M, González-Martínez C, Chiralt A, Cháfer M. Use of Essential Oils in Bioactive Edible Coatings: A Review. Food Eng Rev. 2011 Mar;3(1):1–16.
31. Zhang WP, Lu YH, Khanal S, Xu SA. Effects of Compatibilizers on Selected Properties of HDPE Composites Highly Filled with Bamboo Flour. Wood Fiber Sci. 2018 Jul 31;50(3):254–64.
32. Folino A, Pangallo D, Calabrò PS. Assessing Bioplastics Biodegradability by Standard and Research Methods: Current trends and Open Issues. J Environ Chem Eng. 2023 Apr 1;11(2):109424.
33. Santana RF, Bonomo RCF, Gandolfi ORR, Rodrigues LB, Santos LS, dos Santos Pires AC, et al. Characterization of Starch-based Bioplastics from Jackfruit Seed Plasticized with Glycerol. J Food Sci Technol. 2018 Jan;55(1):278–86.
34. Pooja N, Banik S, Chakraborty I, Sudeeksha HC, Mal SS, Srisungsitthisunti P, et al. Comparative Analysis of Biopolymer Films derived from Corn and Potato Starch with Insights into Morphological, Structural, and Thermal Properties. Discov Sustain. 2024 Dec 5;5(1):467.
35. Yadav RK, Sahoo S, Yadav AK, Patil SA. *Epipremnum aureum* is a Promising Plant Candidate for Developing Nature-based Technologies for Nutrients Removal from Wastewaters. J Environ Chem Eng. 2021 Oct;9(5):106134.
36. Colclough A, Corander J, Sheppard SK, Bayliss SC, Vos M. Patterns of Cross-resistance and Collateral Sensitivity between Clinical Antibiotics and Natural Antimicrobials. Evol Appl. 2019;12(5):878–87.
37. Krevelen DW van, Nijenhuis K te. Properties of Polymers: Their Correlation with Chemical Structure; Their Numerical Estimation and Prediction from Additive Group Contributions. Elsevier; 2009. 1031 p.
38. Ramírez-Martínez M, Aristizábal SL, Szekely G, Nunes SP. Bio-based Solvents for Polyolefin Dissolution and Membrane Fabrication: From Plastic Waste to Value-added Materials. 2022;
39. Hermansyah H, Carissa R, Faiz MB, Deni P. Food Grade Bioplastic Based on Corn Starch with Banana Pseudostem Fibre/Bacterial Cellulose Hybrid Filler. Adv Mater Res. 2014 Aug 11;997:158–68.
40. Udensi O, Ikpeme EV, Uyoh EA, Brisibe EA. Evaluation of Starch Biodegradable Plastics Derived from Cassava and Their Rates of Degradation in Soil. Niger J Biotechnol. 2009;20(1):28–33.
41. Wahyuningtyas N, Suryanto H. Analysis of Biodegradation of Bioplastics Made of Cassava Starch. J Mech Eng Sci Technol. 2017 Mar 20;1(1):24–31.
42. Klaai L, Imzi S, Hammiche D, Boukerrou A. Preparation and Characterization of Starch Based Bioplastic Film from Potatoes. 2022;1.

Nanomaterials and Polymers Innovations Vol. 1, No. 1 (2025); 58-60
ISSN: 3102-0798 (Online). Available online at www.nepalpolymer.org
DOI:https://doi.org/….xyz… xyz (to be updated)

Brief note

Traditional Nanotechnology of Nepal

Rameshwar Adhikari[1,2*]
[1] *Research Centre for Applied Science and Technology (RECAST) and Central Department of Chemistry, Tribhuvan University, Kirtipur 44618, Kathmandu, Nepal*
[2] *Nepal Polymer Institute (NPI), P. O. Box 24411, Kathmandu, Nepal*
https://orcid.org/0000-0002-7350-0204

Abstract: Some of the local traditional technologies of Nepal, despite lacking modern scientific terminologies in their common uses, have been found to possess inherent nanoscopic structural features. This article attempts to present some typical examples from Nepalese traditional practices, including Ayurvedic *Bhasma*, handmade paper, metallic and mineral particles-containing dyes and artifacts, and traditional cosmetics such as *Gajal*. Further, the historic expansion of the *Paubha* way of painting into Tibet, possibly through Princess *Bhrikuti,* underscores the cultural transmission of such nano-enabled art. These indigenous technologies demonstrate eco-friendly, sustainable, and culturally integrated approaches to materials science. The article emphasizes the value of exploring such practices to inspire contemporary emerging green nanotechnological innovations.

Keywords: Traditional technology; Ayurvedic Bhasma; Nepali paper; *Paubha* art, Metal plating; Gajal

शोधसार: आधुनिक वैज्ञानिक पदावलीहरुको प्रयोग नभएतापनि नेपालका कैयौं परम्परागत प्रविधिहरू आफैंमा नानोविज्ञानका विशेषताहरूले सुशोभित रहेका छन्। प्रस्तुत छोटो आलेखमा नानोविज्ञानसंग संबन्धित गुणहरु ग्रहण गरेका आयुर्वेदिय भस्म, हस्तनिर्मित कागज, धातु एवं खनिज-जन्य कणिकाहरु समेतबाट संश्लेषित प्राकृतिक रङहरू, धातुलेपन संबन्धित कलाकृतिहरू, गाजलजस्ता परम्परागत सौन्दर्य प्रसाधनका बस्तु तथा पौभाः चित्रकला लगायतका परम्परागत अभ्यासहरूलाई प्रस्तुत गरिएको छ। सातौँ शताब्दीमा राजकुमारी भृकुटी मार्फत तिब्बतमा पौभाः र थाङ्का कलाको प्रसारले समेत हाम्रो नानोविज्ञान-सम्बद्ध कलाको सांस्कृतिक पक्षलाई दर्शाउँछ । यस्ता रैथाने प्रविधिहरूले वातावरणमैत्री, दिगो र सांस्कृतिक रूपमा जोडिएको पदार्थ विज्ञानको दृष्टिकोण प्रस्तुत गर्दछन्। यो लेखमा यस्ता परम्परागत अभ्यासहरूको गहन अध्ययन-अनुसन्धान गरेर हरित नानोप्रविधिमा समेत नवीन प्रेरणा लिन सकिने विषयमा जोड दिने प्रयाश गरिएको छ।

Nanotechnology, the manipulation of matter at dimensions below 100 nm, has revolutionized materials science (Bhushan, 2017; Cademartiri and Ozin, 2009). However, many traditional technologies have unknowingly harnessed nanoscale phenomena long before the term "nanotechnology" was coined. Nepal, with its long-standing traditions in Ayurveda, Sowa-Rigpa medicine, metalwork, dyeing, and papermaking, provides fertile ground for investigating such practices. These indigenous methods, shaped by cultural, ecological, and philosophical principles, offer insight into sustainable, low-energy, and eco-friendly approaches to manipulating materials at or near the nanoscale.

Ayurvedic Bhasmas: One prominent example of traditional nano-formulation is the preparation of *Ayurvedic Bhasmas* and *Sowa-Rigpa Rasayanas*. Such traditional medicines, produced through repeated cycles of calcination and purification, are known to contain metal and mineral nanoparticles (Adhikari, 2014). Recent scientific investigations using electron microscopy have revealed that the *Bhasmas* often consist of particles in the nanometer range (Adhikari, 2014; Paudel et al., 2022). Gold-based *Swarna Bhasma* has been reported to have particles ranging between 20 and 60 nanometers, while copper Bhasma contains nanoparticles in the 50 to 100 nm range, potentially contributing to their

Corresponding author, E-mail: nepalpolymer@yahoo.com
© Nepal Polymer Institute, Kathmandu, Nepal
Received: April 23, 2025; Revised: May 11, 2025, Accepted: May 11 2025; Published: May 19, 2025

high surface reactivity and therapeutic bioavailability (Adhikari, 2014; Chaudhary, 2011).

Handmade Paper: In the field of traditional materials, handmade *Lokta* paper represents another compelling example. Made from the inner bark of *Daphne bholua* and *Daphne papyracea*, the paper exhibits a fibrillar and layered network structure when viewed under a field emission scanning electron microscope (FESEM) (see Fig. 1). The micro- and nano-structured cellulose matrix (Aryal et al., 2022; Thapa et al., 2025), combined with residual plant-based compounds, contributes to its antimicrobial and insect-resistant properties. Such features are analogous to those found in modern nanostructured antimicrobial packaging materials.

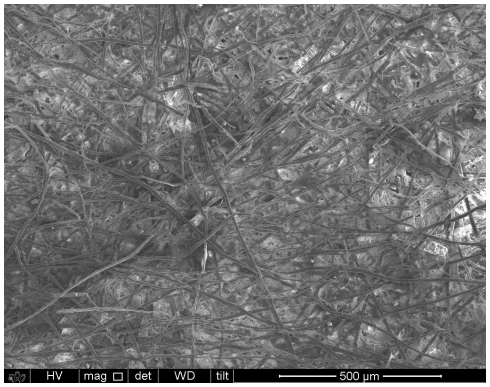

Figure 1: FESEM image of handmade traditional Nepali paper (Adhikari, R. et al, unpublished result)

Natural Dyes: Natural dyes, extensively used in Nepali textiles, also show evidence of nanoscale behavior. Extracts from plants like turmeric, indigo, walnut, and madder, when used with mordants such as alum or iron salts, form stable pigment nanoparticles in aqueous suspensions. These nano-pigments demonstrate enhanced binding properties and improved resistance to photodegradation, contributing to the longevity and vibrancy of traditional textiles (Bhandari et al., 2021). The controlled aggregation of pigment molecules and their interaction with fabrics highlight parallels with colloidal and supramolecular chemistry in modern dye technologies.

Metal Plating: Equally significant is the traditional metal craftsmanship, particularly among Newa artisans of the Kathmandu valley (Joshi et al, 2022; Furger, 2017). Their use of natural abrasives and polishing techniques produces oxide layers and surface finishes at nanometer-scale thickness. Ancient statues and ritual objects made from gilded copper alloys have been shown to possess nanoscale corrosion-resistant coatings, an unintended yet effective surface engineering strategy. Surface analysis studies confirm that these nano-layers contribute to the longevity and aesthetic appeal of these historical artifacts (Furger, 2017).

Gajal: Another notable example of traditional nanotechnology deeply rooted in Nepal is the preparation and use of *Gajal*, a black eye cosmetic widely used for both aesthetic and medicinal purposes. Traditionally, *Gajal* is made by collecting fine soot particles produced from the incomplete combustion of natural oils (such as castor oil or ghee), which are then mixed with herbal oils or ghee to form a smooth paste. Scientific studies suggest that these soot particles are often in the nanometer size range, imparting unique surface properties such as enhanced adhesion, antimicrobial activity, and stability (Sohail et al., 2018; Randhive et al., 2020). The nanoscale structure contributes not only to the cosmetic appeal of *Gajal* but also to its therapeutic effects, protecting and lubricating the eyes, illustrating the intersection of indigenous knowledge with nanoscience principles.

***Paubha* Painting**: A particularly rich and symbolic example of traditional nano-enabled art is the *Paubha* painting tradition, exemplified by the *Prajnaparamita Paubha* preserved at *Hiranyavarna Mahavihara* in Patan (See Fig. 2). Such intricate artworks are painted using finely ground mineral or metals (such as gold and silver) and plant pigments, many of which display the particle diameter well below the micron scale.

Figure 2: Photograph showing the repair of the *Prajnaparamita Paubha* at Hiranyavarna Mahavihara, Patan *(https://risingnepaldaily.com/news/30187)*

Artists traditionally mix the pigments with natural binders, often in oil or water-based vehicles,

allowing for uniform dispersion and fine detailing at an extremely small scale (Gurung, 2025). The nanoparticle, which might form, hence contributes to both aesthetic beauty and long-term preservation. These paintings also exhibit excellent adhesion and resistance to fading, likely due to the stabilization of nano-pigments within natural organic matrices.

There is evidence of the expansion of *Paubha* and *Thanka* art in Tibet, linked historically to Princess Bhrikuti of Nepal, who, according to traditional accounts, married the Tibetan King Songtsen Gampo in the 7th century (Shakya, 2013). As a devout Buddhist and patron of the arts, Bhrikuti is believed to have introduced Nepali artisans and religious iconography to Tibet, thus fostering the development of Thangka painting, a close derivative of *Paubha* art.

Conclusion: Some notable traditional technologies of Nepal illustrate how indigenous knowledge systems can be linked in inspiring ways with the essence of modern nanoscience. By examining these practices through a scientific lens, we uncover nanoscale principles rooted in centuries-old wisdom. These insights not only enhance our understanding of historical technologies but also pave the way for developing sustainable nanomaterials and processes.

Future interdisciplinary research endeavors bridging traditional knowledge and cutting-edge science could yield transformative benefits in environmental remediation and sustainable materials development.

Acknowledgment: The author sincerely dedicates this work, with heartfelt gratitude, to the late Professor Chhabi Lal Gajurel, in honor of his unparalleled and ever-inspiring contributions to the traditional technologies, arts, and crafts of Nepal.

REFERENCES

Bhandari, N. L., Shrestha, S., Bhandari, G., Parajuli, N., Silwal, S. B., & Adhikari, R. (2021). Extraction of dye from *Castanopsis indica* for its use in textile dyeing and medicinal purpose with natural mordant. *Egyptian Journal of Chemistry, 64*(11), 6681–6690. https://doi.org/10.21608/EJCHEM.2021.48519.2991

Bhushan, B. (Ed.). (2017). *Springer Handbook of Nanotechnology* (4th ed.). Springer Publications. https://doi.org/10.1007/978-3-540-29857-1

Cademartiri, L., & Ozin, G. A. (2009). *Concepts of Nanochemistry*. Wiley. ISBN 978-3-527-32597-9

Chaudhary, A. (2011). Ayurvedic Bhasma: Nanomedicine of ancient India—Its global contemporary perspective. *Journal of Biomedical Nanotechnology, 7*(1), 68–69. https://doi.org/10.1166/jbn.2011.1205

Furger, A. R. (2017). *The gilded Buddha: The traditional art of the Newar metal casters in Nepal* (with a contribution by R. J. Shakya). Librum Publishers & Editors. ISBN 978-3-906897-05-9

Gurung, R. (2025). *Paubha painting: The traditional art of Nepal*. https://www.academia.edu/23860855/Paubha_Painting_The_Traditional_Art_Of_Nepal (Retrieved April 5, 2025)

Joshi, P., Maharjan, N., & Nakarmi, M. L. (2022). Comparative study of fire-gilded and electroplated gold films on copper substrates. *Journal of Nepal Physical Society, 8*(3), 13–19. https://doi.org/10.3126/jnphyssoc.v8i3.50717

Mandal, S. M., Saha, S., Sengupta, J., Pratihar, S., & Kaajal. (2013). Fights against eye pathogens and is safe for eye make-up: A reinvestigation of an ancient practice. *The Analyst, 138*(18). https://doi.org/10.1039/c3an01085f

Paudel, R., Karn, G., Aryal, G., Giri, J., Adhikari, R., & Sharma, M. L. (2022). Synthesis, characterization, biological study of synthesized Lauha bhasma. *Journal of Nepal Chemical Society, 43*(1), 4–15. https://doi.org/10.3126/jncs.v43i1.47031

Randive, D. S., Bhinge, S. D., Jadhav, N. R., Bhutkar, M. A., & Shirsat, M. K. (2020). Carbon based kajal formulations: Antimicrobial activity and feasibility as a semisolid base for ophthalmics. *Journal of Pharmaceutical Research International, 32*(13), 62–74. ⟨hal-05330807⟩

Shakya, M. B. (2013). *Sacred art of Nepal*. Federation of Handicraft Associations of Nepal. ISBN 9789993337317

Sohail, T., Rahman, A. U., Imran, H., Yaqeen, Z., Fatima, N., Rehman, Z. U., & Shireen, K. (2018). Toxicological studies of popular eye cosmetic used world wide. *Bangladesh Journal of Medical Science, 18*(1), 118–123. https://doi.org/10.3329/bjms.v18i1.39561

Thapa, Y. N., Dhungana, P., Rajchal, B., Karki, D., Khanal, B., Nepal, A., Henning, S., Joshi, S., Avasthi, D. K., & Adhikari, R. (2025). Antimicrobial evaluation of polyaniline-coated Argeli paper for sustainable packaging. *Nepal Journal of Environmental Science*. (Under review)

AUTHORS GUIDELINES

Title	Nanomaterials and Polymers Innovations (NαPI)
Publication fields	All areas of nanoscience, nanotechnology, and polymers
Publication mode	Online (Prints only on demand, as required)
Papers format	Original research papers, review articles, opinion articles, case reports, and short communications, letter to the editor
Publisher	Nepal Polymer Institute (NPI), Kathmandu, Nepal
Frequency	One volume comprising 2 issues each year; special issues may be published
Language	English; the abstract in both English and Nepali; no translation service available

Text Preparation and Formatting: The manuscript must be typed in English in MS Word using the font 'Times New Roman' in double-spaced 12-point letters without using any predefined formatting. The Nepali version of the abstract should be typed in Unicode format.

The paper should report original research work that has neither been published nor considered for publication anywhere, and if accepted, will not be published elsewhere in the same form in any language. All the manuscripts will be peer-reviewed. If revision of the original manuscript is required, authors should revise and resubmit the paper within the specified time, addressing all the comments.

The content of the manuscripts should follow the order: title, author(s)/affiliation(s), postal address(es), E-mail ID and Telephone number of the corresponding author, abstract, 4-5 keywords, body text (Introduction, Materials and Methods, Results and Discussion, Conclusion), acknowledgments, funding information (if any); references, with figures and tables having their respective captions (e.g., Figure 1a, 1b, 2, 3…., Table 1a, 2, 3….). Abstracts of a single paragraph and up to 200 words are required for all manuscripts. The *Original Research Article* can contain 4 tables and 4 figures or artwork, whereas *Short Communication* should be within 2,500 words in length and can contain a total of 4 pages, including figures and tables. If necessary for review purposes, supplementary information can be supplied. The initial submission should be accompanied by a PDF file of the same. *Original Research, Short Communication*, and *Opinion Articles* comprise the body parts as given above; however, Reviews can be written differently (Please ask the Editor-in-Chief before submitting a Review Article). Review papers can be submitted by invitation only. However, authors may send a proposal to the editorial office if they intend to submit a review or mini-review to the journal.

Reference Citation*:* Any standard format is acceptable; the APA format is preferred.

Tables and Figures: Tables and Figures should be submitted separately from the text, and each table should have an explanatory caption. The figure must be supplied in the JPEG or TIFF format with at least a resolution of 300 DPI. Colour figures should be in RGB format; colour figures will only be printed in grayscale images. All text and symbols on a table and figure should be large enough to read easily, considering they are to be reduced in size to fit in a single-column width (7.5 cm) or two-column width (16 cm).

Publication Charge: There are no submission or processing fees for authors, as we strongly believe in the value of charitable and voluntary contributions to science. *Nanomaterials and Polymers Innovations* is a diamond open-access, community-driven journal, founded on the belief that volunteer-led, community-governed scientific publishing is essential for a sustainable future and that publishing science is a shared moral responsibility in the stewardship of knowledge.

Copyright Forms: The authors must sign and forward the copyright transfer agreement before the publication of the article. The author(s) are responsible for collecting permission from authors and publishers if the published materials have to be reproduced.

Special Issue Editors (Vol. 1, Issue 1)

Dr. Rameshwar Adhikari, Dr. Sven Henning, and Dr. Ralf Lach